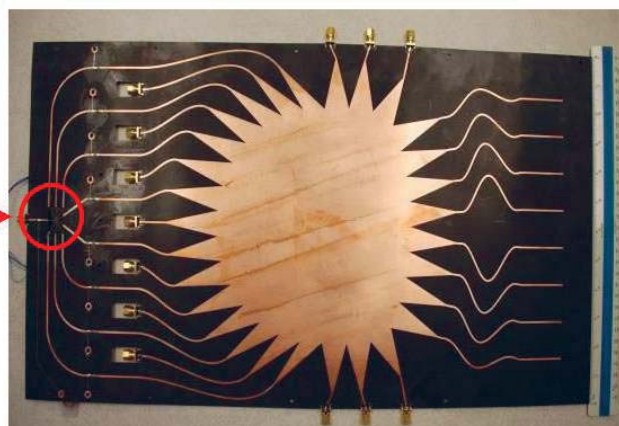
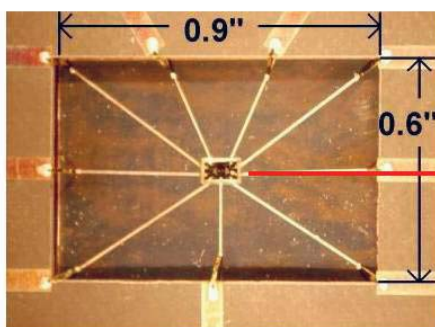
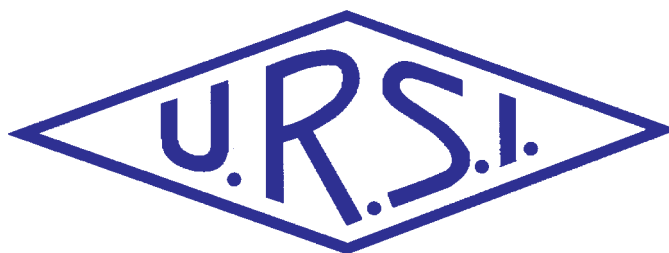


Radio Science Bulletin

ISSN 1024-4530

INTERNATIONAL
UNION OF
RADIO SCIENCE

UNION
RADIO-SCIENTIFIQUE
INTERNATIONALE



No 333
June 2010

URSI, c/o Ghent University (INTEC)
St.-Pietersnieuwstraat 41, B-9000 Gent (Belgium)

Contents

Editorial	3
Rotman Lens Applications for the US Army: A Review of History, Present, and Future.....	10
Four Decades of Space-Borne Radio Sounding.....	24
Picosecond-Level Error Detection Using PCA in the Hardware Timing Systems for the EISCAT_3D LAAR.....	45
Radio-Frequency Radiation Safety and Health	51
Conferences.....	53
News from the URSI Community.....	56
Information for authors	61

Front cover: A C-band integrated Rotman lens and patch antenna array, with integrated switch (shown enlarged on the left) for electronic scanning. See the paper by Ozlem Kilic and Steven J. Weiss on pp. 10-23.

EDITOR-IN-CHIEF
URSI Secretary General
Paul Lagasse
Dept. of Information Technology
Ghent University
St. Pietersnieuwstraat 41
B-9000 Gent
Belgium
Tel.: (32) 9-264 33 20
Fax : (32) 9-264 42 88
E-mail: ursi@intec.ugent.be

EDITORIAL ADVISORY BOARD
François Lefeuvre
(URSI President)
W. Ross Stone

PRODUCTION EDITORS
Inge Heleu
Inge Lievens

SENIOR ASSOCIATE EDITOR
J. Volakis
P. Wilkinson (RRS)

ASSOCIATE EDITOR FOR ABSTRACTS
P. Watson

ASSOCIATE EDITOR FOR BOOK REVIEWS
K. Schlegel

EDITOR

W. Ross Stone
840 Armada Terrace
San Diego, CA92106
USA
Tel: +1 (619) 222-1915
Fax: +1 (619) 222-1606
E-mail: r.stone@ieee.org

ASSOCIATE EDITORS

W.A. Davis (Com. A)	R. Lang (Com. F)
G. Manara (Com. B)	J.D. Mathews (Com. G)
M. Luise (Com. C)	O. Santolik (Com. H)
P-N Favennec (Com. D)	R. Strom (Com. J)
A. van Deursen (Com. E)	J. Wiart (Com. K)

For information, please contact :

The URSI Secretariat
c/o Ghent University (INTEC)
Sint-Pietersnieuwstraat 41, B-9000 Gent, Belgium
Tel.: (32) 9-264 33 20, Fax: (32) 9-264 42 88
E-mail: info@ursi.org

The International Union of Radio Science (URSI) is a foundation Union (1919) of the International Council of Scientific Unions as direct and immediate successor of the Commission Internationale de Télégraphie Sans Fil which dates from 1913.

Unless marked otherwise, all material in this issue is under copyright © 2010 by Radio Science Press, Belgium, acting as agent and trustee for the International Union of Radio Science (URSI). All rights reserved. Radio science researchers and instructors are permitted to copy, for non-commercial use without fee and with credit to the source, material covered by such (URSI) copyright. Permission to use author-copyrighted material must be obtained from the authors concerned.

The articles published in the Radio Science Bulletin reflect the authors' opinions and are published as presented. Their inclusion in this publication does not necessarily constitute endorsement by the publisher.

Neither URSI, nor Radio Science Press, nor its contributors accept liability for errors or consequential damages.

The second part of the Special Section on High-Altitude Platforms (HAPs) has been delayed until the September issue (the first part was in the March issue). We also have some other exciting special sections planned for near-term future issues. These include a Special Section on Computational Electromagnetics, and a special section with the papers of the finalists of the Student Paper Competition for AP-RASC'10, the URSI Asia-Pacific Radio Science Conference.



science associated with these payloads. He begins with a comprehensive summary of the experiments and their objectives. He then explains that the original primary purpose of space-based radio sounding was to determine the vertical profile of the electron density of the ionosphere, N_e , above the peak in density (from the "topside"), on a routine basis over large areas. The challenges associated with doing this are explained, along with the differences between topside and bottom-side radio sounding. The methods of relating what can be measured by

Our Papers

The ability to *simultaneously* scan multiple beams of an antenna array is critical to many applications, including many military applications. It can be costly to this with mechanical scanning, or with electronic scanning using phase shifters. Electronic phase shifters can also be lossy. A Rotman lens uses time-delay paths to create the required phase shifts across the array. In an invited *Review of Radio Science* from Commission A, Ozlem Kilic and Steven Weiss describe the history, current status, and future plans regarding the use of Rotman lenses by the US Army. They begin with an overview of the need for simultaneously scanning multiple beams, and approaches for doing this. This leads to an explanation of the advantages of the Rotman-lens approach. They briefly trace the history of the Rotman lens, and describe how it can be considered to be a multiple-input multiple-output (MIMO) beamformer. The design of a Rotman lens, and practical considerations associated with such designs, are explained. The authors then present a brief history of the use of Rotman lenses in Army applications. This is followed by an in-depth look at current state-of-the-art implementations of the Rotman lens. This includes cavity lenses, and novel microstrip and printed lens designs. The latter includes the use of a metallic-plated plastic lens and antenna array, and an integrated switching system, to achieve a compact, lightweight, and inexpensive system. An additional advantage is that the system is mechanically flexible. The paper concludes with a look at future directions for this technology.

The efforts of Bill Davis, Associate Editor for Commission A, and Phil Wilkinson in bringing us this *Review* are greatly appreciated.

There have been 38 rocket, satellite, and planetary payloads dedicated to radio sounding of the ionosphere and magnetosphere (both of the Earth and other planets) since 1961. In his invited *Review of Radio Science* from Commission H, Robert Benson describes the history and

sounders to the desired physical quantities are described. Information about the various errors and limitations of the different types of sounding is given. This is followed by an examination of the scientific discoveries that have resulted from the use of topside sounders. These include information about a variety of plasma properties, as well as knowledge of gradients in electron density and in the planetary magnetic field. Innovations in instrumentation for topside sounding are described and discussed. The paper explains how it was discovered that the act of radio sounding could excite resonances in the plasma. This underscored the importance of the orientation of the sounder's antenna(s), and also provided a new tool for exploring the topside region. The exploration of a variety of special plasma conditions using sounder-excited resonances is described, along with some of the most important results obtained. The paper concludes with an examination of the observations of nearly lossless propagation in electron-density ducts.

The *Bulletin* thanks Ondrej Santolik, Associate Editor for Commission H, and Phil Wilkinson for bringing us this *Review*.

EISCAT_3D is a design for a new incoherent-scatter radar based on a large-aperture array radar. In this case, "large aperture" means that the incoming radar pulses are shorter than the aperture of the radar. This means that time-delay beamforming has to be used (as opposed to phase-delay beamforming). Timing errors among the elements of the radar array become very important in such a system. The paper by Gustav Johansson, Fredrik Häggglund, Johan Carlson, and Jonny Johansson describes a method based on a statistical analysis of the data received by the array for detecting such timing errors. The method described is not intended to replace the cable-calibration system of the array. However, because the method can be used while the radar is operating without affecting operations, it has certain advantages. The paper begins with a brief explanation of the signals to be received by EISCAT_3D. The error-detection method is based on a statistical-analysis tool called principal-component analysis. Principal-component

analysis characterizes the data in a series of components such that each successive component describes the largest variation in the data not already described by a previous component. A score can be calculated for each principal component that describes how well that component characterizes a portion of the data set. Applying this method to each subarray of the large radar array and comparing the scores obtained allows identification of any subarrays for which the data are different. This, in turn, identifies subarrays with potential timing errors. The paper describes how principal-component analysis is applied to the radar data, and how the scores are used to detect timing errors. A software tool developed for simulating the large-aperture array radar is described. A series of simulation experiments are then described. In these experiments, known, random timing errors were introduced into the array. The principal-component analysis method was applied to the resulting data, and the detection (or failure to detect) the timing errors was analyzed. Two main types of experiments were performed. One tested how small the timing errors could be and still be detected by the method. The other looked at how many subarrays of the radar could be faulty before the method became unreliable. The results showed that as long as the timing errors were larger than the standard deviation of the acceptable timing errors throughout the array, and as long as no more than about 20% of the subarrays were faulty, the detection method would detect all of the faults with a 0% false-alarm rate. This paper is interesting both because of the results obtained for the EISCAT_3D design, as well as because of the explanation it provides for the use of principal-component analysis.

Also in this Issue

Kristian Schlegel has been doing an excellent job of obtaining interesting and insightful reviews of books in the radio-science field, and some of the results of his efforts are included in this issue. One of the books reviewed, Jean Van Bladel's *Electromagnetic Fields, Second Edition*, is a particular favorite of mine. This is one of those books that belongs on every radio scientist's shelf – because it will be constantly used!

Jim Lin provides some interesting commentary on addictive behavior, cell phones, and the state of funding for research on the biological effects of cell phones. As you read this, think about *your* reaction to not having access to mobile-phone service.

The announcement and call for papers for the XXXth URSI General Assembly and Scientific Symposium, to be held August 13-20, 2011, in Istanbul, Turkey, appeared in the March issue, and is also included here. *Be sure to take note of the announcement that is new in this issue, describing the Student Paper Competition.* This is an exciting opportunity for students of radio science around the world. Please also take note of the Young Scientist Program.

I started this column with a note about future special sections in the *Radio Science Bulletin*. If you have an interest in a particular topic, consider organizing a special section in the *Bulletin*. Get in touch with me and if it is appropriate, I'll gladly work with you to make a special section happen.





XXX General Assembly and Scientific Symposium of the International Union of Radio Science

Union Radio Scientifique Internationale

August 13-20, 2011 Lütfi Kırdar Convention and Exhibition Centre, Istanbul,
TURKEY

Call for Papers

The XXX General Assembly and Scientific Symposium of the International Union of Radio Science (Union Radio Scientifique Internationale: URSI) will be held at the Lütfi Kırdar Convention and Exhibition Centre in the beautiful historical center of Istanbul, Turkey, August 13-20, 2011.

The XXX General Assembly and Scientific Symposium will have a scientific program organized around the ten Commissions of URSI and consisting of plenary lectures, public lectures, tutorials, posters, invited and contributed papers. In addition, there will be workshops, short courses, special programs for young scientists, student paper competition, programs for accompanying persons, and industrial exhibits. More than 1,500 scientists from more than fifty countries are expected to participate in the Assembly. The detailed program, the link to an electronic submission site, the registration form, and hotel information will be available on the General Assembly Web site: <http://www.ursigass2011.org>

Information for all authors -Submission information

All contributions (four pages full paper and up to 100 words abstract) should be submitted electronically via the link provided on the General Assembly Web site. Please consult the symposium Web site, <http://www.ursigass2011.org>, for the latest instructions, templates, and sample formats.

Important Deadlines

Paper submission February 11, 2011

Notification of acceptance April 30, 2011

Topics of Interest

Commission A : Electromagnetic Metrology Commission B : Fields and Waves Commission C : Radiocommunication Systems and Signal Processing Commission D : Electronics and Photonics Commission E : Electromagnetic Environments and Interference Commission F : Wave Propagation and Remote Sensing Commission G : Ionospheric Radio and Propagation Commission H : Waves in Plasmas Commission J : Radio Astronomy Commission K : Electromagnetics in Biology and Medicine

Student Paper Competition

A student must be first author of the paper. The student's advisor should attach a statement that his/her contribution is primarily advisory. All other submission requirements and instructions can be found at symposium Web site.

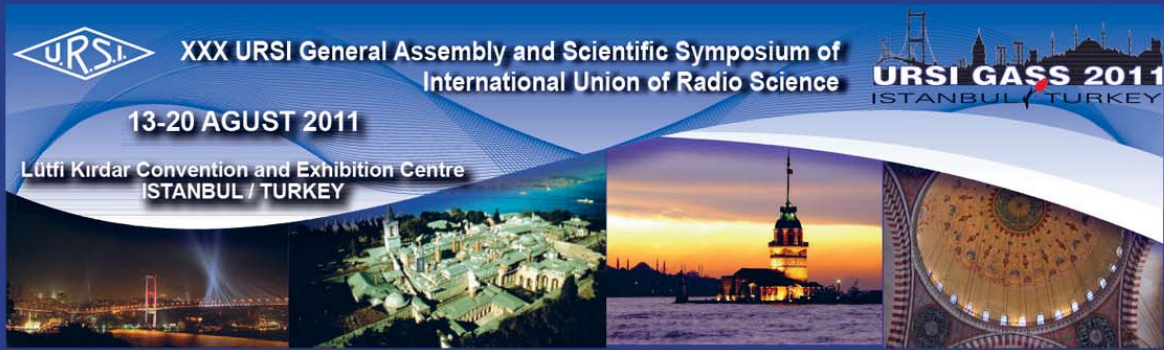
Special Sessions

Individuals interested in organizing special sessions should request permission from the Chair of the appropriate URSI Commission.

Contact

For any questions related to the XXX General Assembly, please contact the Chair of the Conference: Prof. Hamit Serbest Department of Electrical and Electronics Engineering Cukurova University, Adana, Turkey

E-mail: ursigass2011@ursigass2011.org



FIRST ANNOUNCEMENT

The XXX General Assembly and Scientific Symposium of the International Union of Radio Science (Union Radio Scientifique Internationale-URSI) will be held at the Lutfi Kirdar Convention & Exhibition Centre, Istanbul, Turkey on August 13-20, 2011.

The General Assemblies and Scientific Symposia of URSI are held at intervals of plans for future research and special projects in all areas of radio science, especially where international cooperation is desirable. The first Assembly was held in Brussels, Belgium in 1922 and the latest in Chicago, IL, USA in 2008.

The XXX General Assembly and Scientific Symposium will have a scientific program organized around the ten Commissions of URSI and consisting of plenary lectures, public lectures, tutorials, invited and contributed papers. In addition, there will be workshops, short courses, special programs for young scientists, student paper competition, and programs for accompanying persons. More than 1,500 scientists from more than fifty countries are expected to participate in the Assembly and Scientific Symposium.

The Call for Papers will be issued in mid 2010, will be published in the Radio Science Bulletin and in the IEEE Antennas and Propagation Magazine, and will be posted on the URSI website. It is expected that all papers should be received by the beginning of February 2011, that Authors will be notified of the disposition of their submissions by the end of April 2011.

Preliminary information

Detailed information on the scientific program and on abstract submissions will be available toward the end of March 2010. A web site with current information on the XXX General Assembly is available at: www.ursigass2011.org and all abstracts will be received electronically.



Organizing Committee

Chair	A. Hamit Serbest, <i>Cukurova University, Turkey</i> , hamitserbest@gmail.com
Vice Chair	Ayhan Altıntaş, <i>Bilkent University, Turkey</i> , altintas@ee.bilkent.edu.tr
Finance	Sedef Kent, <i>Technical University of Istanbul, Turkey</i> , kents@itu.edu.tr
Publications	Erdem Yazgan, <i>Hacettepe University, Turkey</i> , yazgan@hacettepe.edu.tr
Young Scientists	Özlem Aydın Çivi, <i>Middle East Technical University, Turkey</i> , ozlem@metu.edu.tr
Student Paper Competition	Birsen Saka, <i>Hacettepe University, Turkey</i> , birsen@hacettepe.edu.tr
Workshops/Short Courses	Vakur B. Ertürk, <i>Bilkent University, Turkey</i> , vakur@ee.bilkent.edu.tr
Exhibits	Şimşek Demir, <i>Middle East Technical University, Turkey</i> , simsek@metu.edu.tr
Fundraising	Erdal Panayırıcı, <i>Kadir Has University, Turkey</i> , eeapanay@khas.edu.tr
Registration	Tour Select Ltd, organization@ursigass2011.org
Social activities	Tour Select Ltd, organization@ursigass2011.org
Hotel Reservation	Tour Select Ltd, organization@ursigass2011.org
Contact with URSI	P. Van Daele, peter.vandaele@intec.ugent.be W. Ross Stone, r.stone@ieee.org

Scientific Program Committee

Coordinator	P.L.E. Uslenghi (<i>U.S.A</i>)
Associate Coordinator	A. Hamit Serbest (<i>Turkey</i>)
Commission A	Chair: P. Banerjee (<i>National Physical Laboratory, New Delhi, India</i>) Vice Chair: W. A. Davis (<i>Virginia Tech, Blacksburg, VA, USA</i>)
Commission B	Chair: Karl J. Langenberg (<i>University of Kassel, Germany</i>) Vice-Chair: Giuliano Manara (<i>Università di Pisa, Italy</i>)
Commission C	Chair: Prof. Takashi Ohira (<i>Toyohashi University of Technology, Japan</i>) Vice-Chair: Prof. Marco Luise (<i>University of Pisa-Dip. Ingegneria Informazione, Italy</i>)
Commission D	Chair: Franz Kaertner (<i>USA</i>) Vice Chair: Mr. S. Tedjini (<i>INPG-ESISAR, France</i>)
Commission E	Chair: Professor Christos Christopoulos (<i>University of Nottingham, UK</i>) Vice-Chair: Professor A P J van Deursen (<i>Technische Universiteit Eindhoven, Netherlands</i>)
Commission F	Chair: Madhu Chandra (<i>Germany</i>) Vice Chair: Dr R.H. Lang (<i>George Washington University, USA</i>)
Commission G	Chair: Dr Michael T Rietveld (<i>EISCAT Scientific Association, Norway</i>) Vice Chair: Prof John D Mathews (<i>Pennsylvania State University, USA</i>)
Commission H	Chair: Yoshiharu Omura (<i>Japan</i>) Vice Chair: Dr. O. Santolik (<i>Academy of Sciences of the Czech Republic, Czech Republic</i>)
Commission J	Chair: Subra Anathakrishnan (<i>India</i>) Vice Chair: Dr. D.C. BACKER, (<i>University of California, USA</i>)
Commission K	Chair: Guglielmo D'Inzeo (<i>Italy</i>) Vice Chair: Prof. M. TAKI, (<i>Tokyo Metropolitan University, JAPAN</i>)

www.ursigass2011.org

AWARDS FOR YOUNG SCIENTISTS

CONDITIONS

A limited number of awards are available to assist young scientists from both developed and developing countries to attend the General Assembly and Scientific Symposium of URSI.

To qualify for an award the applicant:

1. must be less than 35 years old on September 1 of the year of the URSI General Assembly and Scientific Symposium;
2. should have a paper, of which he or she is the principal author, submitted and accepted for oral or poster presentation at a regular session of the General Assembly and Scientific Symposium.

Applicants should also be interested in promoting contacts between developed and developing countries. Applicants from all over the world are welcome, also from regions that do not (yet) belong to URSI. All successful applicants are expected to participate fully in the scientific activities of the General Assembly and Scientific Symposium. They will receive free registration, and financial support for board and lodging at the General Assembly and Scientific Symposium. A basic accommodation is provided by the assembly organizers permitting the Young Scientists from around the world to collaborate and interact. Young scientists may arrange alternative accommodation, but such arrangements are entirely at their own expense. Limited funds will also be available as a contribution to the travel costs of young scientists from developing countries.

The application needs to be done electronically by going to the same website used for the submission of abstracts/papers. This website is www.papers-GASS2011.ursi.org. The deadline for paper submission for the URSI GASS2011 in Istanbul is 07 February 2011.

A web-based form will appear when applicants check “Young Scientist paper” at the time they submit their paper. All Young Scientists must submit their paper(s) and this application together with a CV and a list of publications in PDF format to the GA submission Web site.

Applications will be assessed by the URSI Young Scientist Committee taking account of the national ranking of the application and the technical evaluation of the abstract by the relevant URSI Commission. Awards will be announced on the URSI Web site in April 2011.

For more information about URSI, the General Assembly and Scientific Symposium and the activities of URSI Commissions, please look at the URSI Web site at: <http://www.ursi.org> or the GASS 2011 website at <http://www.ursigass2011.org/>

If you need more information concerning the Young Scientist Program, please contact:

The URSI Secretariat
c/o Ghent University / INTEC
Sint-Pietersnieuwstraat 41
B-9000 GENT
BELGIUM
fax: +32 9 264 42 88
E-mail: ingeursi@intec.ugent.be

URSI Student Paper Competition

Chair: Prof. Steven C. Reising
Colorado State University, Fort Collins, CO, USA

Student Paper Prize winners, 1st Place through 5th Place, will be awarded a certificate and check in the amounts of \$1500, \$1250, \$1000, \$750 and \$500, respectively.

Rules and Guidelines

- First author and presenter must be a full-time university student.
- The topic of the paper must be related to the field of one of the ten URSI Commissions.
- A full paper must be submitted by the abstract deadline. The paper must be not longer than 25 pages and in the single-column, double-spaced manuscript format of the journal *Radio Science*.
- A letter from the student's advisor on university letterhead must be appended to the paper. The letter must state that the author is enrolled as a full-time university student in a degree program. If co-authored, the letter must state that all co-authors played only an advisory role. *No other students are permitted as co-authors.*
- Ten finalists will be chosen based upon quality, originality and scientific merit. They will receive free access to the workshop/short course of their choice. They will be required to attend the banquet, where all finalists will be recognized, and the prizes will be presented.
- The URSI Panel of Judges will consist of the ten URSI Commission Chairs or their authorized representatives, in case of absence.
- In addition, the prizes will be awarded based on the clarity of their presentation, accessibility to the broad audience of the ten URSI Commissions and the ability to answer questions on their work.
- All participants will have the option of submitting their full paper manuscripts for review for publication in a special section of the journal *Radio Science* edited by Prof. Piergiorgio L. E. Uslenghi, Univ. of Illinois at Chicago, IL, USA, 2011 URSI GASS Scientific Program Coordinator.

Rotman Lens Applications for the US Army: A Review of History, Present, and Future



Ozlem Kilic
Steven J. Weiss

Abstract

Array antennas that can simultaneously scan multiple beams are often desired for many radar and communications applications. One scanning approach controls the relative phase values at the array elements using microwave lens structures, achieving the desired progressive phase shifts through time delays. The Rotman lens is such a structure. It offers a cost-effective solution to electronic scanning of array antennas by serving as a broadband multiple-input multiple-output beamformer network. Rotman lenses have found many uses in both military and commercial applications. This paper gives an overview of Rotman-lens applications from the military perspective. Ongoing efforts, future plans, and how the Rotman lens is foreseen as a feasible platform are also discussed.

1. Introduction

Many radar and communications systems require wide areas to be scanned, preferably simultaneously, by multiple beams. As a consequence, array antennas with beamformer

networks are needed so that the amplitude and phase can be controlled, creating the desired beams in space. There are numerous possible ways of achieving simultaneous beam scanning with array antennas. Common techniques employ phase shifters for electronically scanning antenna arrays, or array feeds with a switching matrix for reflector systems. Direct-radiating electronic scanning antennas are often preferable over reflector antennas for many applications, because of their more compact size. A phase-shifter approach can be costly and lossy for these antenna arrays, especially when they require a large number of beams to be scanned. This is especially true at higher frequencies, such as Ka band and above, where some future military applications reside. Rotman lenses offer a cost-effective solution to electronic multiple-beam scanning, creating a lens-like medium that utilizes time-delay paths to realize the required progressive phase shift. In essence, a Rotman lens is a multiple-input multiple-output beamformer network, where the excitation of the different input ports results in a phase taper at the output ports. The output ports are often planar, allowing for an ideal transition to an array antenna. In contrast, the input ports lie on a particular circular arc defined by the lens geometry. Possible scenarios for scanning antennas are shown in comparison to the Rotman lens in Figure 1.

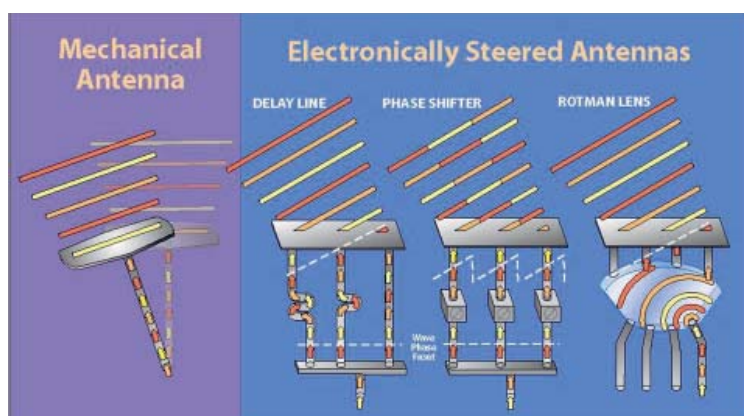


Figure 1. Possible scanning options for antennas.

Ozlem Kilic is with the Catholic University of America, Washington, DC, USA; e-mail: kilic@cua.edu. Steven J. Weiss is with the US Army Research Laboratory, Adelphi, MD, USA; e-mail: steven.weiss@us.Army.mil.

This is an invited *Review of Radio Science* from Commission A

The original Rotman lens was developed in 1963. It achieved two-dimensional scanning using a parallel-plate transmission medium for a true-time-delay lens architecture, and RF coaxial cables that fed a linear aperture array [1]. In his paper, Rotman demonstrated that the lens could achieve broadband performance and scan wide angles in fractional degree steps: outperforming the state-of-the-art at the time. His work improved on the coma aberrations – i.e., the off-axis phase distortions – of the general lens principles that were developed by Gent [2] by using three perfect focal points at the input side.

Since the introduction of Rotman’s design, many researchers have suggested improvements or alternative considerations. Shelton [3] suggested that it is not necessary to have a circular focal arc. Katagi et al. [4] introduced an alternative approach to reduce the phase errors by defining a refocusing equation. Gagnon [5] introduced the term “refracting lens” by suggesting that Snell’s law can be applied to the refocusing of the focal arc. Rotman lenses still draw attention both for commercial use, such as in satellite communications [6, 7], and for military applications [8]. This is due to their potential to electronically scan beams over a wide range of view in small scan steps for a broad bandwidth, while allowing easy integration with the array antenna in a cost-effective manner.

The objective of this paper is to present the developments in Rotman lenses that have been initiated at the US Army Research Laboratory (ARL), both from a historic point of view and the current state of the art. A basic overview of the lens-design considerations, as originally developed by Rotman, is presented in Section 2. The application of the lens from the military perspective – especially, the Army – is discussed in Section 3. Rotman lenses are electrically large structures with fine features

(e.g., the feeds), which can make the modeling a challenge. The Army Research Laboratory has investigated software tools for accurate modeling of these lenses, as discussed in Section 3. Conclusions and a perspective on the future use of Rotman lenses are provided in Section 4.

2. Rotman Lens Design Considerations

A classic Rotman lens consists of a parallel-plate region surrounded by input beam ports, output array ports, and dummy ports that are terminated with a matching impedance to create reflection-less sidewalls for the lens. The input beam ports lie on a circular arc. The output ports reside on a straight line, and are connected to the lens’ output walls via delay lines of particular lengths to allow for the desired scan range of the lens. A typical design begins by specifying the number of radiating elements, i.e., the array ports (N_{out}) and their uniform separation along the array axis, and the number of beam positions at the input (N_{in}), with the desired beam-steering angles. The basic components of the lens are shown in Figure 2.

Three perfect focal points, F_0 , F_1 , and F_2 , reside on the input arc of the lens, where F_1 and F_2 are symmetric with respect to F_0 , as depicted in Figure 3. The on-axis and off-axis focal lengths are denoted by f_0 and f , respectively. The classic development equates ψ and α , as will be used for the initial development. The center of the circular arc at the input wall resides at (x_0, y_0) with respect to the coordinate system of the output wall, S_1 .

The lens equations are derived by generating constant phase fronts at the lens output for the perfect focal points, as follows:

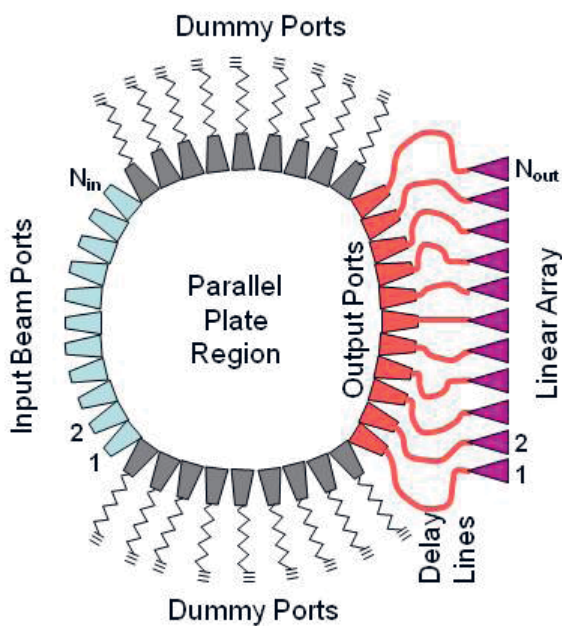


Figure 2. The basic regions of the Rotman lens.

$$\begin{aligned} \overline{F_1 P} + w + y_a \sin \alpha &= f + w_0, \\ \overline{F_2 P} + w - y_a \sin \alpha &= f + w_0, \\ \overline{F_0 P} + w &= f_0 + w_0. \end{aligned} \quad (1)$$

In Equation (1), w_0 is the length of the delay line at the center array element, and $P(x, y)$ denotes a point on the output lens’ wall. The first two equations in Equation (1) enforce a constant phase front for fields traveling from the two symmetric focal ports to any of the array elements on S_2 . The third equation does the same for the center focal point. Since the center focal point has uniform phase across the output ports, it produces a beam along the bore-site direction. The two symmetric focal ports steer the beam by $\pm\alpha$ degrees with respect to the bore site. There are no phase errors at these perfect focal points, as the equations in Equation (1) indicate. The other possible input ports that

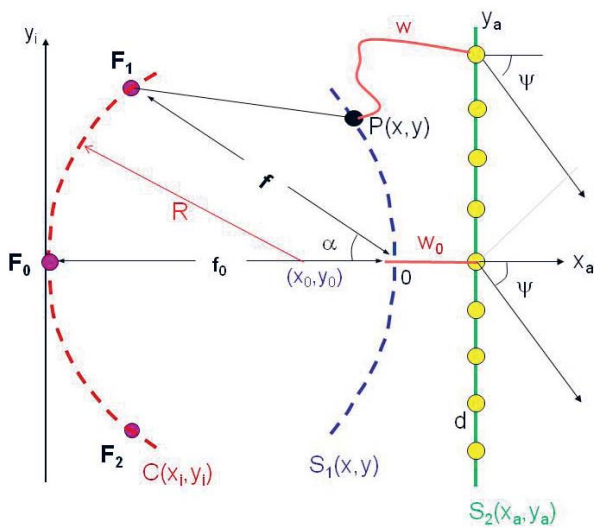


Figure 3. The Rotman lens geometry.

reside between the three perfect ports will have some phase distortion. Rotman investigated the effects of this phase error in his paper, and recommended an optimal focal ratio as a function of scan angle.

The unknowns in the lens design are typically the delay lengths and the curvature of the output lens wall, S_1 . In general, the user specifies the focal length and scan range of the lens. Equations (1) can be rearranged to provide an algebraic equation for the delay lengths (w) between the output walls and the linear array elements. First, the path lengths are expressed in terms of the focal lengths and beam angles such that

$$\begin{aligned} |F_1 P|^2 &= (x + f \cos \alpha)^2 + (y - f \sin \alpha)^2, \\ |F_2 P|^2 &= (x + f \cos \alpha)^2 + (y + f \sin \alpha)^2, \\ |F_0 P|^2 &= (x + f_0)^2 + y^2. \end{aligned} \quad (2)$$

By introducing a normalization with respect to the center focal length such that

$$x = \frac{x}{f_0}, y = \frac{y}{f_0}, y_a = \frac{y_a}{f_0}, \omega = \frac{w - w_0}{f_0},$$

and

$$f = \frac{f}{f_0},$$

and using Equation (2) in Equation (1), one obtains

$$y = y_a \left(1 - \frac{\omega}{f}\right) = y_a \left(1 - \frac{\omega}{f}\right), \quad (3)$$

$$x = -\frac{(1-f)\omega + \frac{1}{2}y_a^2 \sin^2 \alpha}{1-f \cos \alpha}, \quad (4)$$

$$x^2 + y^2 + 2x = \omega^2 - 2\omega. \quad (5)$$

From Equations (4) and (5), the normalized delay lengths, ω , can be expressed in a second-order polynomial as

$$a\omega^2 + b\omega + c = 0, \quad (6)$$

where the coefficients for Equation (6) are given by the lens parameters as follows:

$$\begin{aligned} a &= 1 - \frac{(1-f)^2}{(1-f \cos \alpha)^2} - \frac{y_a^2}{f^2}, \\ b &= -2 + 2\frac{y_a^2}{f} + \frac{2(1-f)}{1-f \cos \alpha} - \frac{y_a^2 \sin^2 \alpha (1-f)}{(1-f \cos \alpha)^2}, \\ c &= -y_a^2 + \frac{y_a^2 \sin^2 \alpha}{1-f \cos \alpha} - \frac{y_a^4 \sin^4 \alpha}{4(1-f \cos \alpha)^2}. \end{aligned} \quad (7)$$

Once the solution to the delay lines is obtained by solving for the roots of Equation (6), the curvature of the lens output surface, S_1 , can be computed from the circle equation of Equation (5) as a function of the delay lengths. Furthermore, the center point of the input arc, (x_0, y_0) , can be computed from the equation of the circle, written as

$$(x_i - x_0)^2 + y_i^2 = R^2 = (f_0 + x_0)^2, \quad (8)$$

where (x_i, y_i) denote the points on the input arc, and R is the radius. It should be noted that where y_0 is set at zero is as Figure 3 indicates. Following the same notation for normalization with respect to focal length, one can derive

$$x_0 = \frac{1-f^2}{2(1-f \cos \alpha)},$$

$$x_0 = \frac{x_0}{f_0}.$$

It should be noted that the maximum scan angle of the lens can be other than the focal angle, α , as detailed in the literature [9, 10]. In this case, Equation (1) is modified such that

$$\begin{aligned}\overline{F_1 P} + w + y_a \sin \psi &= f + w_0, \\ \overline{F_2 P} + w - y_a \sin \psi &= f + w_0, \\ \overline{F_0 P} + w &= f_0 + w_0,\end{aligned}\quad (9)$$

where the maximum scan angle is now ψ . As before, the delay lengths can be expressed in terms of a second-order polynomial as in Equation (6). The coefficients of the polynomial need to be modified such that

$$\begin{aligned}a &= 1 - y_a^2 \gamma^2 - \frac{(1-f)^2}{(1-f \cos \alpha)^2}, \\ b &= -2 + 2y_a^2 \gamma^2 + \frac{2(1-f)}{1-f \cos \alpha} - \frac{y_a^2 \sin^2 \psi (1-f)}{(1-f \cos \alpha)^2}, \\ c &= -y_a^2 \gamma^2 + \frac{y_a^2 \sin^2 \psi}{1-f \cos \alpha} - \frac{y_a^4 \sin^4 \psi}{4(1-f \cos \alpha)^2},\end{aligned}\quad (10)$$

where

$$\gamma = \frac{\sin \psi}{\sin \alpha}.\quad (11)$$

The expressions for the output contour for this case are given as

$$\begin{aligned}x \triangleq \frac{x}{f_0} &= -\frac{\omega(1-f)}{(1-f \cos \alpha)} - \frac{y_a^2 \sin^2 \psi}{2(1-f \cos \alpha)}, \\ y \triangleq \frac{y}{f_0} &= y_a \left(1 - \frac{\omega}{f}\right) \gamma.\end{aligned}\quad (12)$$

We observe that there are six basic parameters that determine the size and specific shape of the input and output contours of the lens, as well as the lengths of the delay lines between the output walls and the linear-array element positions: the on-axis focal length (f_0), which is

also the lens width at the center; the focal angle (α); the focal ratio, $f = f/f_0$; the beam-angle-to-ray-angle ratio, $\gamma = \sin \psi / \sin \alpha$ ($= 1$ for the classical lens); the maximum beam angle, ψ ($= \alpha$ for the classical lens); and the array element spacing, d .

The lens shape is important in terms of the overall size and loss. Larger scan angles typically result in larger lens dimensions. Wide lenses can offer more-uniform path lengths but higher spillover loss. Compact lenses can minimize spillover loss; however, attention must be given in design to avoid asymmetric amplitude tapers. A detailed discussion of the design trades for Rotman lenses was provided in [9].

The equations provided above are fairly easy to solve using a simple algorithm. Therefore, it is straightforward to determine a first-order design for Rotman lenses. A more-reliable design would require verification and optimization for this initial set of parameters. This simplistic approach is based on simple ray optics, neglecting the multiple bounces from the lens walls, as well as the illumination and reception characteristics of the feed structures. In order to avoid multiple iterations in the design, more accurate tools are needed. Since Rotman lenses are electrically large structures (the parallel-plate region is often multiple wavelengths) with fine features (e.g., feeds), an exact numerical approach is problematic because of memory limitations. Some of the smaller lens structures are possible to simulate, and the Army Research Laboratory has found (after simulation) that the differences are not as pronounced as originally expected.

3. Rotman Lenses for Military Applications

The Army Research Laboratory has long been interested in battlefield sensors to facilitate operation of communication systems and multimode radar [11-13]. Common functions include secure point-to-point communications, active-protection combat identification, as well as networks for situational awareness and signal interception. Typically, each of these requires a separate antenna for the necessary RF transmission and reception. A desirable objective would be to have a common aperture for two or more of these functions, to reduce the count of antennas on a platform. The Rotman lens is an ideal candidate for these needs, as it is a wideband beam-former, allowing simultaneous functions to be integrated into a common array aperture [13].

This section is divided into two parts. First, a brief history of Rotman lens designs used for the Army applications will be discussed. The second part presents current state-of-the-art approaches, and recent designs involving three-dimensional scanning and flexible lens configurations, as well as future directions for the Army. Discussions of how to design and model Rotman lenses are also provided in the second part.

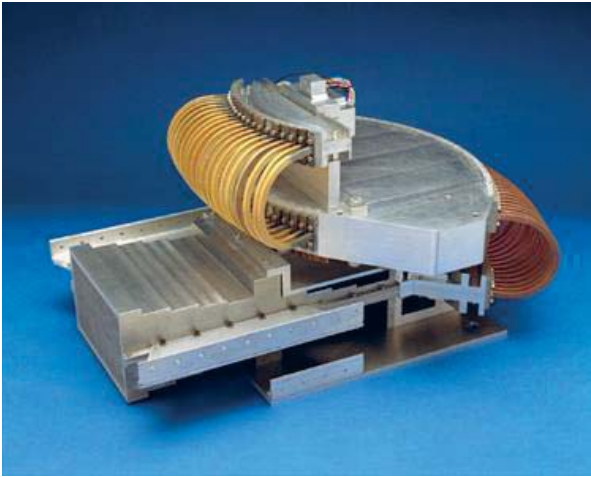


Figure 4. An early Rotman lens with sectoral-horn antennas.

3.1 A History of the Rotman Lens in Army Applications

An early version of one of the Army Rotman lens antenna arrays was provided to the Army Research Laboratory by the Georgia Tech Research Institute [14-15], shown in Figure 4. This design operated between 32 to 40 GHz. It consisted of 34 sectoral-horn antennas that were connected to the 34 array ports at the output of the Rotman lens, using U-shaped waveguides through an array-port manifold. The input consisted of 19 beam ports, which were also connected to a beam-port manifold using U-shaped waveguides. This configuration led to a reasonably compact configuration that allowed azimuth scanning. The Rotman lens was realized with a metallic cavity, allowing for a low insertion loss.

As mentioned earlier, the Rotman lens achieves scanning by an equivalent time delay created by the different path lengths to the radiating elements. These lengths depend on the relative positions between the beam port and the array ports on the structure. As long as the path lengths exhibit constant-time-delay behavior over the bandwidth, the lens is insensitive to the beam-squint problems exhibited by constant-phase beam-formers. Clearly, the waveguide transmission lines exhibit wave dispersion, counteracting the “true-time-delay” aspect of the Rotman. However, this

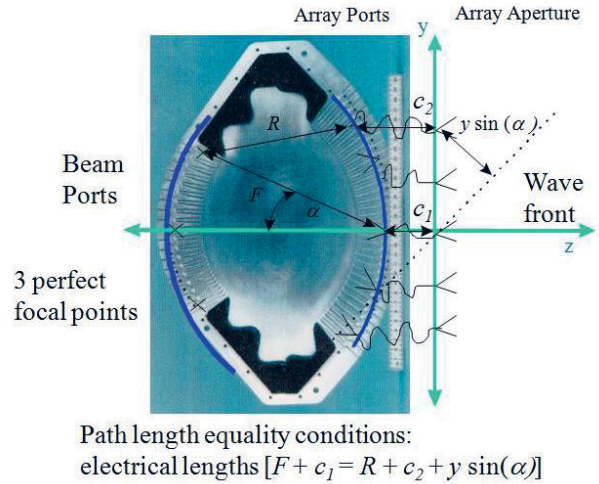


Figure 5. Further details of the prototype Rotman lens: a top view for the lower half.

dispersive effect was not found to be significant in this lens, which was essentially a proof-of-concept prototype.

Some further details of this lens can be seen in Figure 5, where a top view for the lower half of the lens is shown. The top half was identical, and rested on the lower half to create the waveguides for the ports and the parallel plate at the center. The three perfect focal points were at the center and the two extremes of the input (i.e., beam-port side) of the array. The output array of the lens was constructed to achieve a narrow beamwidth of 3° , and the lens allowed for a wide scan range of $\pm 22.5^\circ$. Absorber material was used on the sides to suppress reflections from the sidewalls of the lens.

Leveraging off of this work, the Army Research Laboratory and Georgia Tech further advanced this design with a follow-up version, as shown in Figure 6, and as described in further detail in [16-18]. This second prototype integrates the required transmission-line lengths into the structure, making a fully machined Rotman lens. As in the earlier design, there were 19 beam ports and 34 array ports. The use of waveguide for delay lines introduced a $\pm 4\%$ beam shift over a limited frequency range of 35 to 40 GHz. The lens was fabricated using Aluminum (alloy 6061-T6). It consisted of two symmetric halves that were aligned with each other to form the hollow cavity and the waveguide transmission lines.

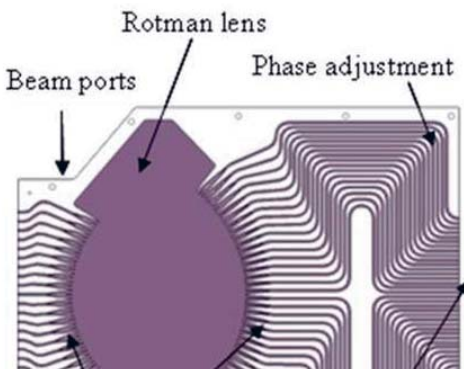


Figure 6. The second version of the Ka-band Rotman lens: integrated delay lines

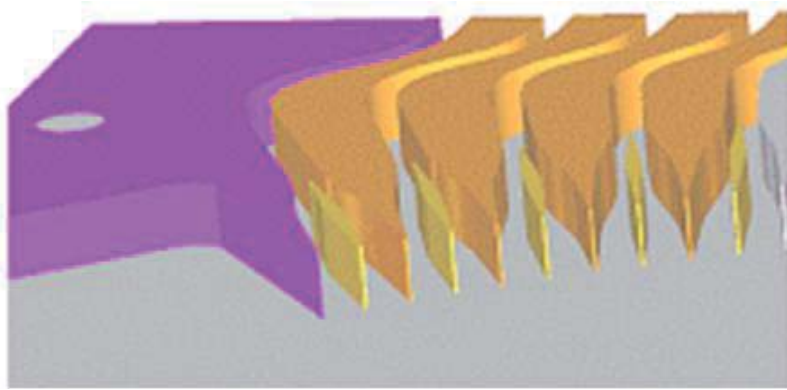


Figure 7. The waveguide-to-cavity transitions inside the Rotman lens.

It should be noted that only one of the symmetric halves is shown in Figure 6. It was determined that the fabrication tolerances for the side-to-side dimensions should be held to ± 0.003 in, while the depth should be limited to ± 0.005 in. Registration of the two symmetric halves was achieved through alignment pins, and electrical contact was ensured through the use of fourteen 1/4-20 bolts. Absorber material was placed as before at the sidewalls to mitigate unwanted reflections.

A notable complexity had to do with incorporating septums into the architecture, as shown in Figure 7. A view of the waveguide-to-cavity transitions shows a septum placed in the center to prevent unwanted modes from being excited in the waveguide. This also created the need for a combiner just behind the septum.

Originally, a Magic T was used as the power-combining mechanism just behind the septum. Unfortunately, this scheme required machining into the “floor” of the structure, and greatly increased the cost of production. A careful analysis by the Army Research Laboratory demonstrated that simple “T” combiners could be used instead of the Magic-T designs [16]. The key insight was that the phase difference over the “aperture” of any one port never

became pronounced enough to warrant the need for the Magic Ts. That is, the sides of the port were reasonably close in phase excitation, and the degradation was found to be minimal. This “small” change in the architecture resulted in significant savings in terms of complexity, cost, and fabrication time. The return- and transmission-loss performance of the new design is shown in Figure 8. For example, as long as the phase difference remained less than 30° , the impact on the transmission loss was negligible.

The performance of the lens with the simple T combiners was measured in the Army Research Laboratory anechoic chamber by simply using the ends of the waveguide as the radiating elements, and separately exciting each input. The resulting beam patterns for all the input ports are shown in Figure 9. As seen, the lens properly scanned with respect to the selected beam port. As the weighting for each element was essentially uniform, sidelobe levels on the order of 13 dB were expected and measured [16, 17].

The discussions so far have focused on cavity-based, parallel-plate lens designs. This design still tends to be heavy and large compared to printed lens approaches. Furthermore, three-dimensional fabrication processes are required for manufacturing, which adds to the cost. Printing

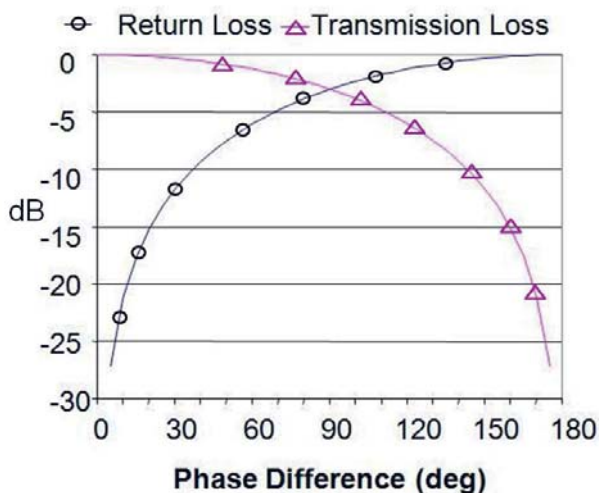


Figure 8. The performance of the folded T junctions as a function of the maximum phase mismatch (dB).

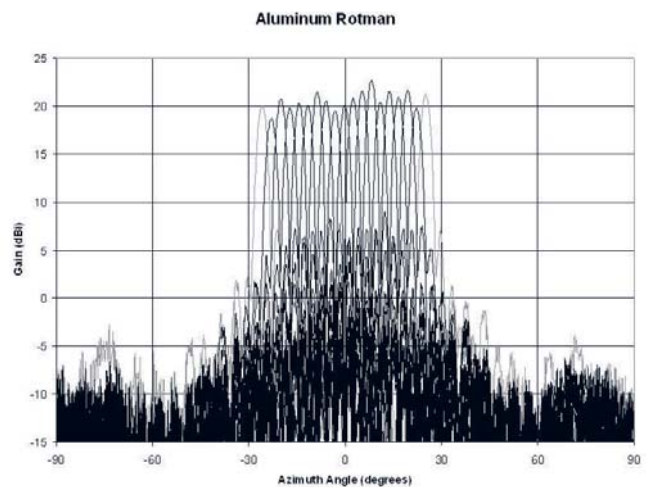


Figure 9. The measured radiation patterns of the Rotman lens with simple T combiners.

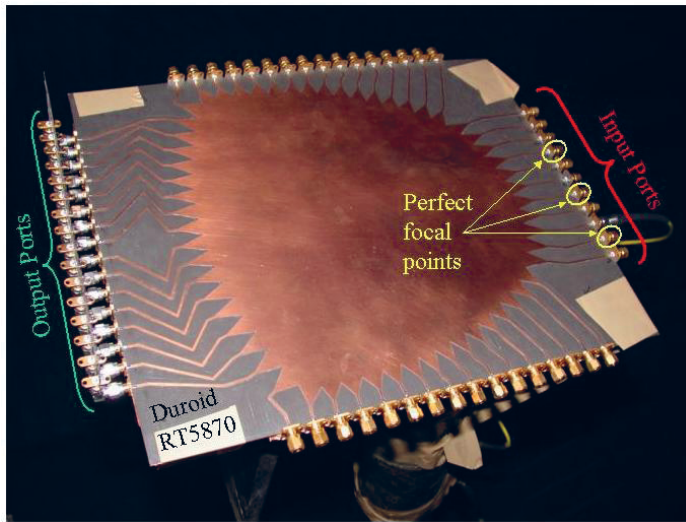


Figure 10. The Army Research Laboratory's first printed Rotman lens prototype, for Ku band.

the lens structure on a dielectric substrate reduces the cost, while the overall size is reduced as a direct function of the square root of the dielectric value of the substrate used. This miniaturization in size allows for stacking multiple lenses at the output ports of the current design, to allow for elevation scanning.

The Army Research Laboratory carried out initial designs of these lenses at Ku band to minimize cost for the prototype design. The first prototype was designed to operate between 12-18 GHz, using seven input ports to scan 20° with 16 output ports, as shown in Figure 10 [11, 12]. A 20-mil thick RT5870 Duroid substrate from Rogers was used to construct a microstrip lens. The overall dimensions of the lens were 30 cm by 35 cm. Power measurements compared to a standard horn suggested that the Rotman lens integrated with the 1×16 element patch array had about 9.5 dB loss at 17 GHz. This "hit" of about 6 dB in loss relative to the cavity design was a major tradeoff in cost. The 1×16 element patch array had a gain of 12 dBi at boresight.

This first prototype was designed using the simple set of equations as described in Section 2. No optimization was applied, and perfect ports were assumed. As Figure 11 shows, the performance was non-ideal, but nevertheless proved the concept of the printed-lens approach [18]. The sidelobe levels that crept up at the far side were due to chamber errors at the time of the measurements. However, a non-ideal peak-value distribution was observed for different input ports of the lens, indicating that the feeds needed to be better optimized and positioned for a better amplitude taper. Future designs improved significantly in performance by using better design tools, as will be seen in the sections that follow.

3.2 Current State-of-the-Art and Future Efforts for Rotman Lenses in Army Applications

This section provides an overview of the ongoing research efforts at the Army Research Laboratory,

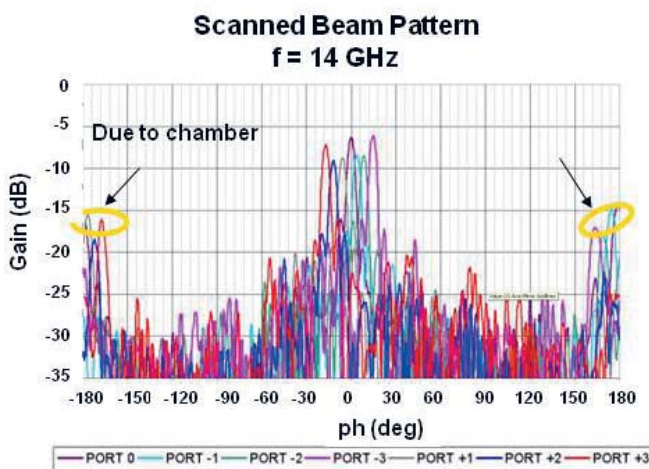


Figure 11a. The performance of the first prototype printed lens: the scanned beam positions

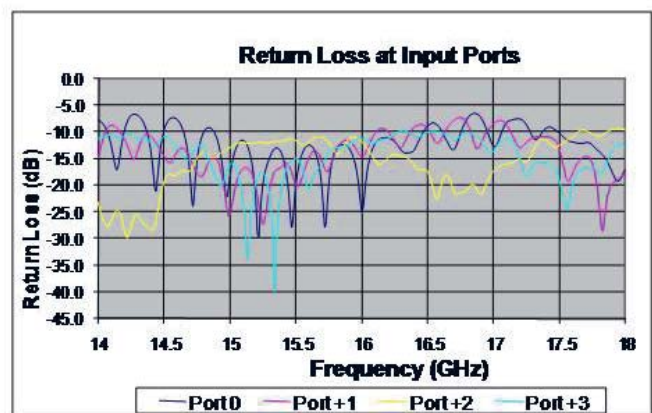


Figure 11b. The performance of the first prototype printed lens: the return loss for different input ports.



Figure 12. A Ka-band cavity Rotman lens made from Ultem 1000, and then gold plated.

leveraging the past work discussed above. The cavity lens approach is attractive, due to the lower loss achieved by the air-filled waveguide and parallel-plate structures. The printed lens has merits due to the compact size, at the expense of higher losses. The Army Research Laboratory continues to pursue both approaches, and progress in both areas is presented in this section.

3.2.1 Cavity Lens Design

To further reduce the cost and weight of the cavity design, the Army Research Laboratory decided to make this structure from plastic with a conductive coating. The machining was performed at the Army Research Laboratory using Ultem 1000 resin from GE Plastics. The structure was then plated with gold to achieve metallization, as shown in Figure 12. This was for a proof-of-concept design. Less-expensive plating would need to be used for any significant volume of production. The plating approach allowed a 60% reduction in weight, dropping it from 14.65 lbs to 6.05 lbs [19].

The radiated patterns for this Rotman lens were measured (Figure 13) for comparison to the earlier results (Figure 9). The results actually showed a significant improvement in the pattern, with a smooth decrease in peak power as the beam scanned from broadside, in agreement with theory. It should be noted that the Rotman is actually two mirror images that are secured together. The improvement in performance over the aluminum lens was attributed to better contact achieved between the waveguide transmission lines and the cavity, itself. The aluminum lens was a far more rigid structure, and the loss of continuity between the two halves was felt to be more pronounced, accounting for the degraded patterns.

With the concept of a plastic Rotman lens validated, the remaining work is to injection mold the structure, and plate with less-expensive conducting material. These two steps will significantly lower the cost, and make the Rotman lens suitable for high-volume use.

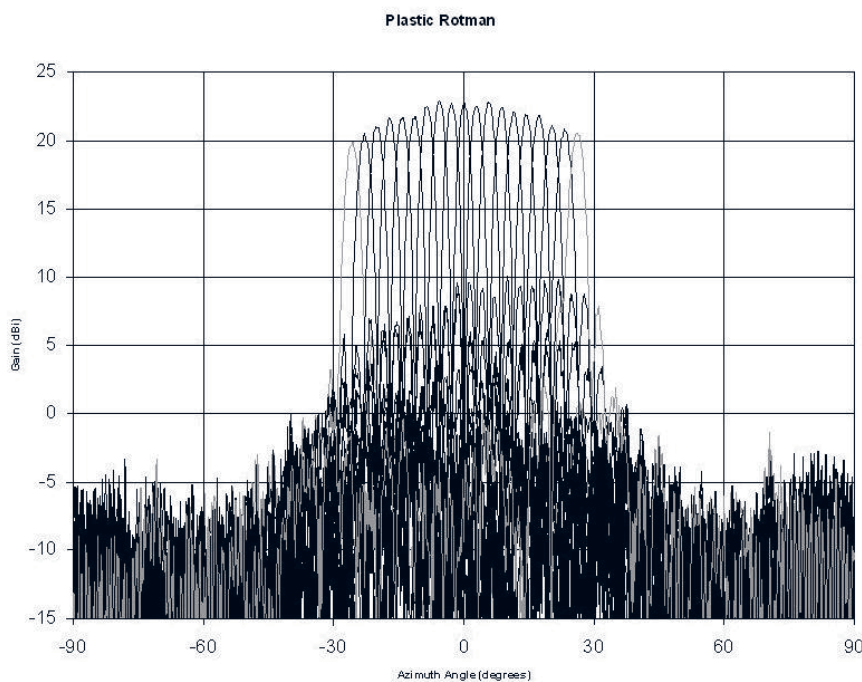


Figure 13. The measured azimuth patterns for the plastic Rotman lens.

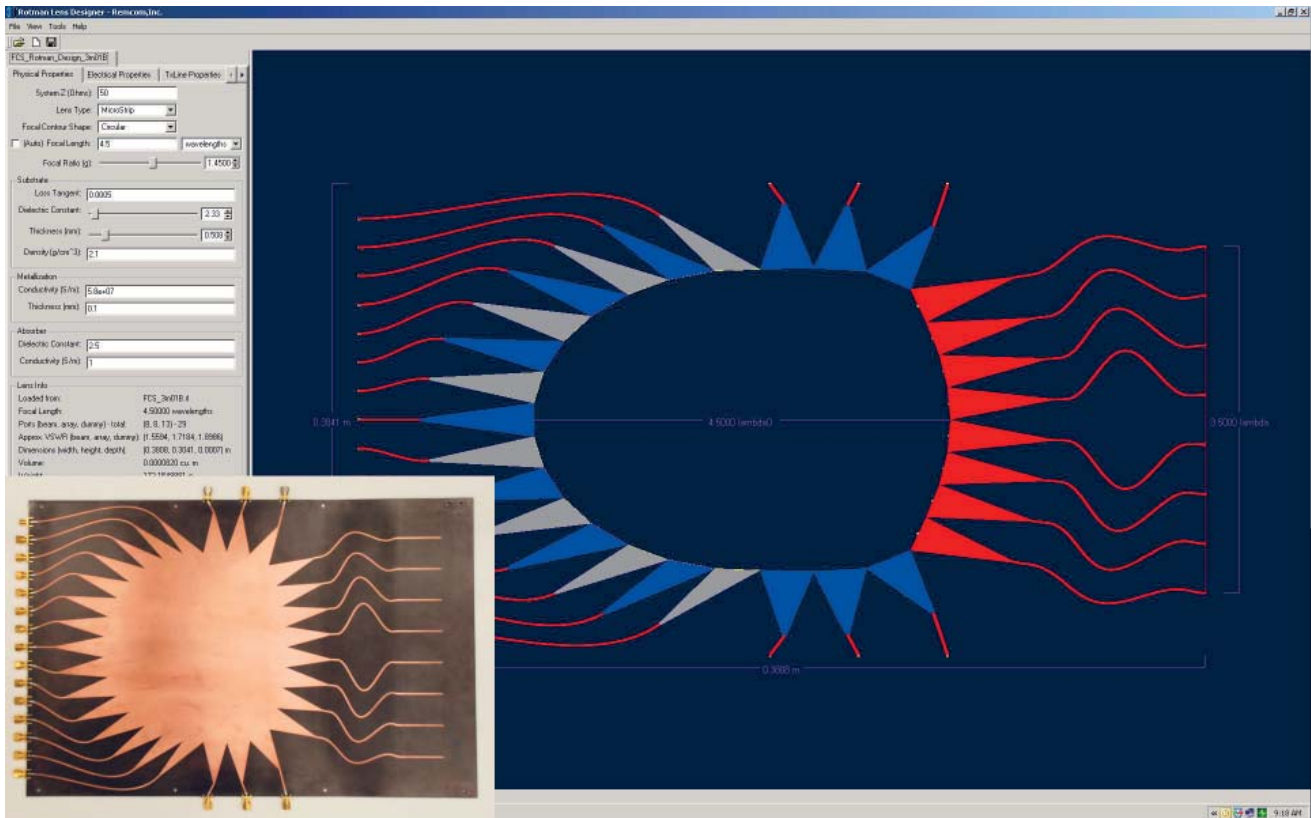


Figure 14. The Rotman lens design software's front-end interface.

3.2.2 Modeling Microstrip Lenses

The modeling tool currently being used by the Army Research Laboratory was developed by REMCOM under an SBIR contract with the Army. This software package combines Rotman's equations with Geometrical Optics (GO), producing an interactive package that allows the user to adjust a variety of parameters (number of ports, the focal ratio, alpha ratio, port size, etc.) in real time [20].

Direct and singly reflected waves are taken into account by the software, as are dielectric losses, allowing the port-voltage standing-wave ratio (VSWR) to be approximated. Transmission-line losses are also calculated. A typical screen shot of the software is shown in Figure 14, in conjunction with the picture of the actual lens based on it. This software is meant to enhance the initial (first-cut) simulations, as originally provided by Rotman. Full-wave analysis tools are then needed to take into account "real-world" effects, such as reflections off the walls and other ports.

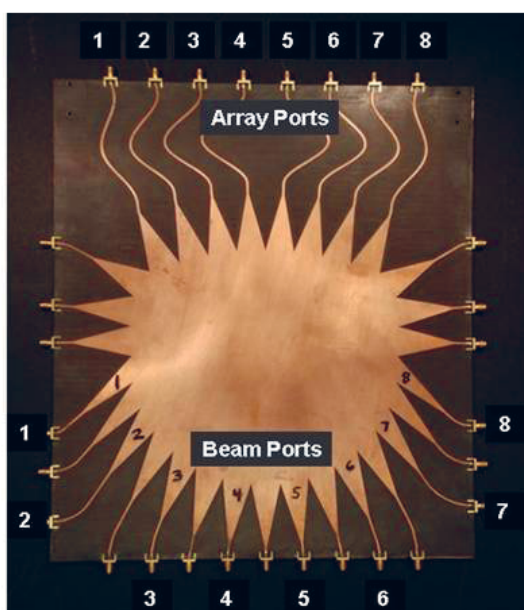


Figure 15a. The C-band printed Rotman lens.

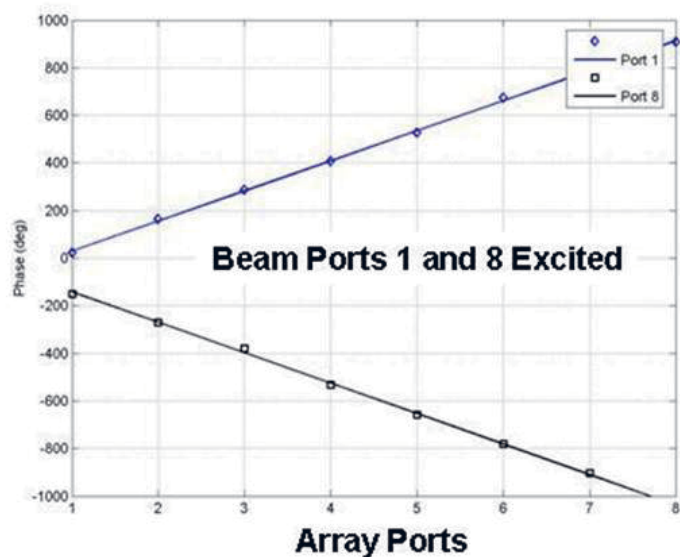


Figure 15b. The measured phase of the C-band printed Rotman lens for input ports 1 and 8 at 4.6 GHz.

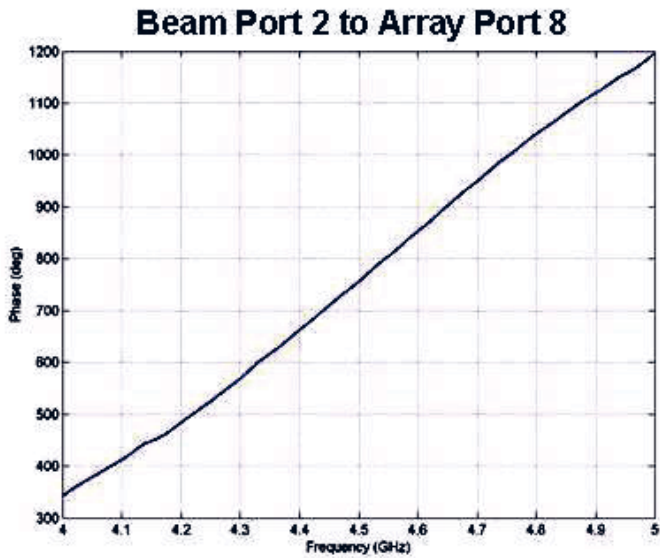


Figure 16. The measured phase shift between beam port 2 and array port 8 as a function of frequency.

3.2.3 Printed Lens Design

As a continuation of the Ku-band prototype of the printed lens design, the Army Research Laboratory designed a C-band lens, operating between 4.5 and 5.0 GHz, using the simulation package *RLD*, as described above. The substrate used was RT Duroid 5870, with a relative dielectric value of 2.33, and a thickness of 20 mils. The overall dimensions of the lens were 12 in by 18 in. The scan range was $\pm 45^\circ$ degrees, using eight input ports with the array-port aperture supporting a beam of approximately 12° in width. This desired scan was achieved by the placement of beam ports 1 to 8 along the beam's contour. Dummy ports were placed between each numbered port on the beam side. These ports (if used) would allow scanning to intermediate beam positions between any two beams.

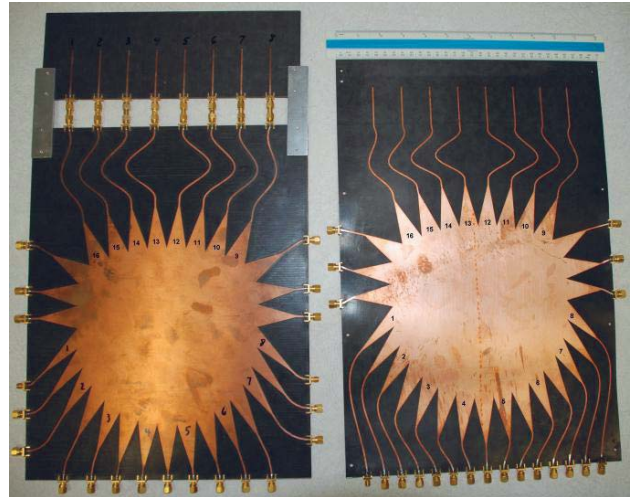


Figure 17. A Rotman lens with a separate antenna array, and a follow-on version with an integrated lens and array.

If each beam port had included the arc length occupied by the dummy position, the increased aperture size would have introduced significant phase errors across the receptor ports on the array side of the structure. Figure 15 shows the picture of the C-band Rotman lens and its performance for the measured phase shift (at a fixed frequency) at the array ports, when either beam-port 1 or beam-port 8 was excited. The desired progressive phase shift between array ports was evident. A linear phase change between any beam and array port as a function of frequency should have been found when measured, if this Rotman lens was a time-delay beam-former. Such measurements were taken for validation, as shown in Figure 16. The agreement between the *RLD* software and measured data was very good with respect to the main-beam position and the sidelobe levels [21]. More-extensive full-wave simulations were undertaken by the Army Research Laboratory [21], confirming the good performance of the *RLD* software.

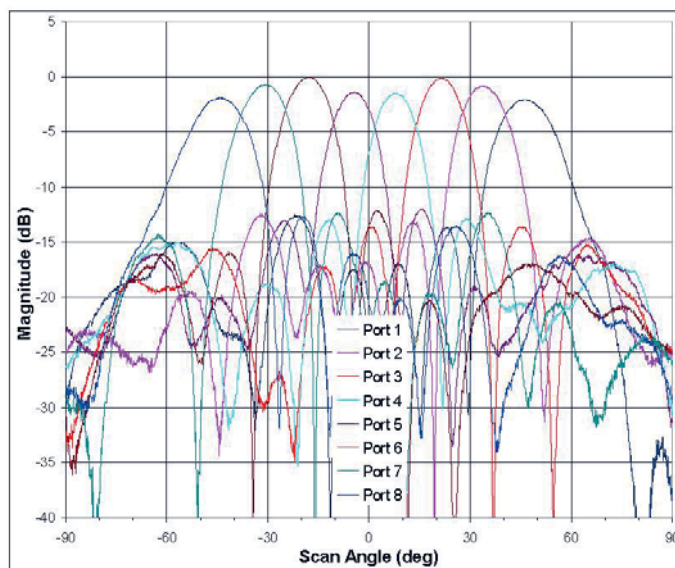


Figure 18. The measured radiation patterns for the integrated Rotman lens and patch antenna array.

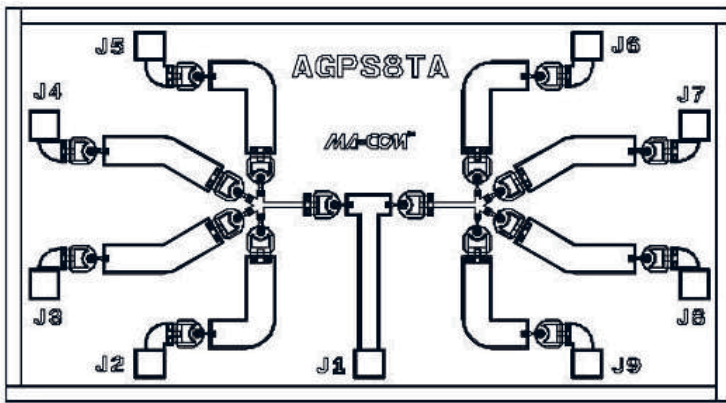


Figure 19a. The MA4AGSW8-1 SP8T switch.

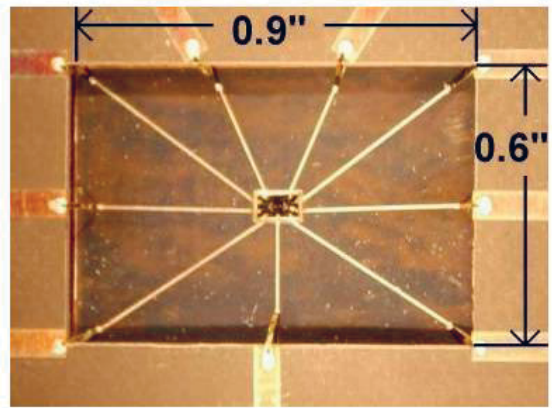


Figure 19b. The switch surrounded by CuFlon, measuring 0.9 in \times 0.6 in \times 0.002 in.

With the phase characteristics of the C-band Rotman lens design fully measured, the next step was the integration of the patch antennas into the design, to act as the radiation elements. The initial integration used a separate lens and array, connected with SMA barrels. This initial design yielded reasonable radiation-pattern results. A follow-on version integrated the lens and the antenna array into a common structure. Both versions are shown in Figure 17. The radiation patterns for the integrated array are given in Figure 18. A small dip in the measured power for the two beams that were directed to the front of the radiating aperture was observed. We attributed this slight (2 dB) loss in gain to reflections off the imperfectly absorbing sidewalls. The measured gain of these two beams was found to be 8.75 dBi.

The full integration required a 1 \times 8 switch for electronic scanning [23]. M/A-COM's (94 mil \times 51 mil) MA4AGSW8-1 SP8T was selected for this design, because of its low insertion loss (2 dB max) and speed of operation (typically, 20 ns). Narrow microstrip transmission lines were

needed to reach the small pads of the switch, requiring the dielectric material surrounding the switch to be very thin. This was accomplished by placing dielectric material (2 mils in thickness) measuring 0.9 in \times 0.6 in around the switch, as seen in Figure 19. Note that a small rectangular area of dielectric at the center was removed to accommodate the switch placement. The dielectric material was CuFlon (a product of Polyflon Corp.). A conductive epoxy was used to bond the CuFlon to a 1.1 in \times 0.8 in copper ground plane. The switch was next conductively bonded to the same ground plane in the rectangular donut hole of CuFlon. Conductive epoxy was used to hold the wire bonds from the Cu transmission lines on the CuFlon substrate to the gold pads on the MA4AGSW8-1. Afterwards, this 1.1 in \times 0.8 in module was soldered underneath the Rotman Lens antenna array design to establish ground-plane continuity. The final step in the fabrication process connected the thicker transmission lines of the Rotman lens to the thin lines on the 2 mil thick dielectric using wire bonds and conductive epoxy, as shown in Figure 20.

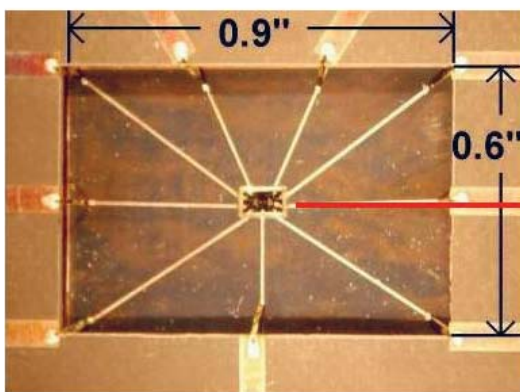
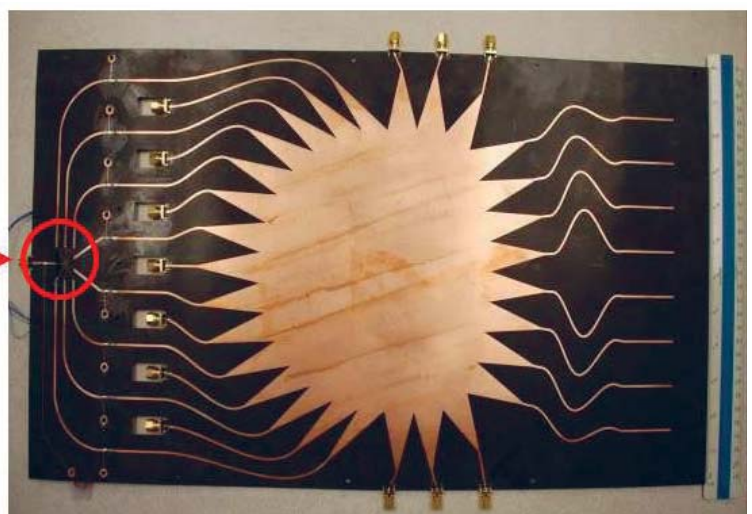


Figure 20. The integration of the switch into the Rotman lens beamformer.



Beam	1	2	3	4	5	6	7	8
Gain (dBi)	8.19	8.00	10.02	7.34	8.41	9.94	8.52	9.15

Table 1. The measured system gain for each beam (beamformer and switch losses included).

The measured gains for this integrated design are given in Table 1. However, the difficulty of integrating the switch did cause some discrepancies, due to the transition between the 20 mil-thick material and the 2 mil-thick material. The insertion loss of this entire beamformer, including the switch, was on the order of 9 dB.

The completion of this prototype utilized the fact that the 20 mil substrate material was reasonably flexible. The patch antenna layer needed to reside on 60 mil thick Duroid, and was not flexible. As there was no need to keep the patch material over the entire extent of the Rotman Lens, it became possible to bend the Rotman lens, as seen in Figure 21. This lens was measured with a 90° bend, and no loss in performance was observed [24].

4. Future for Rotman Lenses and Conclusions

Many radar and communications applications benefit from simultaneous electronic scanning of multiple beams via an array antenna. This paper investigated Rotman lenses

as beamformers to linear array antennas for applications of the US Army. Due to the inherent broadband characteristics and simple yet elegant design concept, Rotman lenses offer a suitable platform for electronic scanning, and have been investigated by the Army Research Laboratory for more than a decade. A brief history of the prototypes developed at the Army Research Laboratory and the current state-of-the-art has been discussed.

Rotman lens beamformers remain an attractive option for applications involving platform-integrated arrays for the Army. The arrays are simple to implement and have very desirable features, such as their low profile, low cost, and reasonably wide field of view [25], using flexible array configurations. There are a few challenges that need to be overcome for the military requirements. First, the original lens design is for two-dimensional scanning, using a linear array. Army applications typically require three-dimensional scanning capability. It has been shown that these structures can achieve full 360° scanning with some added complexity [26, 27]. The focus of the future objectives for Rotman lens applications for the Army is foreseen as the full field of view, i.e., 360° scanning and compact size.



Figure 21. The flexible electrically scanned Rotman lens on a platform.

The second issue is that Rotman lenses are electrically large structures, especially for the cavity design, which offers the lowest loss. More compact sizes are desirable for low visibility and reduced weight, to enable ease of deployment. These needs may be resolved by using printed lenses, as discussed, or by exploring the use of advanced RF materials in the cavity structure. Possible research topics of interest are the reduction of the lens size by the use of engineered materials, such as metamaterials [28]. Metamaterials tend to be very bandlimited. A tradeoff study would have to be undertaken to determine if size reductions are desirable at the expense of wideband performance.

Finally, since the lens is an electrically large structure with fine features, reliable modeling tools that don't have excessive running times are necessary. The accurate modeling of the lens structure remains a point of interest for the Army. The Army Research Laboratory has invested in the development of hybrid tools, as discussed in this paper. Recently, the possibility of enabling full-wave simulations on hardware-accelerated platforms has been investigated by one of the authors, with early promising results using the Finite-Difference Time-Domain (FDTD) method [29]. Such techniques have been slowly finding their way into the scientific community, and some tools already have been developed for the use of the electromagnetics community [30-32]. These platforms can be effectively utilized for optimizing the lens design, as they enable rapid computations for full-wave analysis without sacrificing accuracy, which can be expected in some hybrid approaches.

5. References

1. W. Rotman and R. F. Turner, "Wide-Angled Microwave Lens for Line Source Applications," *IEEE Transactions on Antennas and Propagation*, **AP-11**, 6, 1963, pp. 623-632.
2. H. Gent, "The Bootlace Aerial," *Roy. Radar Est. J.*, **40**, 1957, pp. 47-57.
3. J. B. Shelton, "Focusing Characteristics of Symmetrically Configured Bootlace Lenses," *IEEE Transactions on Antennas and Propagation*, **AP-26**, 4, 1978, pp. 513-518.
4. T. Katagi, S. Mano and S. Sato, "An Improved Design Method of Rotman Lens Antennas," *IEEE Transactions on Antennas and Propagation*, **AP-32**, 5, 1984, pp. 524-527.
5. D. R. Gagnon, "Procedure for Correct Refocusing of the Rotman Lens According to Snell's Law," *IEEE Transactions on Antennas and Propagation*, **AP-37**, 3, 1989, pp. 390-392.
6. K. K. Chan and S. K. Rao, "Design of a Rotman Lens Feed Network to Generate a Hexagonal Lattice of Multiple Beams," *IEEE Transactions on Antennas and Propagation*, **AP-50**, 8, 2002, pp. 1099-1108.
7. M. C. D. Maddocks and M. S. Smith, "Flat-Plate Steerable Antennas for Satellite Communications and Broadcast Reception," *Proceedings of IEE on Microwaves, Antennas and Propagation H*, **138**, 1991, pp. 159-168.
8. O. Kilic and R. Dahlstrom "Rotman Lens Beam Formers for Army Multifunction RF Antenna Applications," 2005 IEEE International Symposium on Antennas and Propagation *Digest*, Washington, DC, **2B**, July 2005, pp. 43-46.
9. R. C. Hansen, "Design Trades for Rotman Lenses," *IEEE Transactions on Antennas and Propagation*, **AP-39**, 4, 1991, pp. 464-472.
10. P. S. Simon, "Analysis and Synthesis of Rotman Lenses," Proceedings of the 22nd AIAA International Communications Satellite Systems Conference & Exhibit, May 2004, Monterey, CA.
11. O. Kilic and S. Weiss, "Dielectric Rotman Lens Design for Multi-Function RF Antenna Applications," 2004 IEEE International Symposium on Antennas and Propagation *Digest*, Monterey, CA, **1**, 2004, pp. 659-662.
12. O. Kilic, "Dielectric Rotman Lens Alternatives for Broadband Multiple Beam Antennas in Multifunction RF Applications," Proceedings of the 24th Army Science Conference, Orlando, FL, November 2004.
13. S. Weiss, R. Dahlstrom, O. Kilic, E. Viveiros, S. Tidrow, F. Crowne and E. Adler, "Overview of the Multifunction RF Effort - An Army Architecture for an Electronically Scanned Antenna," Proceedings of the 2002 Antenna Applications Symposium, pp. 119-129.
14. E. O. Rausch, A. F. Peterson and W. Wiebach, "A Low Cost, High Performance, Electronically Scanned MMW Antenna," *Microwave Journal*, **40**, 1, 1997, pp. 20-32.
15. E. O. Rausch, A. F. Peterson and W. Wiebach, "Millimeter Wave Rotman Lens," Proceedings of the 1997 IEEE National Radar Conference, May 1997, pp. 78-81.
16. S. Weiss, R. Dahlstrom, O. Kilic, E. Viveiros, S. Tidrow, F. Crowne, and E. Adler, "Overview of the Multifunction RF Effort - An Army Architecture for an Electronically Scanned Antenna," Proceedings of the 2002 Antenna Applications Symposium, pp. 119-129.
17. R. Dahlstrom, S. Weiss, E. Viveiros, A. Bayba and E. Adler, "A Ka-Band Electronically Scanned Antenna for Multi-Function RF Applications," Proceedings of the 2003 Antenna Applications Symposium, pp. 360-372.
18. R. Dahlstrom and O. Kilic, "Enhanced Ka-Band Electronically Scanned Antennas with Multi-Function RF Capability," Proceedings of the 2004 Antenna Applications Symposium, pp. 264-278.
19. S. Weiss and R. Dahlstrom, "Rotman lens Development at the Army Research Lab," Proceedings of the IEEE AESS Conference, Big Sky, MT, March 2005.
20. C. Penney, "Rotman Lens Design and Simulation in Software," *IEEE Microwave Magazine*, **9**, 2008, pp. 138-149.
21. S. Weiss, S. Keller and C. Ly, "Development of Simple Affordable Beamformers for Army Platforms," Proceedings of the GOMACTech-07 Conference, Lake Buena Vista, FL, March 2007.
22. J. Dong, A. Zaghoul, R. Sun, D. J. Reddy and S. Weiss, "Rotman Lens Amplitude, Phase, and Pattern Evaluations by Measurements and Full Wave Simulations," *ACES Journal*, **24**, 2009, pp. 567-576.
23. T. Anthony, "Rotman Lens Development," 2008 IEEE International Symposium on Antennas and Propagation *Digest*, San Diego, CA, June, 2008, pp. 1-4.

24. T. Anthony and S. Weiss, "Development of a Flexible Electrically-Scanned Array using a Rotman Lens," Proceedings of the XXIX URSI General Assembly, Chicago, IL, August, 2008.
25. C. M. Rappaport and A. I. Zaghoul, "Optimized Three-Dimensional Lenses for Wide-Angle Scanning," *IEEE Transactions on Antennas and Propagation*, **AP-33**, 11, 1985, pp. 1227-1236.
26. R. E. Clapp, "Extending the R-2R Lens to 360 Degrees," *IEEE Transactions on Antennas and Propagation*, **AP-32**, 7, 1984, pp. 661-671.
27. A. I. Zaghoul and J. Dong, "A Concept for Lens Configuration for 360-Degree Scanning," *IEEE Antennas and Wireless Propagation Letters*, **8**, 2009, pp. 985-988.
28. A. I. Zaghoul, Y. Lee and S. Weiss, "Measurements of Refraction Focusing Using Negative-Refractive-Index Metamaterials," USNC/URSI National Radio Science Meeting, San Diego, California, July 2008.
29. O. Kilic, M. Mirotznik and J. Durbano, "Application of FPGA Based FDTD Simulators to Rotman Lenses," Proceedings of the 22nd Annual Review of Progress in Applied Computational Electromagnetics Society, Miami, FL, 2006.
30. O. Kilic and D. Barger "Field Programmable Gate Array Acceleration of Bio-Inspired Optimization Techniques for Phased Array Design," 2009 IEEE International Symposium on Antennas and Propagation *Digest*, Charleston, SC, June 2009, pp. 1-4.
31. M. J. Inman and A. Z. Elsherbeni, "GPU Acceleration of Linear Systems for Computational Electromagnetic Simulations," 2009 IEEE International Symposium on Antennas and Propagation *Digest*, Charleston, SC, June 2009, pp. 1-4.
32. M. J. Inman and A. Z. Elsherbeni, "Optimization of GPU Codes for FDTD Simulations," Proceedings of the 25th Annual Review of Progress in Applied Computational Electromagnetics Society, Monterey, California, March 2009.

Four Decades of Space-Borne Radio Sounding



Robert F. Benson

Abstract

A review is given of the 38 rocket, satellite, and planetary payloads dedicated to ionospheric/magnetospheric radio sounding since 1961. Between 1961 and 1995, eleven sounding-rocket payloads from four countries evolved from proof-of-concept flights to sophisticated instruments. Some involved dual payloads, with the sounder transmitter on one and the sounder receiver on the other. The rocket sounders addressed specific space-plasma-wave questions, and provided improved measurements of ionospheric electron-density (N_e) field-aligned irregularities (FAI). Four countries launched 12 ionospheric topside-sounder satellites between 1962 and 1994, and an ionospheric sounder was placed on the Mir Space Station in 1998. Eleven magnetospheric radio sounders, most of the relaxation type, were launched from 1977 to 2000. The relaxation sounders used low-power transmitters, designed to stimulate plasma resonances for accurate local N_e determinations. The latest magnetospheric sounder designed for remote sensing incorporated long antennas and digital signal processing techniques to overcome the challenges posed by low N_e values and large propagation distances. Three radio sounders from three countries were included on payloads to extraterrestrial destinations from 1990 to 2003. The scientific accomplishments of space-borne radio sounders included (1) a wealth of global N_e information on the topside ionosphere and magnetosphere, based on vertical and magnetic-field-aligned N_e profiles; (2) accurate *in-situ* N_e values, even under low-density conditions; and (3) fundamental advances in our understanding of the excitation and propagation of plasma waves, which have even led to the prediction of a new plasma-wave mode.

1. Introduction

Table 1 provides a summary of the 38 rocket, satellite, and planetary payloads from eight countries (US, Canada, France, USSR, Norway, Japan, Sweden, and Italy) dedicated to ionospheric, magnetospheric, and planetary radio

sounding, launched between 1961 and 2003. It indicates that the first radio sounding in space was performed from a US rocket launched on June 24, 1961, following the successful US rocket antenna-deployment test of June 14, 1961. These two rockets were followed by a US rocket flight into a disturbed ionosphere on October 31, 1961.

The first ionospheric sounding from a satellite was from the Canadian-built and US-launched Alouette 1. It was launched on September 29, 1962. It also established another first: the first satellite to be launched from the Western Test Range in California. It was the first satellite in the highly successful International Satellites for Ionospheric Studies (ISIS) program. The program, which included an additional eight countries (Australia, Finland, France, India, Japan, New Zealand, Norway, and the UK), included six satellites. Five of these satellites contained topside sounders. Four of the sounding satellites were Canadian-built and US-launched, and contained swept-frequency sounders (Alouette 1 and 2 and ISIS 1 and 2). The other two satellites in the program were built by the US (Explorer 20 and Explorer 31). Explorer 20 contained a topside sounder that operated on six fixed frequencies. This mode of operation proved to be so valuable for the investigation of N_e gradients and plasma resonances that it was included in the design of the sounders on ISIS 1 and 2. Explorer 31, also known as Direct Measurements Explorer-A (DMEA), was launched piggyback with Alouette 2. This dual-satellite mission was known as ISIS X. Explorer 31 demonstrated the compatibility of radio-sounder operations and *in-situ* measurements. The last satellite in the ISIS program, ISIS 2, was a complex observatory that included the first two auroral imagers in orbit. It demonstrated the compatibility of such imaging from a spinning satellite containing long sounder antennas.

The USSR and Japan launched an additional seven topside sounding satellites (Cosmos 381, ISS A and B, Intercosmos 19, EXOS C, Cosmos 1809, CORONAS 1) between 1970 and 1994. Cosmos 381 followed the launch of Cosmos 318 in 1969 that failed due to a rocket problem. The Cosmos 381 sounder, which was a pulsed sounder

Robert Benson is with the Geospace Physics Laboratory (Code 673), NASA Goddard Space Flight Center, Greenbelt, Maryland 20771, USA; Tel: +1 (301) 286-4037; Fax: +1 (301) 286-1433; E-mail: robert.f.benson@nasa.gov.

This is an invited Review of *Radio Science* from Commission H.

Table 1. A summary of space-borne radio sounders*.

Date	Country	s/c	T	Freq	Dp (m)	P (W)	Sounder Experiment and Comments	Sample Results and Reference
06/14/61	US	r			75	no tx	Antenna deployment test from spinning s/c	Successful demonstration [1]
06/24/61	US	r	s	f	32	3	4.07 & 5.97 MHz, 22 pps, 1,060 km apogee	1 st topside sounding, quiet [2]
10/31/61	US	r	s	f	32	3	4.07 MHz, 22 pps, 1,070 km apogee	t/s sounding of spread F [3]
09/29/62	Canada	s	s	s	23, 46	100	Alouette 1, (0.5-12) 63 pps, 1,000 km polar	1 st Global $N_e(h)$ t/s profiles [4]
08/25/64	US	s	s	f	19, 37	45	Exp. XX, 6 freq (1.5 to 7.22), 3 dp at 60°	N_e & res at 800 km polar [5, 6]
11/29/65	Canada	s	s	s	23, 73	300	Al. 2, (0.1-14.5), 30 pps, 500-3,000 polar	Compare <i>in-situ</i> techniques [4]
01/30/69	Canada	s	s	f/s	19, 73	400	ISIS 1, (0.1-20), 30 pps, 550-3,500 polar	More high-alt sound., AKR [4]
10/06/70	France	r	r	s	4	low	EIDI 1, 1-11 MHz in 0.4 s, 500 pps	3 f_{UH} res: 2 waves 1 kHz apart [7]
10/22/70	France	r	r	s	4	low	EIDI 2, 2 nd of 3 rocket relax sounders	Results given for EIDI 1 & 3 [8]
12/20/70	USSR	s	s	f	18	100	Cosmos 381, 985-1023 km, 74° inclination	N_e irreg. related to obs. UV [9, 10]
04/01/71	Canada	s	s	f/s	19, 73	400	ISIS 2, (0.1-20), 45 pps, 1,400 km polar	Compatible/w imagers, etc. [4]
06/25/71	US	r	r	s	10	60	0.5-4.5 MHz in ~ 4 s, 50 pps, waveform tel	f_T res freq variation obs. [11]
01/13/72	Norway	r	r	s	5	low	Mother-Daughter, 1.1-9 MHz, 192 km apog	Res identified as cone res [12]
02/06/73	Norway	r	r	s	8	low	Mother-Daughter, 0.8-5 MHz, 260 km apog	Cone & other res observed [13]
02/17/73	France	r	r	s	4, 8	2	EIDI 3, 0.44-5.52 MHz in 4 s, 10 ms listen	N_e irreg from f_N res [14]
02/29/76	Japan	s	s	s	11, 37	n/a	Ionosphere Sounding Satellite (ISS)-A	One month lifetime
04/20/77	France	s	r	s	42	low	GEOS 1, 0.3-77 kHz in 256 300 Hz steps	Magnetospheric N_e , 5-7 R_E , [15]
10/22/77	France	s	r	s	215	low	ISEE 1 (mother) w/sounder & 2 (daughter)	Magnetospheric N_e [16]
02/16/78	Japan	s	s	s	11, 37	150	ISS B, (0.5-14.8), 9 & 64 pps, 972-1220 km	Global maps of foF, [17]
07/14/78	France	s	r	s	42	low	GEOS 2, 0.3-77 kHz in 256 300 Hz steps	Plasmapause N_e features [18]
09/16/78	Japan	s	r	s	73,102	300	EXOS B (Jikiken), (.02-3), 227-30051 km	Plasmapause N_e irreg. [19]
02/27/79	USSR	s	s	s	15, 50	300	Intercosmos 19, 0.3-15.9 MHz in 5.8 s	Sounder-accel. electrons [20]
02/14/84	Japan	s	s	s	40	300	EXOS C (Ohzora), (0.1-16.0), 354-865 km	Wave-mode conversion [21]
02/22/86	Fran/Swed	s	r	s	80	low	V4H on Viking, 8-500 kHz in 3 freq. bands	N_e , plasmasphere & polar cap [22]
12/18/86	USSR	s	s	s	15,50	300	Cosmos 1809, (0.3-15.95), 58.6 pps	Freq. of sound-acc electrons [23]
01/30/89	Canada	r	s	s	4.4, 5.5	2	OEDIPUS A, 0-5 MHz bi-static sounder	Guided Z-mode propagation [24]
02/22/89	Japan	s	s	s	60	600	EXOS D (Akebono) 0.3-11.0, 10500 km ap.	Magnetosph. ducted echoes [25]
10/06/90	US/France	p	r	s	72	low	URAP on Ulysses, (0-50 kHz)	N_e in Io plasma torus [26-28]
03/03/94	USSR	s	s	s	15	n/a	CORONAS 1, 500 km, 82.5° inclination	Upper-hybrid emission band [29]
11/07/95	Canada	r	s	s	4.4, 5.5	10	OEDIPUS C, 0.1-8 MHz bi-static sounder	<i>In-situ</i> Faraday-rotation [30]
10/15/97	US/France	p	r	s	20	low	RPWS on Cassini, 3.6-115.2 kHz in 90 steps	N_e in vicinity of Saturn [31]
08/ /98	USSR	s	s	s	n/a	n/a	Orbital Complex (OC) on Mir Space Station	Sounding below F peak [32]
03/25/00	US	s	s	s	500, 20	10	IMAGE/RPI, (.003-3 MHz), tuned tx ant.	2D F-A N_e structures [33, 34]
07&08/00	France	s	r	s	88	low	WHISPER on 4 Cluster s/c, 2-80 kHz	Multipoint magnetospheric N_e [35]
06/02/03	Italy/US	p	s	s	40	5	MARSIS on Mars Express	Radio sounding of Mars iono [36]

*The date is the month/day/year of launch; s/c indicates that the spacecraft was either a rocket (r), satellite (s), or space probe (including a satellite around another planet) (p); T indicates the type of sounding, i.e., either a low-power relaxation sounder (r) for resonances or long-range sounding (s); Freq indicates that the sounding was at one or more fixed frequencies (f) or was a swept-frequency sounder (s); Dp (m) indicates the tip-to-tip length of the sounder dipole antenna(s) in meters; P (W) indicates the estimated peak radiated pulse power in watts; n/a indicates that the information could not be located by the author.

using 20 fixed frequencies, was noteworthy for at least two reasons. First, the sounder design team was awarded the silver medal of the Moscow Exhibition of National Achievements. Second, one member of the design team (A. I. Galkin) was the father of I. A. Galkin, who is a key member of the sounder on the IMAGE satellite known as the Radio Plasma Imager (RPI), to be discussed below. In 1998, the USSR placed a radio sounder on the Mir Space

Station. It was the first ionospheric sounder to be placed in orbit near the altitude of the N_e maximum, h_{max} .

From 1970 to 1995, eight ionospheric-sounding rockets built by four countries (France, US, Norway, and Canada), including four dual payloads (two each from Norway and Canada) were launched to investigate wave propagation and plasma resonances. The two French

rocket sounders launched in October 1970 were the first to telemeter the sounder-receiver waveform to the ground for plasma-resonance investigations. The US rocket sounder launched in June 1971 also transmitted the sounder-receiver waveform to the ground. It was the first “smart” sounder, in that the mode of operation was changed when strong plasma resonances were encountered.

From 1977 to 2000, eleven magnetospheric sounders (on the GEOS 1, ISEE 1, GEOS 2, EXOS B, Viking, EXOS D, IMAGE, and four Cluster satellites) from four countries (France, Japan, Sweden, and the US) were placed into orbit. The first was of the relaxation type, i.e., low-power transmissions designed to stimulate local plasma resonances. It operated from the European GEOS 1. Since the intended geostationary orbit was not achieved, most local electron-density (N_e) measurements, as deduced from the sounder-stimulated plasma resonances, were made from radial distances between five and seven Earth radii (R_E). The last four were also relaxation sounders, designated as WHISPER (Waves of HIGH frequency and Sounder for Probing Electron density by Relaxation); an identical sounder was placed on each Cluster satellite. The first magnetospheric sounding (out to a radial distance of nearly $2R_E$) to stimulate the full spectrum of plasma resonances, including a class of resonances known as the Dn resonances that were prominently stimulated in the ionosphere by Alouette 2 and ISIS 1 at radial distances out to about $1.5R_E$, was from the Japanese EXOS D (Akebono). The first long-range magnetospheric sounding (out to a radial distance of $8R_E$), using a programmable instrument with digital signal processing, was performed by the US sounder RPI on the IMAGE satellite. It was capable of low-frequency operation because of 500-m tip-to-tip dipole antennas in the spin plane. As in the case of the ISIS-2 observatory, IMAGE/RPI demonstrated the compatibility of remote imaging from a spinning satellite containing long sounder antennas.

Three extraterrestrial sounders, based on cooperative agreements among the US, France, and Italy, were launched between 1990 and 2003. Two were of the relaxation type: the Unified Radio And Plasma-wave instrument (URAP) on the Ulysses spacecraft to Jupiter (encountering the Io plasma torus in February 1992), and the Radio and Plasma Wave Science (RPWS) investigation on the Cassini spacecraft to Saturn. The Mars Advanced Radar for Subsurface and Ionospheric Sounding (MARSIS) instrument performed the first planetary ionospheric sounding at Mars in June 2005 from the Italian/US Mars Express.

While the above discussion highlights the many firsts associated with space-borne sounders, it is important to note that there was a fundamental first associated with ground-based sounders, commonly referred to as ionosondes. As pointed out by Warren Flock [37],

The ionosonde, developed in 1925-1926 and used for monitoring the ionosphere since, was the first practical

radar system of significance to be put into service. Operating in the HF frequency range and developed some years prior to surveillance radars, before the term radar (for radio detection and ranging) was introduced, the ionosonde may not be thought of by some as a radar, but it clearly is a special-purpose radar system.

Descriptions of the operation of swept-frequency ionosondes, and the interpretations of their data records, called ionograms, have been given in numerous books and publications [38-45]. Modern ionosondes, in use worldwide, incorporate both enhanced remote-sensing capabilities and automatic-analysis techniques [46-51].

The material in Table 1 was based on a comprehensive review of the ISIS program [52], a more-recent review that includes sounders other than those from the ISIS program [53], and information collected by the author with the aid of colleagues. It includes representative references from the various space-borne sounders: see [54] for a thorough review with references covering the first two decades of Alouette-1, Explorer-20, Alouette-2, and Explorer-31 operations. The related discussion in the text is based on the author’s involvement with radio-sounding research using data from sounders carried on the Alouette 1 and 2, ISIS 1 and 2, OEDIPUS C, Ulysses, and IMAGE spacecraft. The objectives, history, and principal achievements of the ISIS program were discussed in a special issue of the *Proceedings of the IEEE* on topside sounding and the ionosphere [55]. There has been a resurgence of interest in the analysis of the Alouette-2, ISIS-1 and ISIS-2 topside sounder data, following a data-rescue effort that produced digital ionograms from a subset of the original analog telemetry tapes – many that were not previously processed into 35-mm film ionograms [56]. OEDIPUS C (Observations of Electric-field Distributions in the Ionospheric Plasma—a Unique Strategy) established a new record length for the longest tether in space at the time (approximately 1.2 km), breaking the record set by its predecessor, OEDIPUS A. The tether was cut shortly after the dual rocket payload achieved apogee, in order to provide the setting for unique bistatic radio-sounding experiments. The addition of an active sounding mode to the URAP instrument on the interplanetary Ulysses probe was the result of leadership by the late R. G. Stone, as PI, after instrument selection. IMAGE/RPI employed the longest antenna elements ever deployed on a spinning spacecraft, namely, orthogonal 500 m tip-to-tip dipoles in the spin plane, and a 20 m tip-to-tip dipole along the spin axis. The former were later shortened (presumably by micrometeorite impacts), but did not prevent successful active soundings (see, e.g., Section 1.2 of [57]).

This paper is not intended to be a thorough review of space-borne radio sounding, as approximately 1,000 scientific papers have been written based on these sounders. Rather, the plan is to discuss space-borne radio sounding as the gold standard for *in-situ* and remote electron-density (N_e) determinations in Section 2. Fundamental plasma

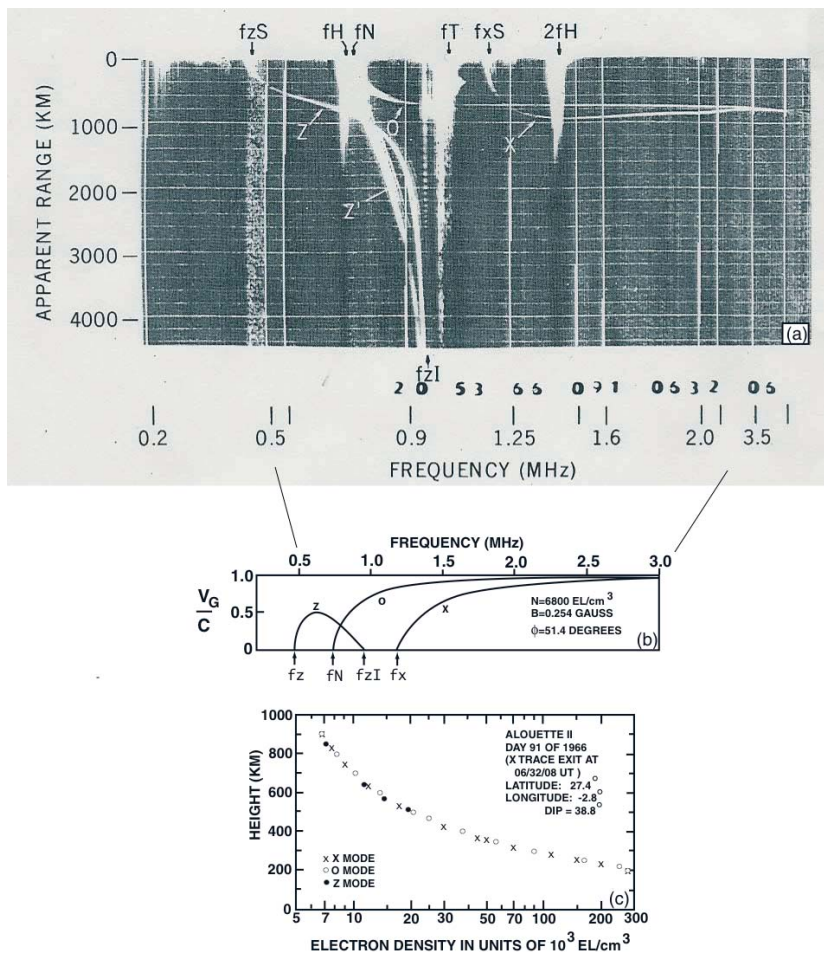


Figure 1. (a) An Alouette-2 mid-latitude ionogram, in negative format with signal reception in white on a black background, showing Z, O and X traces, plasma resonances, and a natural noise band (presumably in the Z mode): see the discussion in the text. (b) The group velocities corresponding to the plasma conditions at the satellite. (c) The calculated N_e values from each of the traces. (Figure adapted from [59, 60].)

processes, and gradients in N_e and the magnetic field, \mathbf{B} , are discussed in Section 3. Enabling instrumental innovations are covered in Section 4. The importance of the antenna's orientation (relative to \mathbf{B}) and of special plasma conditions for sounder-stimulated plasma phenomena are discussed in Sections 5 and 6, respectively. Nearly lossless propagation within N_e wave ducts are covered in Section 7. Section 8 provides a brief summary.

2. Space-Borne Radio Sounding as the Gold Standard for N_e Determinations

The original motivation for placing radio sounders in space was to obtain routine ionospheric N_e information over large geographic regions at altitudes above h_{max} , i.e., in the topside ionosphere: hence, the name ionospheric topside sounders. They are complementary to ground-based ionosondes, in that they provide orbit-plane topside N_e contours over a short time interval above a ground-based station where an ionosonde provided 24-hour coverage of the N_e profile below h_{max} . (Note: In each case, there are problems associated with the determination of h_{max} . Ionosonde measurements from the ground typically yield values that are about 10 km too low, and topside-sounder measurements from a satellite typically yield values that are

about 10 km too high [58].) Since many of these topside-sounder satellites were in high-inclination orbits, the topside orbit-plane N_e contours corresponded to latitudinal contours. With an orbital period of about 90 minutes, these contours can be considered to be snapshots of the topside ionosphere covering about 40° of latitude in 10 minutes.

In addition to the differences in spatial and temporal coverage between ionosondes and topside sounders, there are fundamental differences in the received signals. These signals are recorded on data records called ionograms, which display the apparent range to the reflection point as a function of sounding frequency. The apparent range, also called the virtual range, is defined as $ct/2$, where c is the vacuum speed of light, and t is the roundtrip travel time. The apparent range is greater than the true range because, in the frequency range of main interest, the waves travel with a group velocity, v_g , considerably less than c . An example of a topside ionogram is presented in Figure 1a. The values of v_g for each of the principal ionospheric reflection traces, corresponding to the plasma conditions at the satellite as determined from the resonances and cutoffs (see next paragraph) on the ionogram of Figure 1a, are presented in Figure 1b.

Topside ionograms, such as the one in Figure 1a, differ from ground-based ionograms in that:

1. The apparent ranges of the echoes are much greater (they are typically within 1,000 km on ground-based ionograms [42]).
2. The echo traces extend to zero range (they typically do not appear below 100 km range on ground-based ionograms [42]).
3. The Z-mode wave is directly observed (it is only detected after a coupling to the O-mode wave on ground-based ionograms [39]).
4. Prominent plasma resonances, appearing as stalactites hanging from the zero apparent-range baseline, are present (these signals are mainly attributed to the reception of short-range electrostatic-mode echoes, and thus are not observed by ground-based sounders, where the antenna is in the neutral atmosphere [61]).
5. The ionosphere often generates noise bands that are received over the entire listening range, such as the one with a low-frequency cutoff coinciding with fzS in Figure 1a.
6. The ionosphere provides shielding of manmade interference in the frequency region below the ionospheric penetration frequency, $fxF2$ [62], allowing low powers to be used in topside sounding (a few hundred watts, rather than several kW as used in ground-based sounding in the 1960s), even though the propagation distances are much greater.
7. In the frequency region above $fxF2$, surface reflections are often received that enable information to be deduced about the entire (topside and bottomside) $N_e(h)$ profile [63], as well as terrain information [64]. At Mars, the sounder has been used as a ground-penetrating radar in this frequency region [65].

The labels at the top of the ionograms in Figure 1a use notation common in ionospheric publications. The labels correspond to (with commonly used magnetospheric physics notations in parentheses) the electron cyclotron frequency, f_H (f_{ce}) and harmonics nf_H (nf_{ce}); the electron plasma frequency, f_N (f_{pe}); the upper-hybrid frequency, f_T (f_{uh}); the cutoff frequency of the free-space extraordinary (X) mode, $f_X S$ (the “S” is used to designate the cutoff frequency at the satellite); and the cutoff frequency, $f_Z S$, of the slow branch of the X mode, called the Z mode. The cutoff frequency of the free-space ordinary (O) mode corresponds to f_N . These frequencies have been defined in many books and review articles, e.g., see Sections 2 of the reviews [66] and [67]. They are defined below in terms of how they can be used to determine $|\mathbf{B}|$ and N_e :

$$|\mathbf{B}| \text{ [nT]} \cong 35.7(nf_H \text{ [kHz]})/n, \text{ where } n = 1, 2, 3, \dots \quad (1)$$

$$N_e \text{ [cm}^{-3}\text{]} \cong (f_N \text{ [kHz]})^2 / 80.6, \quad (2)$$

$$f_N = (f_T^2 - f_H^2)^{1/2}, \quad (3)$$

$$f_N = [f_X (f_X - f_H)]^{1/2}, \quad (4)$$

$$f_N = [f_Z (f_Z + f_H)]^{1/2}. \quad (5)$$

Equations (4) and (5) lead to the useful expression

$$f_H = f_X - f_Z. \quad (6)$$

The quantity f_H (and hence $|\mathbf{B}|$ from Equation (1)) can often be determined to an accuracy of a few tenths of a percent, since there are typically more nf_H resonances present on an ionogram than in the example of Figure 1a, and the individual frequencies can typically be determined to an accuracy of a few percent or better (see, e.g., Appendix A of [56]). Once f_H is accurately determined, Equations (3) to (5) provide three independent measurements of f_N (and hence, N_e from Equation (2)), based on the observed values of f_T , f_X , and f_Z . Thus, together with the observed value for the f_N resonance and Equation (2), there are four independent determinations of N_e available from an ionogram such as the one shown in Figure 1a. Even when X and Z traces are not present, other resonances are often present to enable a spectral classification so as to determine N_e values to a precision of $\sim 1\%$, even when $N_e \sim 1 \text{ cm}^{-3}$ (see Section 3, and Section 3 of [68]).

The above redundancy in the determination of f_N , the typical accuracy of a few percent or better in determining the frequencies, and the minimal effect of spacecraft/plasma interactions on the determined values (see Section 3), leads to the concept of the space-borne sounder as the gold standard for the accurate determination of N_e . Indeed, the comparison of different DMEA probe techniques used the nearby Alouette-2 topside-sounder as the N_e reference level [69, 70]. Also, a comparison of data acquired from the DMEA and Alouette-2 cylindrical electrostatic probes indicated “no inherent incompatibility” between sounder and probe operations [71]. More recently, interleaved active and passive Radio Plasma Imager observations were used to confirm that accurate magnetospheric N_e measurements – i.e., within a few percent – can be deduced from the spectral features of the upper-hybrid emission band, which is often present on magnetospheric dynamic spectrograms [72]. On the other hand, in the ionosphere earlier investigations based on comparing passive wave observations and active sounder operations have shown that intense wave emissions seldom correspond to the upper-hybrid band, particularly to emissions at f_T (or f_{uh}) [29, 73]

However, the main objective of an ionospheric topside sounder is not to obtain accurate *in-situ* N_e values, but

to obtain complete vertical N_e profiles, $N_e(h)$, from the satellite altitude down to h_{max} . This information is obtained by inverting the following integral expression for the apparent range as a function of frequency, $P'(f)$, in order to obtain the electron-density distribution as a function of true altitude, i.e., $N_e(h)$:

$$P'(f) = \int n' dh, \quad (7)$$

where $n' = n' \{N_e(h), f, |\mathbf{B}|(h), \phi(h)\}$ is the group refractive index, ϕ is the angle between \mathbf{B} and the direction of propagation, and the integration is from the satellite altitude down to the height of reflection for frequency f . Equation (7) and its solution have been discussed in many texts and papers. The approach commonly used in the ISIS program is that of Jackson [60, 74, 75]. The approach is to partition the total integration path in Equation (7) into a number of laminations equal to the number of points selected on the X-mode reflection trace. The values of $|\mathbf{B}|$ and ϕ at the top of each lamination interval, including the first one starting at the satellite altitude, are obtained from a magnetic-field model. The variation of $|\mathbf{B}|$ within a lamination is based on the inverse cube law.

While the observed nf_H plasma resonances are not used to improve on the model's f_H value, other resonances are used with this model value to obtain a better determination of $f_X S$ in situations when it is difficult to accurately measure (see Section 3 of Appendix B of [74]). In some cases, particularly when N_e at the satellite altitude is very low, this iteration technique fails to converge. A modified iteration method has been shown to converge in such cases [76]. Refinements to true-height inversion techniques have continued (see, e.g., [77, 78]), and programs have been developed for the automatic processing of topside digital ionograms [79-82], which have been recently produced for Alouette 2, ISIS 1, and ISIS 2 [56].

Since the expressions for n' in Equation (7) are different for the O and X modes, and since the X mode has two branches, corresponding to a fast wave (termed the X mode) and a slow wave (termed the Z mode), the three ionospheric reflection traces, i.e., the Z, O, and X traces in Figure 1a, yield three independent ways to determine the $N_e(h)$ profile. The results of applying the inversion analysis to these three reflection traces in Figure 1a are shown in Figure 1c. The good agreement among the calculated $N_e(h)$ profile values based on the observed $P'(f)$ values from the Z, O, and X reflection traces provides confidence that these traces were properly identified, and that the two main assumptions used in the analysis were satisfied, namely, that the propagation was vertical and that the ionosphere was horizontally stratified. Note that the points corresponding to the O and X modes extended all the way down to near h_{max} , i.e., the altitude of maximum N_e near 200 km, whereas the points corresponding to the Z mode extended only down to about 500 km. This limitation was caused by the restriction of the Z mode to frequencies less than $f_Z I$ (called "Z infinity") in Figure 1b. In Figure 1a, $f_Z I$ appears as a narrowband signal just beyond 0.9 MHz hanging from the top of the ionogram, and it coincides with the asymptotic Z trace at the bottom of the ionogram. $f_Z I$ varies between f_N and f_T , depending on the angle of propagation. In spite of this propagation limit for the Z-mode echoes, IMAGE/RPI Z-mode echoes have been used to determine accurate N_e profiles along \mathbf{B} for thousands of kilometers above the IMAGE satellite, i.e., into regions of decreasing N_e , when IMAGE was in the inner plasmasphere and at moderate to low altitudes over the poles [83]. These Z-mode echoes are possible because the Z-mode cutoff frequency, f_Z , in Equation (5) can have a local minimum leading to a trapping region for Z-mode waves [84]. An inversion routine was developed to convert the IMAGE/RPI Z-mode echoes into field-aligned N_e profiles in the vicinity of the spacecraft [83]. It was shown that these profiles were in good agreement with model values based on a different inversion procedure [85] used on IMAGE/RPI X-mode echoes.

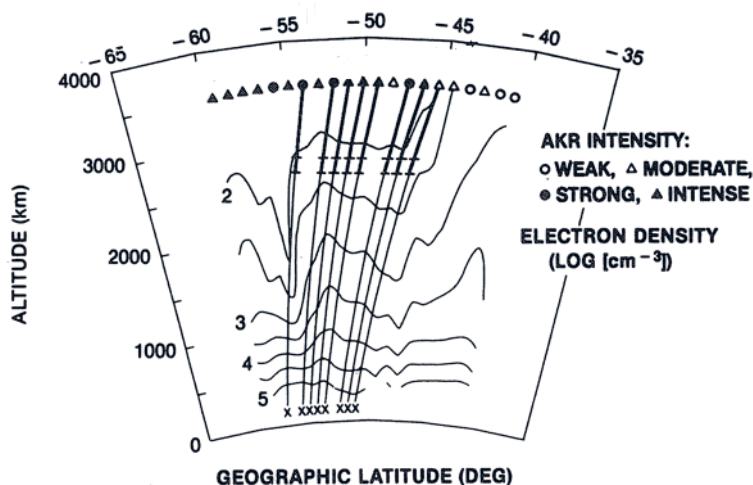


Figure 2. ISIS-1 sounder-derived N_e contours (10^2 , 3×10^2 , 10^3 , etc.) and field-aligned projections through symbols indicating satellite position and auroral kilometric radiation intensity, with upper bold portions indicating the depth beneath the satellite of the auroral kilometric radiation source region (with estimated error limits), as determined from the spectral range of the auroral kilometric radiation (0959-1008 UT on 19 August 1969; adapted from [92]).

In addition to Z-, O-, and X-mode echoes, space-borne sounders have also detected echoes from waves propagating in the whistler (W) mode. Whistler-mode echoes were detected on high-latitude, early-morning Alouette-2 ionograms, and were attributed to ground reflections and a mode-coupling process in the lower ionosphere [86]. IMAGE/RPI commonly observed W- and Z-mode echoes when IMAGE was in the inner plasmasphere and at moderate to low altitudes over the polar regions [87]. Two types of W-mode echoes were observed by the Radio Plasma Imager: discrete and diffuse. The former were attributed to reflections from the bottom side of the ionosphere; the latter were attributed to scattering from field-aligned N_e irregularities (FAI) located within 2,000 km Earthward of the satellite, and near the magnetic field line passing through the satellite. These echoes were consistent with cross-**B** field-aligned irregularity scale sizes ranging from 10 m to 100 km. They support previous evidence [88] for the common occurrence of field-aligned irregularities in the topside ionosphere. Both types of W-mode echoes, and diffuse Z-mode echoes, have great potential for local and remote N_e diagnostics [87].

The results displayed in Figure 1c confirm the validity of the inversion procedure on a given ionogram with good traces. Furthermore, high-latitude conjunction studies between different topside-sounding satellites show good agreement among the $N_e(h)$ (field-aligned) profiles obtained from the different sounders [89]. However, accumulated evidence indicates that the topside Alouette-1 $N_e(h)$ profiles are too low, i.e., that they should be shifted upward parallel to the altitude axis [58]. This evidence included comparing simultaneous Alouette-1 topside profiles, ground-based incoherent scatter radar, and rocket measurements. It indicated that the profiles were about 20 km too low at altitudes below 600 km. Detailed topside-sounder/bottom-side-ionosonde comparisons, involving both Alouette-1 and Alouette-2 profiles, indicated that the topside altitude error was only a few percent of the propagation path. The differences were too large to be attributed to the vertical propagation assumption (rather than performing actual ray tracing). When the propagation path was short, i.e., corresponding to low satellite altitudes, a systematic error was detected in the range markers. An inspection of the ground reflection traces observed on Alouette-2 ionograms indicated that the best $N_e(h)$ profile results were obtained by assuming this systematic error to be 30 km, i.e., by reducing the virtual range by 30 km [58]. This range-marker problem led to the addition of a calibration range marker at 1667 km on the ISIS-2 topside sounder [90]. Later work, involving magnetic-field-aligned conjunction comparisons between low-altitude DE-2 *in-situ* Langmuir-probe measurements and ISIS-1 and -2 topside $N_e(h)$ profiles, indicated that the sounder-derived N_e values agreed with the probe measurements to within 30% near h_{max} on three of four comparisons. The agreement for the fourth comparison, in a region of N_e irregularities, was within 60% [91].

As stated by Jackson [58] concerning the errors discussed above, they “are usually too small to detract significantly from the general usefulness of topside ionograms.” Many investigations have indicated this usefulness of the topside $N_e(h)$ profiles. For example, Alouette-2, ISIS-1, and ISIS-2 topside $N_e(h)$ profiles were used to reveal a tongue of F-region ionization (attributed to anti-sunward drift caused by magnetospheric convection) extending from the dayside across the polar cap during a magnetically-quiet day [89]. Topside ISIS-1 $N_e(h)$ profiles were combined to produce orbit-plane contours that together with simultaneous passive observations of the auroral kilometric radiation (AKR) frequency spectrum by the sounder receiver, determined the altitude extent of the auroral kilometric radiation source region below the satellite [92] (see Figure 2). Such orbit-plane N_e contours were compared with plasmopause magnetic-field lines (determined near the same time period by other satellites) to provide examples where the plasmopause projection occurred near the sharp low-latitude boundary of the nighttime ionospheric N_e main (mid-latitude) trough at high altitudes, but near the N_e minimum at lower altitudes. These contours were derived from ISIS-2 $N_e(h)$ hand-scaled profiles obtained from the National Space Science Data Center (NSSDC) ftp site. They may actually correspond to magnetic-field-aligned profiles, making the stated altitudes on the contours slightly low (see Figure 4 of [93]), but not impacting the conclusions of the study.

Large satellite topside sounding databases have enabled a number of diverse investigations. Alouette-1 and 2 hand-scaled $N_e(h)$ profiles have been used to create global-averaged $N_e(h)$ distributions [94]. Computer-scaled ISIS-2 digital ionograms produced $N_e(h)$ profiles that have been used to improve the International Reference Ionosphere (IRI) [95], and that have been used with IMAGE/RPI high-latitude magnetic-field-aligned magnetospheric N_e profiles to model the topside ionospheric F region and plasmasphere [96]. The International Reference Ionosphere is in particular need of improvement in the high-latitude topside ionosphere, as illustrated in Figure 10b of [56]. Global averaged F-region peak critical frequency (foF2) distributions obtained from the ISS-B topside sounder have been used to evaluate global foF2 models [97]. Regional averaged foF2 and h_{max} distributions obtained from the Intercosmos-19 topside sounder have been used to detect ionospheric signatures of tectonic activity [98], and for event studies, such as identifying ionospheric precursor signatures of large earthquakes, as reviewed in [53]. These are only a few examples of the scientific results that have come from the remote-sensing capabilities of space-borne radio sounders, particularly in the ability to derive topside $N_e(h)$ profiles. More examples can be found in a detailed review [54] of the results from the first two decades of the early satellites in the ISIS program.

The next sections will concentrate on some of the serendipitous scientific results that have resulted from these sounders, i.e., results not directly related to the main objective of obtaining vertical N_e profiles.

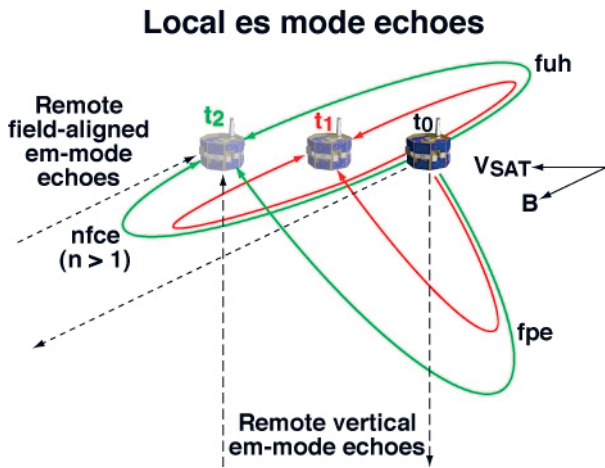


Figure 3. A schematic illustration of ray paths leading to echoes (at times t_1 and t_2) of sounder-generated (at time t_0) electrostatic (solid curves) and electromagnetic (dashed lines) waves [103].

3. Fundamental Plasma Processes, and Gradients in N_e and \mathbf{B}

Spectacular signal returns on topside ionograms can often be explained using ray tracing, and special properties of the refractive index under certain plasma conditions, rather than invoking unusual N_e distributions. A classic example is the observation of a kink in the Z reflection trace that has been explained in terms of the peculiar properties of the Z-mode group refractive index when the wave frequency varies near f_{pe} [99]. Another is the concept of oblique echoes of sounder-generated electrostatic waves, due to the sensitivity of the refractive index to gradients in N_e and \mathbf{B} near f_{pe} , f_{uh} , and nf_{ce} , to explain plasma resonances observed at these frequencies [100-102] (see Figure 3). Since these waves travel hundreds to thousands of meters into the medium, geophysical parameters deduced from the resonant frequencies using Equations (1) to (5) are not significantly affected by spacecraft/plasma interactions.

Note that the ray paths for the nf_{ce} resonances in Figure 3 exclude the case for $n=1$. The parabolic nf_{ce} ray paths illustrated in Figure 3 correspond to electrostatic waves, with wave vectors, \mathbf{k} , nearly perpendicular to \mathbf{B} . The group velocities, \mathbf{V}_g , for these waves are approximately parallel to \mathbf{B} when the wave frequency, f , is near nf_{ce} . Observational and theoretical investigations support the concept illustrated in Figure 3 for the resonances with $n > 1$. Additional effects may play a role in the case of $n = 2$, and the ray paths of the higher-order resonances in the topside ionosphere may be very short (see [104] and references therein). The nf_{ce} resonances stimulated by magnetospheric sounders are observed for much longer time durations [15]. The oblique-echo mechanism has yet to be applied to explain these observations. The nf_{ce} plasma wave dispersion curves with \mathbf{k} approximately perpendicular to \mathbf{B} are quite different for the case $n = 1$, however, and an

interpretation of the observed features of the f_{ce} resonance has been sought for decades. A recent explanation for this resonance involves a solution to the hot-plasma dispersion equation with f near f_{ce} when \mathbf{k} is approximately parallel to \mathbf{B} [105]. It can explain the fringe pattern observed on the f_{ce} resonance during fixed-frequency operations in terms of the beating of two waves radiated from the plane containing the antenna and \mathbf{B} . The waves in this interpretation are highly damped, which may explain the observed strong dependence of the duration of the f_{ce} resonance with altitude (longer duration under low-density conditions at high altitudes) in the Alouette-2 topside-sounder data [106].

There are two prominent sequences of resonances often observed between the nf_{ce} resonances that are not well explained by the oblique-echo mechanism. One is observed in the frequency region above f_{uh} [107], and the other is in the frequency region below f_{pe} [108], following the earlier discovery of the first member of the sequence [109]. The former are known as the Qn resonances, and have been explained in terms of a near matching of slowly-propagating electrostatic waves (known as Bernstein-mode waves) and the satellite velocity, \mathbf{V}_s [110]. The latter are known as the Dn resonances, and have motivated five different theoretical interpretations (see the review in Section 1 of [111]). One proposed that the Dn resonances provided evidence for a new wave mode involving eigenmodes of cylindrical-electromagnetic plasma oscillations [112, 113] based on earlier theoretical predictions, involving force-free electromagnetic field (FFEMF) configurations, and that such oscillations would lead to a quantized emission spectrum with the frequencies of the different elements proportional to \sqrt{n} [114, 115]. The cylindrical structures in this model correspond to the commonly observed field-aligned irregularity observed in space, not to the sheath surrounding the sounder antenna. The wave nature of these cylindrical oscillations was predicted as force-free electromagnetic field waves and solitons [116] that were later observed in a laboratory plasma [117]. The Dn resonances have prominent subsidiary resonances [108] that have been interpreted differently [118-120]. In the magnetosphere, the frequencies of the Qn resonances have been observed to deviate from the values expected for a Maxwellian electron velocity distribution [15, 68, 121, 122]. These observations have been investigated theoretically in two ways: (1) in terms of two Maxwellian components [121]; and (2) as a kappa distribution, where observations were shown to be consistent with a kappa value of two [123]. The Qn resonances also have subsidiary resonances [124, 125]. For a particular n value, the Qn resonance and its subsidiary have been attributed to the Doppler shifts of two waves, one propagating as a forward mode and the other as a backward mode, near but on both sides of the un-shifted Qn frequency [121]. The first member of each sequence is shown in Figure 4 [67]. This also shows one of the D1 subsidiary resonances (D1+); the hybrid relationship proposed to explain it [119]; and a resonance designated as "F" because it is often observed to float from the zero time-delay (or zero apparent range) baseline, and the approximate expression for its frequency [126].

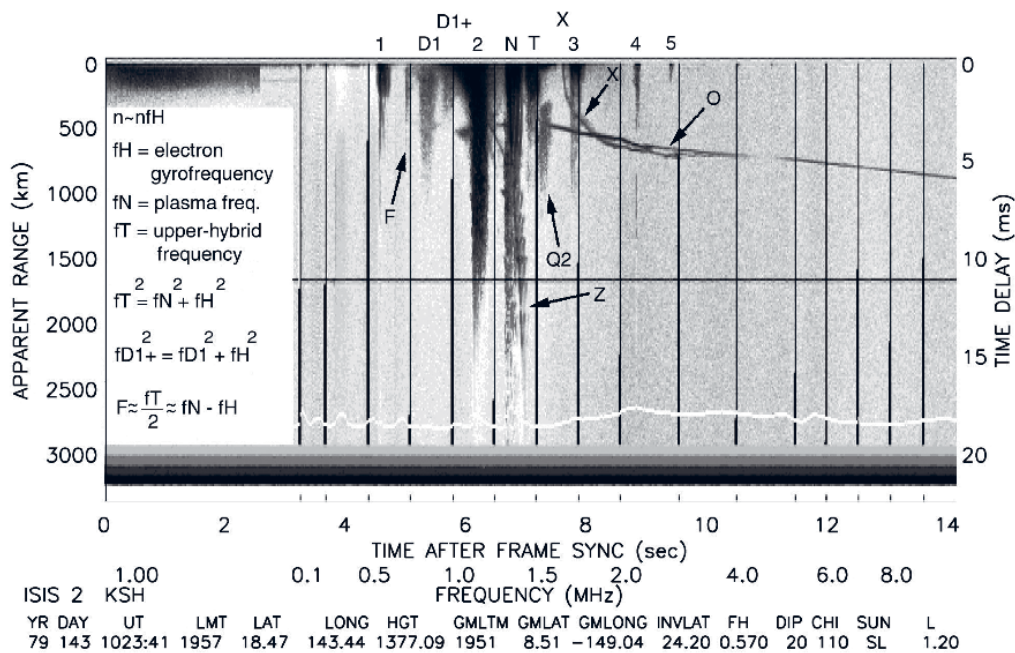


Figure 4. An ISIS-2 digital ionogram illustrating the D1, D1+, Q2, and F resonances (in addition to the resonances that can be explained by the oblique-echo mechanism characterized by Figure 3) [67].

The sequence nature of the Dn and Qn resonances is not apparent from a single ionogram, such as the one reproduced in Figure 4. However, as the plasma parameter, f_{pe}/f_{ce} , increases, higher members of the sequences appear. A presentation displaying the observed resonant frequencies from many ionograms, normalized by the observed f_{ce} versus the observed f_{pe}/f_{ce} illustrates the dominant control of the plasma parameter f_{pe}/f_{ce} in determining the frequency of these resonances [108, 118, 120, 125]. These resonances have proven to be of great value in the spectral classification of sounder-stimulated plasma resonances for the accurate determination of N_e , particularly in the magnetosphere, where clear X and Z traces are often not present [68]. While the Dn-sequence portion of this spectral classification is well explained by the cylindrical-electromagnetic plasma oscillations mechanism, some major issues remain. For example, these issues include deriving the fundamental D1 frequency from first principles (presently it is based on an empirical fit to the observations), and incorporating propagation aspects likely needed to explain the observed long time durations of the Dn resonances and the frequency splitting of the D1 resonance observed at mid latitudes [108, 127]. The issues also include explaining the abrupt disappearance of the $3f_{ce}$ resonance as the D2 resonance becomes prominent [125, 128] (see also Section 6), and investigating the role of sounder-stimulated ion motions leading to ion signatures on Dn resonances [128] (such ion signatures will be discussed in Sections 5 and 6). These issues, plus many other features of the Dn and Qn resonances, such as their excitation by natural process and (in the case of Dn) by rocket-borne electron guns, their use in determining N_e , and their relationship (in the case of Dn) to sounder-accelerated electrons, are discussed in Sections 1 and 3 of [111], Sections 3 of [68] and [113], and the “Discussion and Summary” of [129].

The revolutionary concept of interpreting the plasma resonances as oblique echoes, introduced by McAfee [100] after building on the work of Calvert [130] in interpreting the Z' echo (see, e.g., Figure 1a), was confirmed by innovative rocket experiments, as described in the next section.

4. Instrumental Innovation

Having had the privilege of working with Willi Hough on the ionosphere program, using the massive C3 ionosonde, during the first winter-over operation in 1957 at the Amundsen-Scott IGY South-Pole Station, under the leadership of Paul Siple [131], the author fully appreciates the degree of instrumental innovation involved in placing a swept-frequency ionospheric sounder on a satellite in 1962 [4, 55, 132, 133]. At the time, many thought that the Canadian-built Alouette-1 would at best have the then-typical satellite lifetime of a few months. The pessimism that the sounder would work was so strong that NASA had made no plans to use data from it. However, thanks to a *Robust Design* approach, the sounder provided a wealth of data for 10 years, even surviving higher-than-expected radiation from the unanticipated high-altitude hydrogen-bomb test over Johnston Island in the Pacific Ocean, seven weeks before the Alouette-1 launch [134, 135].

Several rocket payloads in the early 1970s were designed specifically to investigate the plasma resonances detected by ionospheric topside sounders. Rather than retrieving only the received pulse envelope, as in the case of the Alouette and ISIS topside sounders, these rocket-borne sounders telemetered the sounder-receiver waveform to the ground. Fourier analysis of this waveform resulted in unprecedented frequency accuracy. In one experiment,

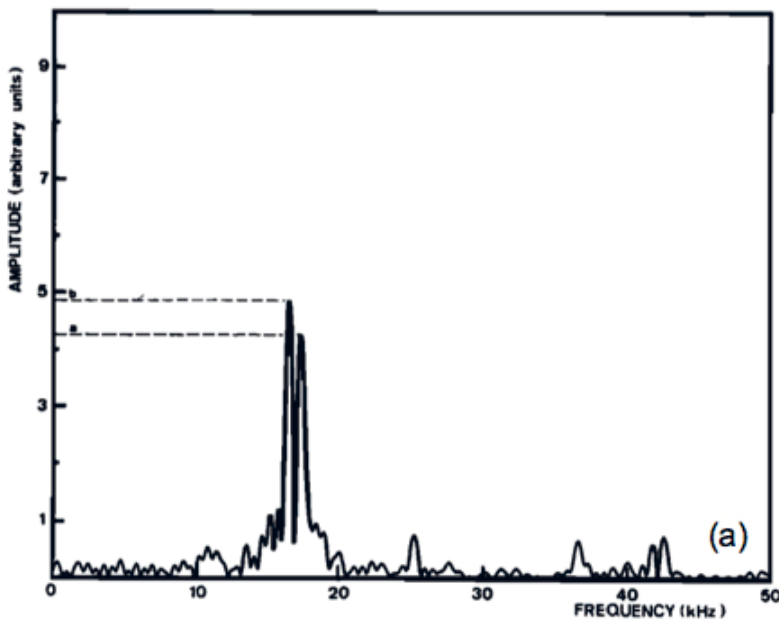


Figure 5a. The Fourier spectrum of the $3f_{ce}$ resonance waveform of the signal observed at 3.096 MHz when the rocket-borne sounder was at 480 km altitude, where $f_{pe} \cong 4.20$ MHz [7].

the $3f_{ce}$ resonance was shown to be the result of a beating of two waves separated in frequency by about 1 kHz, as illustrated in Figure 5a [7]. These remarkable experimental-rocket results suggested that the $3f_{ce}$ resonance was the result of oblique echoes of electrostatic waves, i.e., the $3f_{ce}$ resonance was the result of a mechanism similar to the one proposed earlier for the f_{pe} and f_{uh} resonances [100, 101, 136]. In approximately the same timeframe as this rocket experiment, ray-tracing calculations demonstrated that an Alouette-2 $3f_{ce}$ resonance could be explained by the oblique-echo mechanism [102]. In another rocket experiment, the frequency variation of the received f_{uh} signal with delay time was measured, and found to agree with theoretical predictions based on oblique echoes of slowly propagating sounder-generated waves (see Figure 5b). Previous satellite ionospheric topside sounders could not observe this frequency variation with delay within the receiver bandwidth, because of onboard signal detection [11].

The highly successful bistatic rocket sounders OEDIPUS A and C obtained magnetic-field-aligned separations of the order of 1 km in the auroral topside ionosphere with the sounder transmitter on one payload and the sounder receiver on the other. OEDIPUS-C provided the first *in-situ* demonstration of Faraday rotation in space [30]. It also provided one of the first controlled quantitative confirmations of incoherent radiation theory in space, by detecting slow Z-mode radiation from sounder-accelerated electrons [137]. The OEDIPUS-C measurements of field-aligned irregularities, responsible for wave ducting of sounder generated X- and Z-mode waves, showed they consisted of N_e depletions of up to 21% with dimensions across \mathbf{B} of a few kilometers [138].

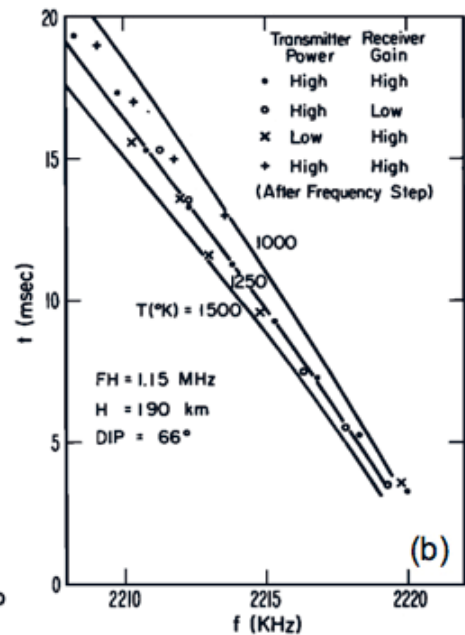


Figure 5b. The echo delay as a function of frequency for the f_{uh} resonance when f_{uh} was slightly less than $2f_{ce}$. The different symbols indicate different combinations of transmitter power and receiver gain during different modes of operation triggered by the large amplitude of the f_{uh} resonance, and the solid lines are theoretical predictions based on different electron temperatures [11].

The above rocket experiments introduced innovations in sounder design that made use of high data rates on short-duration missions dedicated to radio sounding. The design considerations for the sounder known as the Radio Plasma Imager (RPI) for the magnetospheric IMAGE satellite were quite different. IMAGE was a remote-sensing observatory with many instruments, and was far from being a dedicated sounding mission. The Radio Plasma Imager had to overcome programmatic challenges as well as instrumental challenges [139]. The instrumental challenges were many. Sounding was to be performed over great distances involving reflections from low-density plasmas, in spite of power, weight, and data-rate restrictions [66, 140]. The solution was to use 500 m tip-to-tip dipole antennas, transmit coded pulses that enabled signal processing to increase the signal-to-noise ratio so as to obtain long-range echoes with only 10 W radiated power, and to have a variety of programs and schedules to optimize the science return within the data restrictions [33]. The scientific results have been profound, as illustrated in a number of Radio Plasma Imager review papers [34, 141-143], reviews based on IMAGE/RPI and Cluster/WHISPER [144-147], and in other sections of this review.

Similarly, the design considerations for the WHISPER relaxation sounders on the magnetospheric Cluster satellites were also quite different. Here, the challenge was to deliver simultaneous N_e measurements on board the four spacecraft of the constellation in order to calculate instantaneous N_e spatial gradient vectors. The variability of plasma conditions near boundaries demanded a duration of each N_e

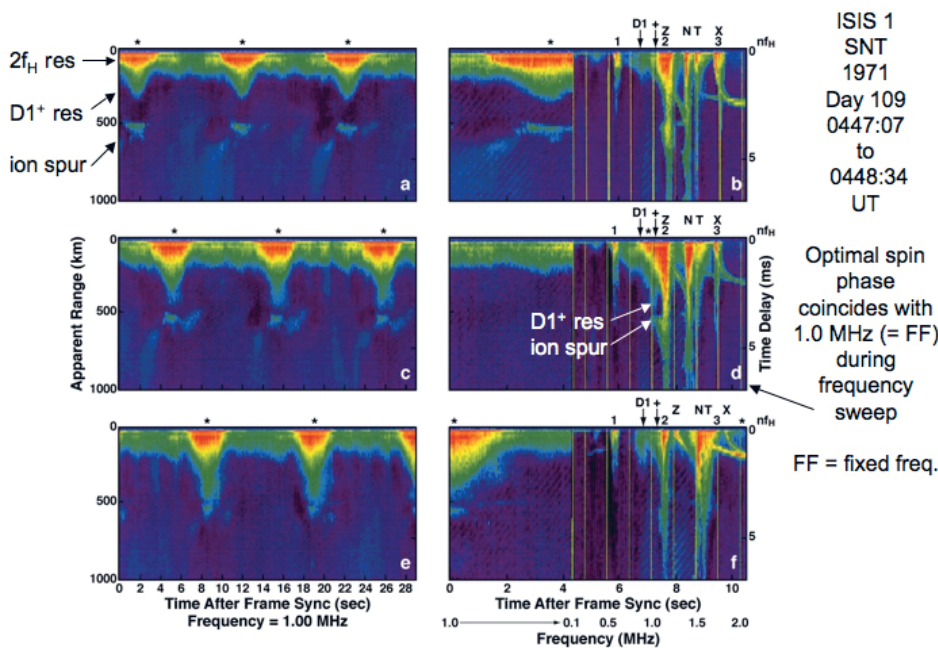


Figure 6. Six consecutive ISIS-1 ionograms when the sounder was operating in the G mode (alternating between fixed-frequency and normal fixed/swept-frequency ionograms), illustrating the antenna spin modulation of the $D1^+$ resonance, the $2f_H$ resonance, and its ion spur. The optimal spin phase for resonance excitation, the calculated value for the $D1$ resonance, and the calculated value for the $D1^+$ resonance are designated at the top of each ionogram by *, $D1$, and +, respectively.

determination significantly shorter than had been obtained on board previous magnetospheric sounders, like GEOS or ISEE. This requirement was met by implementing a fast Fourier transform, instead of a swept-frequency analyzer, in the receiver and analysis chain. The time resolution thus obtained (~ 1.5 s) allowed quasi-synchronization of the four independent measurements, via on-board UT clocks [35, 122, 148, 149].

5. Sounder-Stimulated Plasma Resonances: Importance of the Antenna's Orientation

There are several factors that can determine the occurrence of, and the characteristics of, sounder-stimulated plasma resonances, as have been discussed in a number of review papers [61, 102, 103, 150, 151]. Lockwood [152] was the first to show the importance of the antenna's orientation on the sounder excitation of plasma resonances. He showed that nf_{ce} resonances with high n were only observed by the Alouette-1 topside sounder when the relevant sounder antenna was nearly parallel to B. The relevant antenna was the one being used for transmission and reception. (In order to cover the wide frequency range, Alouette-1 employed crossed orthogonal dipoles of different lengths in the spin plane, with the longer dipole being used for transmission and reception at the lower frequencies, and the shorter dipole used for transmission and reception at the higher frequencies. The Alouette-2, ISIS-1, and ISIS-2 sounders operated in a similar manner [4].) While the effective radiated power does not appear to be a significant factor in determining the duration of the nf_{ce} resonances, as indicated by a comparison of selected Alouette-1 and Alouette-2 observations (see Section 5 of [106]), plasma

conditions do play an important role. The following three studies indicated that for large f_{pe}/f_{ce} , plasma conditions may be the dominant factor:

1. An investigation of the time durations of Alouette-2 nf_{ce} resonances as a function of altitude near the dip equator found the greatest durations for resonances with $n > 5$ in the relatively dense plasma near perigee (see Figures 1 and 8b of [106]), where large values of f_{pe}/f_{ce} are expected.
2. An inspection of more than 200 Alouette-2 ionograms, selected so as to provide a wide range of f_{pe}/f_{ce} values within a narrow range of f_{ce} values, found few high-order nf_{ce} resonances excited when $f_{pe}/f_{ce} < 4$, but found the number of high-order harmonics to increase linearly with increasing f_{pe}/f_{ce} (see Figures 2, 21, and 22 of [125]).
3. A display of ionograms from two ISIS-1 passes, selected to obtain a range of f_{pe}/f_{ce} values from approximately one to 10, again while maintaining a narrow range of f_{ce} values, revealed a striking decrease in the duration and frequency width of the nf_{ce} resonances when $nf_{ce} > f_{uh}/f_{ce}$ (most apparent for $n > 2$). The greatest nf_{ce} resonant duration corresponded to the resonance with frequency closest to, but less than, f_{pe} [153]. Thus, these studies suggested that a particular antenna orientation is not required for the excitation of high-order nf_{ce} resonances when f_{pe}/f_{ce} is large (> 4). These results were consistent with the antenna-orientation restrictions for the detection of high-order nf_{ce} resonances found by Lockwood [152], since the Alouette-1 data set he used only sampled f_{pe}/f_{ce} values less than about four [125].

The sounder's antenna orientation plays an important role in determining the characteristics of the lower-order nf_{ce} resonances, but that role appears to be more complex than in the case of the high-order nf_{ce} resonances when f_{pe}/f_{ce} is small (< 4). An investigation of Explorer 20 fixed-frequency observations indicated that the $3f_{ce}$ resonance revealed a peak in duration with a pronounced fringe pattern when the antenna was perpendicular to \mathbf{B} , but even stronger and longer-duration signals (without fringes) when it was parallel to \mathbf{B} (see Figure 1b of [6]). The striking fringe pattern observed when the antenna was perpendicular to \mathbf{B} is suggestive of two waves beating together, as observed for the $3f_{ce}$ resonance in a rocket experiment [7] as the antenna orientation relative to \mathbf{B} varied approximately $\pm 20^\circ$ around the perpendicular direction. The rocket observations were explained in terms of oblique echoes using analytic ray tracing [154]. This analytic ray-tracing approach was applied to Alouette-1 low-order nf_{ce} resonance observations, where it was found that near the magnetic equator, the maximum resonant duration would be expected when the antenna was nearly perpendicular to \mathbf{B} (see Equation 31 of [104]). Low-latitude Alouette-1 observations indicated that strong plasma resonances at f_{pe} , f_{uh} , $2f_{ce}$, and $3f_{ce}$ could be observed using the long antenna when it was far from parallel to \mathbf{B} , since high-order nf_{ce} resonances were observed a few seconds later on the short antenna [155] (an assumption supported by the plasma conditions, which corresponded to $f_{pe}/f_{ce} < 4$). ISIS-1 fixed-frequency observations of the f_{pe} resonance revealed strong maxima when the antenna was nearly perpendicular to \mathbf{B} that were separated by a deep minimum when it was perpendicular to \mathbf{B} . These observations have been explained by including the finite size of the antenna in the oblique-echo interpretation [156]. In general, it appears that plasma resonances at f_{pe} , f_{uh} , $2f_{ce}$, and $3f_{ce}$ can be stimulated over a wide range of antenna orientations. However, the signal strengths, time durations, and fringe patterns change in spectacular ways when the angle between the antenna and \mathbf{B} is near either 0° or 90° .

Figure 6 presents six consecutive ISIS-1 ionograms, illustrating the enhancement of the $2f_{ce}$ resonance (the notation $2f_H$ is used in the figure) when the sounder antenna was in an optimal orientation. During this sequence, the ISIS-1 topside sounder alternated between fixed-frequency ionograms (Figures 6a, 6c, and 6e) and normal fixed/swept-frequency ionograms (expanded portions shown in Figures 6b, 6d, and 6f). From the later ionograms, it was clear that $f_{pe}/f_{ce} < 3$, and that the $2f_{ce}$ resonant frequency was significantly greater than 1.0 MHz, the frequency corresponding to the fixed-frequency operations. Note that even though the $2f_{ce}$ resonant frequency was greater than 1.0 MHz, the $2f_{ce}$ resonance was observed on the fixed-frequency ionograms (Figures 6a, 6c, and 6e) for a short duration with an intense (red) signal every time the sounder antenna was in an optimum orientation (these orientations are indicated by the * marks at the top of the ionograms). These short-duration intense signals resulted from a broadening of the bandwidth of the $2f_{ce}$

resonance during these favorable antenna orientations. (These signals shifted in phase from one fixed-frequency ionogram to the next fixed-frequency ionogram because the time interval between these ionograms was near but not an exact multiple of the antenna-spin period, the former being 57.9 s and the latter being about 20 s.) This broadening (to include 1.0 MHz) was seen on only one of the normal fixed/swept-frequency ionograms, namely, Figure 6d, the only ionogram where the sounder antenna was in an optimal orientation as the swept frequency was near 1.0 MHz (as indicated by the * in Figure 6d). In addition to the larger bandwidth, the intense (red) portion of the $2f_{ce}$ resonance was observed to have a longer duration on this ionogram than on Figures 6b and 6d. These characteristics suggested that the optimal antenna orientations, flagged by the * marks, corresponded to the antenna being nearly parallel to \mathbf{B} , based on the Explorer-20 fixed-frequency observations where the strongest nf_{ce} resonances with no fringe patterns were observed under these conditions [6, 150].

There were two other striking features to notice in the expanded portion of the fixed/swept-frequency ionogram shown in Figure 6d, where this optimal antenna orientation occurred when the swept frequency was near 1.0 MHz. First, the $2f_{ce}$ resonance had an ion spur near 500 km apparent range that extended far enough on the low-frequency side of the resonance so as to reach the 1.0 MHz frequency marker. Second, there was a long-duration D1+ resonance near 1.0 MHz extending to nearly 500 km apparent range. Both of these features were only apparent on the fixed-frequency ionograms (Figures 6a, 6c, and 6e) under the * marks, indicating optimal antenna orientation, and they were less pronounced during the swept-frequency operation on Figures 6b and 6f, where the optimal antenna orientation (* marks) did not occur near the excitation of the $2f_{ce}$ resonance or the calculated positions of the D1+ resonances (indicated by the arrows below the + signs near 1.0 MHz). No theoretical explanation has been proposed to explain this dependence of the D1+ resonance stimulation on the antenna's orientation. However, this dependence was likely the reason the subsidiary Dn resonances were not always present with their corresponding main resonance on the same ionogram. The example in Figure 4, where the D1 and D1+ resonances were clearly seen on the same ionogram, is not typical.

The ion spur illustrated in Figure 6 (also known as a proton spur, because it appears after a time delay equal to the proton gyro period) clearly demonstrated that positive ion motions cannot be ignored if such sounder-stimulated phenomena are to be explained. These spurs were also apparent in the ionogram of Figure 4 near 500 and 1,000 km apparent range on the f_{pe} resonance (labeled "N"), and on the $2f_{ce}$ resonance (labeled "2"), where the spur extended nearly to the 1.0 MHz frequency marker at an apparent range slightly below the 500 km apparent-range label. Evidence for sounder-stimulated ion motions was first identified as a series of spurs on the sounder-generated plasma resonances on Alouette-1 topside ionograms [157]. These spurs have been

the subject of additional investigations using later topside sounders with better frequency resolution that identified specific resonances containing ion spurs [128, 158, 159]. Their explanation may be similar to the interpretation of the proton-cyclotron echoes observed on topside ionograms. These interpretations involve either proton bunching due to the RF-pulse-induced negative sounder-antenna potential [160, 161], or selective proton acceleration by the RF sounder pulse depending on the RF phase [162, 163]. Recent IMAGE/RPI observations at various altitudes within the plasmasphere have revealed intense W-mode proton-cyclotron echoes that were attributed to proton excitation as a transient event near the beginning of each RF sounder pulse. They were believed to be the most efficient at frequencies near and below the proton plasma frequency [57]. These Radio Plasma Imager observations also revealed two other forms of proton-cyclotron echoes that were similar to echoes observed by the Alouette/ISIS topside sounders. The first of these involved striking echoes

at frequencies just above f_{ce} with a delay-time dependence on sounder frequency, suggesting warm-plasma propagation following a sounder-perturbed proton distribution possibly similar to that proposed for the ISIS observations [162]. The second involved proton-cyclotron echoes associated with the cold-plasma Z mode [57].

6. Sounder-Stimulated Plasma Resonances: Importance of Special Plasma Conditions

Sounder-stimulated plasma phenomena have been observed to be particularly sensitive to the value of the plasma parameter f_{pe}/f_{ce} . There was a stepping through higher members of the Dn resonances as f_{pe}/f_{ce} increases [108, 118, 125]; an instability signature on the nf_{ce} resonances when $nf_{ce} < f_{uh}$ [153]; an enhancement of the proton spurs when $nf_{ce} \approx f_{pe}$ [128]; a strong diffuse resonance between f_{pe} and f_{uh} (known as DNT) that changed from a floating to a non-floating resonance as the plasma conditions changed from $f_{pe}/f_{ce} < 1$ to $f_{pe}/f_{ce} > 1$ [125]; an abrupt disappearance of the $3f_{ce}$ resonance when $f_{pe}/f_{ce} \approx 4$ (see Figure 9 of [128] and Figure 14 of [125]); and enhanced scattering of sounder-generated Z-mode waves when $f_{pe}/f_{ce} \approx n$ and $n \geq 4$, suggesting either sounder-enhanced or sounder-generated field-aligned irregularity [164]. Figure 7b illustrates this last phenomenon. Here, enhanced proton spurs and Z-mode scattered signals were observed when $f_{pe}/f_{ce} \approx 6$. During the three-ionogram sequence of Figure 7, f_{ce} decreased slightly from Figure 7a to 7c, and thus the frequencies of the nf_{ce} resonances varied only slightly from one ionogram to the next. Some of the more-prominent nf_{ce} resonances in Figure 7c are labeled at the top of the ionogram. However, the f_{pe} and f_{uh} resonances (coalescing into the long-duration signal between the Z and X reflection traces) increased considerably in frequency from one ionogram to the next. Only in Figure 7b, where the indicated signal enhancements were observed, was the ratio f_{pe}/f_{ce} near an integer value.

It has been shown that the enhanced signals attributed to wave scattering in Figure 7b were not due to more-efficient scattering when $f_{pe}/f_{ce} \approx n$ [165]. This result supports the argument that the wave scattering is from field-aligned irregularity stimulated, or enhanced, on a short time scale by the sounder [164]. These observations stimulated two theoretical studies:

1. An investigation of large-amplitude electron oscillations in cylindrical plasma structures aligned along \mathbf{B} , i.e., with structures that could represent field-aligned irregularity, where enhanced resonance conditions were found when $f_{pe}/f_{ce} \approx n$ and where it was suggested that future work include dissipation and driver mechanisms [166].

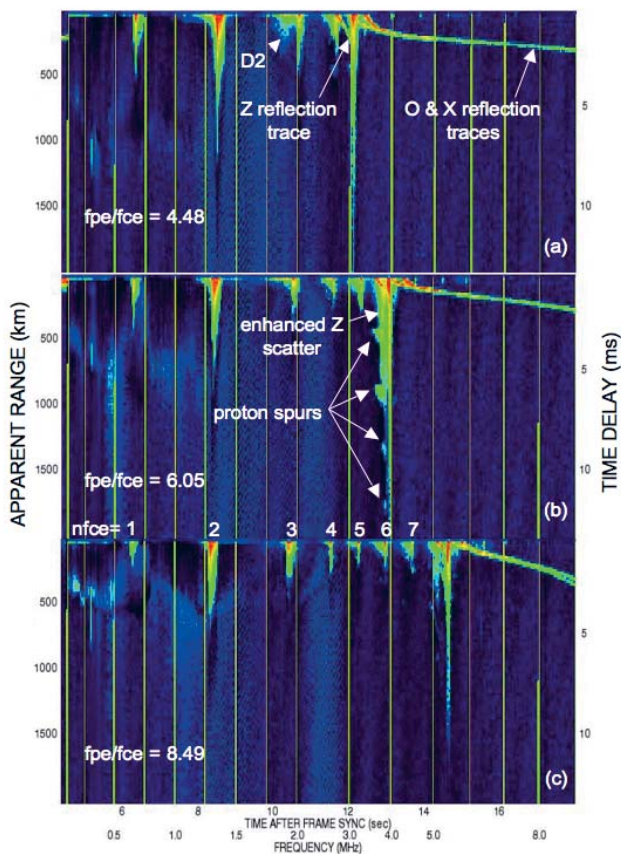


Figure 7. Portions of three consecutive ISIS-1 ionograms illustrating the changes in sounder-stimulated plasma phenomena as the ambient plasma conditions changed from $f_{pe}/f_{ce} < 5$ in (a) to $f_{pe}/f_{ce} > 8$ in (c). Spectacular enhancements occurred when $f_{pe}/f_{ce} \approx 6$ near 13 s after the frame sync, corresponding to a swept-frequency value of about 4.0 MHz in (b). (Recorded at QUI on 1971_006 with ISIS-1 at -11.9 GMLONG and 1914 GMLTM; 0037:36, 0038:06, and 0038:05 UT, 13.4, 11.5, 9.6 GMLAT, 704.5, 688.1, 673.3 km, in (a), (b), and (c), respectively; scaled f_{pe}/f_{ce} values: 3.03/0.676, 3.97/0.656, and 5.45/0.642 in (a), (b), and (c), respectively.)

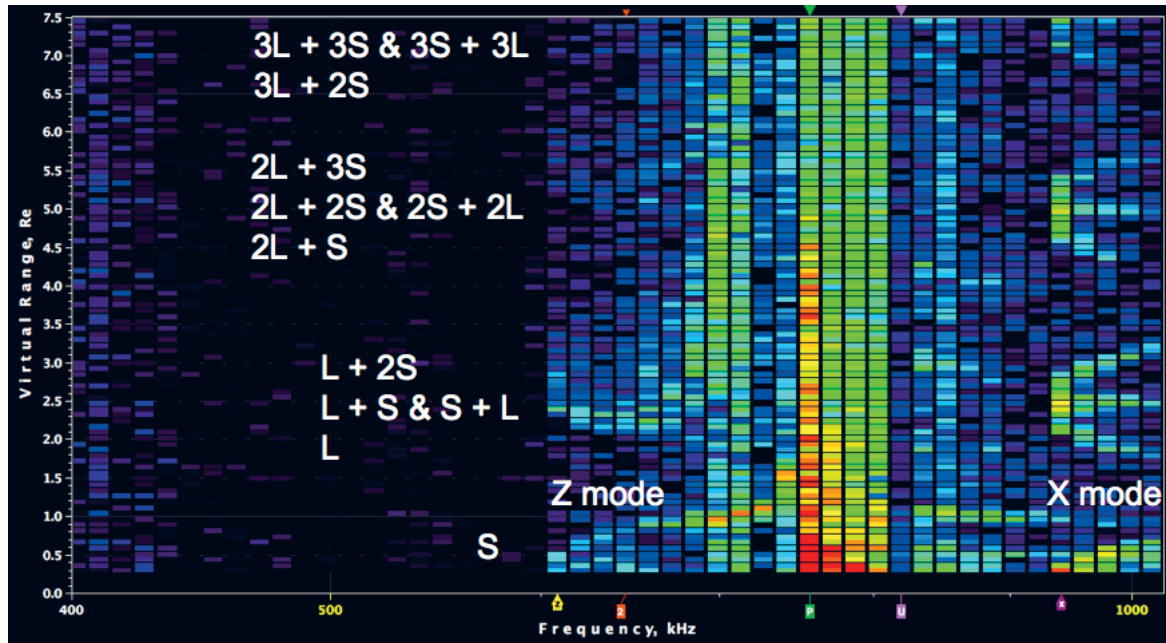


Figure 8. An IMAGE/RPI plasmagram (color-coded signal amplitude, with red most intense, displayed as virtual range from 0 to $7.5R_E$ on a linear scale as a function of sounding frequency from 400 to 1000 kHz on a logarithmic scale) with multiple Z- and X-mode epsilons, each containing traces due to multiple-hop hemisphere-to-hemisphere echoes. Echoes within the local hemisphere, i.e., the hemisphere containing the IMAGE satellite, are labeled “S” for short echo path, and echoes from the conjugate hemisphere are labeled “L” for long echo path. The outside labels on the bottom scale designate the Z- and X-mode cutoffs. The inner three labels on the bottom scale, and the three arrows at the top, identify the model value for $2f_{ce}$ and the calculated f_{pe} and f_{uh} values consistent with the observed wave cutoffs. (1850:28 UT on 31 August 2002; 11.1 MLAT, 0228 MLT, $1.5R_E$, $L = 1.57$.)

2. A four-wave coupling process, where a sounder-generated Z-mode wave acts as a pump wave at frequency f_O , which decays into two electron Bernstein waves and a purely growing meter-scale field-aligned irregularity when this Z-mode wave propagates to the O-mode reflection layer, where $f_O \approx f_{pe} \approx nf_{ce}$ [167]. In this latter study, the $f_{pe} \approx nf_{ce}$ condition would thus be achieved at some distance from the satellite, rather than at the satellite’s location as observed.

A new resonance, stimulated by the Radio Plasma Imager on the IMAGE satellite, has been observed at a frequency about 15% above f_{ce} when the spacecraft is within the plasmasphere but at altitudes above about 7,000 km [57]. It was suggested that the lack of observation of this resonance by the Alouette-2 and ISIS-1 topside sounders may have been due to their relatively low apogees of 3,000 and 3,500 km, respectively [57]. Recall that in Section 3, it was pointed out that there is both theoretical and observational evidence that the f_{ce} resonance itself is also expected to be observed in a stronger form in a rare rather than a dense plasma.

The plasma conditions encountered by the URAP relaxation sounder on Ulysses in Jupiter’s Io plasma torus led to a spectrum of sounder-stimulated plasma resonances quite different from those encountered in the Earth’s ionosphere or magnetosphere. The resonances were first interpreted in terms of the Dn resonances and the f_{pe} resonance, with no evidence for resonances at nf_{ce} or f_{uh} , to deduce both $|\mathbf{B}|$

and N_e along the spacecraft (s/c) trajectory [27, 168]. Later, they were interpreted as Doppler-shifted nf_{ce} resonances, due to the large (> 100 km/s) spacecraft velocity relative to the co-rotating Jovian magnetospheric plasma, and were used to deduce both N_e and T_e along the spacecraft’s trajectory [28]. These different interpretations generated some controversy [169-171].

7. Nearly Lossless Propagation within N_e Wave Ducts

The first satellite evidence of efficient propagation within N_e wave ducts was in the classic paper by Muldrew [172], published one year after the Alouette-1 launch. There have been many investigations of this non-vertical propagation [86] that include the concept of ducting within field-aligned irregularity in the whistler (W), Z, O, or X modes [83, 87, 173-176]. These ducted signals can take the shape of spectacular signals appearing as floating epsilons on ionospheric topside ionograms [177, 178] and on magnetospheric plasmagrams [83, 176, 179], as illustrated in Figure 8.

The intensities of the epsilon signatures, which are caused by multiple hemisphere-to-hemisphere echoes, suggest nearly lossless propagation within wave ducts. Such propagation has been well described for the W mode, as well as for the other modes (see, e.g., [173, 174]). Conjugate O-mode epsilons are not apparent in this figure, but when

they are observed, they provide an independent confirmation of field-aligned N_e profiles deduced from Radio Plasma Imager plasmagrams. This confirmation has indicated that what appears as an O-mode magnetospheric conjugate echo is the result of O-Z-O-wave-mode coupling [179], rather than direct O-mode ducting as proposed to explain the Alouette-1 conjugate echoes observed in the ionosphere [172]. The subject of O-Z mode coupling is also of great interest in ground-based wave-injection experiments (see, e.g., [180, 181]).

It is to be emphasized that the combination of echoes from the conjugate hemisphere with echoes from the local hemisphere enabled nearly instantaneous magnetic-field-aligned N_e profiles to be produced from one hemisphere to the other (with only the low-density region near the equator, where N_e is less than the value at the IMAGE satellite, being filled in by interpolation). As IMAGE travels along its orbit, consecutive hemisphere-to-hemisphere field-aligned profiles can be obtained for different radial distances, i.e., different L values. Such consecutive Radio Plasma Imager field-aligned N_e profiles have been combined to produce orbit-plane plasmaspheric N_e contours for a number of IMAGE orbits before, during, and after the large magnetic storm of March 31, 2001, in order to describe the plasmaspheric mass loss and refilling processes [182].

8. Summary

Space-borne radio sounding is a highly reliable technique, compatible with other instruments, for accurately measuring the local $|\mathbf{B}|$, and both local and remote N_e . Sounder observations have provided a wealth of information on the terrestrial topside ionosphere and magnetosphere, and on basic processes of wave generation and propagation. In spite of these great achievements – which have also been obtained in extraterrestrial plasmas – additional improvements to the International Reference Ionosphere for the topside ionosphere are required to meet the needs of present-day technological systems. Fundamental questions, such as the following, remain to be answered concerning many sounder-stimulated plasma phenomena:

1. What processes, in addition to the oblique-echo model, are needed to explain satellite observations of the $2f_{ce}$ resonances?
2. What is the cause of the abrupt disappearance of the $3f_{ce}$ resonance when $f_{pe}/f_{ce} \approx 4$?
3. Can the oblique-echo model explain the long durations observed for the magnetospheric nf_{ce} resonances?
4. What is the origin of the plasmaspheric resonance observed about 15% higher in frequency than f_{ce} , and the proton-cyclotron echoes observed both in a similar frequency region and near f_Z ?
5. Will mechanisms applied to ionospheric and magnetospheric proton echoes be able to explain the proton spurs observed on sounder-stimulated plasma resonances, including their dependence on f_{pe}/f_{ce} and antenna orientation?

6. Can the fundamental D1 frequency be derived from first principles, can propagation aspects be incorporated into the cylindrical-electromagnetic plasma oscillations mechanism so as to explain the observed durations of the Dn resonances, and can the antenna spin-modulation dependence of the subsidiary Dn resonances be explained?
7. What causes the strong DNT resonance observed between f_{pe} and f_{uh} when f_{pe}/f_{ce} is near but less than one?
8. How does a space-borne sounder enhance, or generate, field-aligned irregularity when $f_{pe}/f_{ce} \approx n$ and $n \geq 4$?

9. Acknowledgements

The ISIS-1 ionograms in Figures 6 and 7 were located and retrieved using the NASA Goddard Space Flight Center (GSFC) Space Physics Data Facility (SPDF) CDAWeb service, available from the ISIS data-restoration project home page at <http://nssdc.gsfc.nasa.gov/space/isis/isis-status.html>. The Radio Plasma Imager plasmagram of Figure 8 was produced using the *BinBrowser* software, made available by the University of Massachusetts Lowell group under the leadership of B. W. Reinisch (see the IMAGE home page at <http://image.gsfc.nasa.gov>). Valuable comments and suggestions were received from D. L. Carpenter, I. A. Galkin, D. B. Muldrew, S. A. Pulinets, V. S. Sonwalkar, and two reviewers. Support for this work was provided in part by the NASA Living-With-a Star and Geospace programs and the GSFC Internal Research and Development (IRAD) program.

The Commission H Editor thanks the reviewers Pierrette Decreau and Gordon James for their assistance in evaluating this paper.

10. References

1. A. R. Molozzi and J. R. Richardson, "Measured Impedance of a Dipole Antenna in the Ionosphere," *Space Res.*, **7**, 1967, pp. 489-505.
2. R. W. Knecht, T. E. V. Zandt, and S. Russell, "First Pulsed Radio Soundings of the Topside of the Ionosphere," *J. Geophys. Res.*, **66**, 1961, pp. 3078-3081.
3. R. W. Knecht and S. Russell, "Pulsed Radio Sounding of the Topside of the Ionosphere in the Presence of Spread F," *J. Geophys. Res.*, **67**, 1962, pp. 1178-1182.
4. C. A. Franklin and M. A. Maclean, "The Design of Swept-Frequency Topside Sounders," *Proc. IEEE*, **57**, 1969, pp. 897-929.
5. S. Russell and F. C. Zimmer, "Development of the Fixed-Frequency Topside-Sounder Satellite," *Proc. IEEE*, **57**, 1969, pp. 876-881.
6. W. Calvert and T. E. VanZandt, "Fixed-Frequency Observations of Plasma Resonances in the Topside Ionosphere," *J. Geophys. Res.*, **71**, 1966, pp. 1799-1813.

7. B. Higel, J. Bitoun, and M. Petit, "Rocket Observations of Two Waves Beating at 3fH Resonance," *J. Geophys. Res.*, **77**, 1972, pp. 6254-6258.
8. B. Higel and H. d. Feraudy, "Experimental and Theoretical First Approach to fH Plasma Resonance from a Relaxation Sounding Rocket Experiment," *Radio Sci.*, **12**, 1977, pp. 879-889.
9. G. V. Vasiliev, A. I. Galkin, V. E. Zasenkov, A. S. Kasimanov, Y. V. Kushnerevski, et al., "Experiment on Pulse Radio Sounding of the Ionosphere above the Main Maximum of Ionization," Proceedings of the 10th All-Union Conference on Radiowave Propagation, Irkutsk, 26-30 July 1972, Moscow, Nauka, 1972, pp. 55-58 (in Russian).
10. G. V. Vasiliev, V. E. Zasenkov, A. S. Kasimanov, S. M. Matyushonok, N. S. Mozerov, et al., "Satellite Ionosonde IS-2," Proceedings of the 10th All-Union Conference on Radiowave Propagation, Irkutsk, 26-30 July 1972, Moscow, Nauka, 1972, pp. 59-61 (in Russian).
11. J. R. McAfee, T. L. Thompson, W. Calvert, and J. M. Warnock, "Rocket Observations of Topside Resonances," *J. Geophys. Res.*, **77**, 28, 1972, pp. 5542-5550.
12. K. Folkestad and J. Troim, "A Resonance Phenomenon Observed in a Swept Frequency Experiment on a Mother-Daughter Ionospheric Rocket," *J. Atmos. Terr. Phys.*, **36**, 1974, pp. 667-685.
13. K. Folkestad, J. Troim, and J. Bording, "Interpretation of Signals Detected on a Mother-Daughter Rocket in the Polar F-Region," *J. Atmos. Terr. Phys.*, **38**, 1976, pp. 335-350.
14. B. Higel, "Small-Scale Irregularities of Electron Density in the F Region from f_N Resonances Observed by a Rocket-Borne Relaxation Sounding Experiment," *Radio Sci.*, **13**, 1978, pp. 901-916.
15. J. Etcheto and J. J. Bloch, "Plasma Density Measurements from the GEOS-1 Relaxation Sounder," *Space Science Reviews*, **22**, 1978, pp. 597-610.
16. C. C. Harvey, J. Etcheto, Y. D. Javel, R. Manning, and M. Petit, "The ISEE Electron Density Experiment," *IEEE Trans. Geosci. Electr.*, **GE-16**, 3, 1978, pp. 231-238.
17. T. Maruyama and N. Matuura, "Global Distribution of Occurrence Probability of Spread Echoes Based on ISS-B Observation," *J. Radio Res. Lab.*, **27**, 1980, pp. 201-216.
18. B. Higel and L. Wu, "Electron Density and Plasmopause Characteristics at 6.6 RE: A Statistical Study of the GEOS 2 Relaxation Sounder Data," *J. Geophys. Res.*, **89**, A3, 1984, pp. 1583-1601.
19. T. Ono and H. Oya, "Electrostatic Electron Cyclotron Harmonic (ESCH) Echoes Found near the Plasmopause by the EXOS-B (Jikiken) Satellite," *Geophys. Res. Lett.*, **15**, 1988, pp. 156-159.
20. Y. I. Galperin, R. Z. Sagdeev, F. K. Shuiskaya, Y. V. Lisakov, V. V. Migulin, et al., "Detection of Electron Acceleration in the Ionospheric Plasma under the Influence of High-Power Radio Radiation near the Local Plasma Frequency Aboard the Space Vehicle Interkosmos 19," *Cosmic Res.*, **19**, 1981, pp. 22-29.
21. H. Oya, A. Morioka, and T. Obara, "Leaked AKR and Terrestrial Hectometric Radiations Discovered by the Plasma Wave and Planetary Plasma Sounder Experiments on Board the Ohzora (EXOS-C) Satellite-Instrumentation and Observation Results of, Plasma Wave Phenomena," *J. Geomagn. Geoelectr.*, **37**, 1985, pp. 237-262.
22. P. M. E. Decreau, M. Hamlin, R. Massif, H. d. Feraudy, E. Pawela, et al., "Plasma Probing by Active Wave Experiments on the Viking Satellite," *Ann. Geophys.*, **5A**, 4, 1987, pp. 181-186.
23. F. K. Shuiskaya, Y. I. Galperin, A. A. Serov, N. V. Baranets, Y. V. Kushnerevsky, et al., "Resonant Heating of the Ionospheric Plasma by Powerful Radiopulses Aboard the Interkosmos-19 and Cosmos-1809 Satellites," *Planet. Space Sci.*, **38**, 1990, pp. 173-180.
24. H. G. James, "Guided Z Mode Propagation Observed in the OEDIPUS A Tethered Rocket Experiment," *J. Geophys. Res.*, **96**, 1991, pp. 17865-17878.
25. H. Oya, A. Morioka, K. Kobayashi, M. Iizima, T. Ono, et al., "Plasma Wave Observation and Sounder Experiments (PWS) Using the Akebono (EXOS-D) Satellite – Instrumentation and Initial Results Including Discovery of the High Altitude Equatorial Plasma Turbulence," *J. Geomagn. Geoelectr.*, **42**, 1990, pp. 411-442.
26. R. G. Stone et al., "Ulysses Radio and Plasma Wave Observations in the Jupiter Environment," *Science*, **257**, 1992, pp. 1524-1531.
27. V. A. Oshervich, R. F. Benson, J. Fainberg, R. G. Stone, and R. J. MacDowall, "Sounder Stimulated Dn Resonances in Jupiter's Io Plasma Torus," *J. Geophys. Res.*, **98**, 1993, pp. 18751-18756.
28. P. LeSager, P. Canu, and N. Cornilleau-Wehrin, "Impact of the Ulysses Velocity on the Diagnosis of the Electron Density by the Unified Radio and Plasma Wave Sounder in the Outskirts of the Io Torus," *J. Geophys. Res.*, **103**, 1998, pp. 26667-26677.
29. A. Kiraga, Z. Klos, H. Rothkaehl, Z. Zbyszynski, V. N. Oraevsky, et al., "Estimation of Electron Density of Ionospheric Plasma Using Wave, Impedance and Topside Sounder," *Adv. Space Res.*, **20**, 1997, pp. 1083-1095.
30. H. G. James and W. Calvert, "Interference Fringes Detected by OEDIPUS C," *Radio Sci.*, **33**, 1998, pp. 617-629.
31. D. A. Gurnett et al., "The Cassini Radio and Plasma Wave Investigation," *Space Sci. Rev.*, **114**, 2004, pp. 395-463.
32. N. P. Danilkin, "The Results of the Satellite Radio Sounding of the Ionosphere in the Vicinity of the F-Layer Maximum," *Int. J. Geomagn. Aeron.*, **2**, 2001, pp. 173-180.
33. B. W. Reinisch, D. M. Haines, K. Bibl, G. Cheney, I. A. Gulkin, et al., "The Radio Plasma Imager Investigation on the IMAGE Spacecraft," *Space Sci. Rev.*, **91**, 2000, pp. 319-359.
34. J. L. Green and B. W. Reinisch, "An Overview of Results from RPI on IMAGE," *Space Sci. Rev.*, **109**, 2003, pp. 183-210.
35. P. M. E. Decreau, P. Fergeau, V. Kramoselskikh, E. L. Guirriec, M. Leveque, et al., "Early Results from the Whisper Instrument on Cluster: An Overview," *Ann. Geophysicae*, **19**, 2001, pp. 1241-1258.
36. D. A. Gurnett et al., "Radar Soundings of the Ionosphere of Mars," *Science*, **310**, 2005, pp. 1929-1933.
37. W. L. Flock, *Electromagnetics and the Environment: Remote Sensing and Telecommunications*, Englewood Cliffs, New Jersey, Prentice-Hall, Inc., 1979.

38. J. E. Jackson, "A New Method for Obtaining Electron-Density Profiles from P^{\prime} - f Records," *J. Geophys. Res.*, **61**, 1956, pp. 107-127.
39. J. A. Ratcliffe, *The Magneto-Ionic Theory and Its Applications to the Ionosphere*, New York, Cambridge University Press, 1959.
40. K. G. Budden, *The Propagation of Radio Waves, the Theory of Radio Waves of Low Power in the Ionosphere and Magnetosphere*, New York, Cambridge University Press, 1985.
41. J. M. Kelso, *Radio Ray Propagation in the Ionosphere*, New York, McGraw-Hill Electronic Sciences Series, McGraw Hill, 1964.
42. K. Davies, *Ionospheric Radio Propagation*, Washington, National Bureau of Standards Monograph 80, US Government Printing Office, 1965.
43. H. Rishbeth and O. K. Garriot, *Introduction to Ionospheric Physics*, New York, Academic Press, 1969.
44. J. A. Ratcliffe, *An Introduction to the Ionosphere and Magnetosphere*, London, Cambridge University Press, 1972.
45. J. W. Wright and G. H. Smith, "Introductory Paper Review of Current Methods for Obtaining Electron-Density Profiles from Ionograms," *Radio Sci.*, **2**, 1967, pp. 1119-1125.
46. R. D. Hunsucker, *Radio Techniques for Probing the Terrestrial Ionosphere*, (Physics and Chemistry in Space, Volume 22), Berlin, Springer, 1991.
47. B. W. Reinisch, "Modern Ionosondes," in H. Kohl, R. Ruster, and K. Schlegel (eds.), *Modern Ionospheric Science*, Katlenburg-Lindau, Germany, European Geophysical Society, 1996, pp. 440-458.
48. B. W. Reinisch, I. A. Galkin, G. M. Khmyrov, A. V. Kozlov, K. Bibl, et al., "New Digisonde for Research and Monitoring Applications," *Radio Sci.*, **44**, 2009, RS0A24, doi:10.1029/2008RS004115.
49. N. A. Zaboltn, J. W. Wright, and G. A. Zhabankov, "NeXtYZ: Three Dimensional Electron Density Inversion for Dynasonde Ionograms," *Radio Sci.*, **41**, 2006, RS6S32, doi:10.1029/2005RS003352.
50. N. A. Zaboltn and J. W. Wright, "Principles of Dynasonde Data Acquisition and Processing," XXIX URSI General Assembly, Chicago, 2008, Paper GH11.
51. I. A. Galkin, G. M. Khmyrov, A. V. Kozlov, B. W. Reinisch, X. Huang, et al., "The Artist 5," in P. Song, J. Foster, M. Mendillo, and D. Bilitza, (eds.), *Cp974, Radio Sounding and Plasma Physics*, Lowell, Massachusetts, American Institute of Physics, 2008, pp. 150-159.
52. J. E. Jackson, "Alouette-ISIS Program Summary," NSSDC Report 86-09, National Space Science Data Center, Greenbelt, Maryland, 1986.
53. S. A. Pulnests and R. F. Benson, "Radio-Frequency Sounders in Space," in W. R. Stone (ed.), *Review of Radio Science 1996-1999*, Oxford, Oxford University Press, 1999, pp. 711-733.
54. J. E. Jackson, "Results from Alouette 1, Explorer 20, Alouette 2 and Explorer 31," NSSDC Report 88-10, National Space Science Data Center, Greenbelt, Maryland, 1988.
55. J. E. Jackson and E. S. Warren, "Objectives, History, and Principal Achievements of the Topside Sounder and ISIS Programs," *Proc. IEEE*, **57**, 1969, pp. 861-865.
56. R. F. Benson and D. Bilitza, "New Satellite Mission with Old Data: Rescuing a Unique Data Set," *Radio Sci.*, **44**, 2009, RS0A04, doi:10.1029/2008RS004036.
57. D. L. Carpenter, T. F. Bell, D. Chen, D. Ng, C. Baran, et al., "Proton Cyclotron Echoes and a New Resonance Observed by the Radio Plasma Imager Instrument on the IMAGE Satellite," *J. Geophys. Res.*, **112**, 2007, A08208, doi:10.1029/2006JA012139.
58. J. E. Jackson, "Comparisons Between Topside and Ground-Based Soundings," *Proc. IEEE*, **57**, 1969, pp. 976-985.
59. R. F. Benson, P. A. Webb, J. L. Green, D. L. Carpenter, V. S. Sonwalkar, et al., "Active Wave Experiments in Space Plasmas: The Z Mode," in J. W. LaBelle and R. A. Treumann (eds.), *Lect. Notes Phys. 687 Geospace Electromagnetic Waves and Radiation*, New York, Springer, 2006, pp. 3-35.
60. J. E. Jackson, "The Reduction of Topside Ionograms to Electron-Density Profiles," *Proc. IEEE*, **57**, 1969, pp. 960-976.
61. R. F. Benson, "Stimulated Plasma Waves in the Ionosphere," *Radio Sci.*, **12**, 1977, pp. 861-878.
62. E. L. Hagg, E. J. Hewens, and G. L. Nelms, "The Interpretation of Topside Sounder Ionograms," *Proc. IEEE*, **57**, 1969, pp. 949-960.
63. J. E. Titheridge and M. L. Heron, "The Production and Analysis of Transmission Ionograms," *Planet. Space Sci.*, **20**, 1972, pp. 2029-2038.
64. B. D. Muldrew, M. D. Litwack, and P. L. Timleck, "Interpretation of the Statistics of Occurrence of Alouette I Earth Echoes," *Planet. Space Sci.*, **15**, 1967, pp. 611-618.
65. W. M. Farrell, S. M. Clifford, S. M. Milkovich, J. J. Plaut, C. J. Leuschen, et al., "MARSIS Subsurface Radar Investigations of the South Polar Reentrant Chasma Australe," *J. Geophys. Res.*, **113**, 2008, E04002, doi:10.1029/2007JE002974.
66. R. F. Benson, J. L. Green, S. F. Fung, B. W. Reinisch, W. Calvert, et al., "Magnetospheric Radio Sounding on the IMAGE Mission," *Radio Sci. Bull.*, No. 285, 1998, pp. 9-20.
67. R. F. Benson and V. A. Osherovich, "Application of Ionospheric Topside-Sounding Results to Magnetospheric Physics and Astrophysics," *Radio Sci.*, **39**, 2004, RS1S28, doi:10.1029/2002RS002834.
68. R. F. Benson, V. A. Osherovich, J. Fainberg, and B. W. Reinisch, "Classification of IMAGE/RPI-Stimulated Plasma Resonances for the Accurate Determination of Magnetospheric Electron-Density and Magnetic Field Values," *J. Geophys. Res.*, **108**, 2003, 1207, doi:10.1029/2002JA009589.
69. J. L. Donley, L. H. Brace, J. A. Findlay, J. H. Hoffman, and G. L. Wrenn, "Comparison of Results of Explorer XXXI Direct Measurement Probes," *Proc. IEEE*, **57**, 1969, pp. 1078-1084.
70. G. L. Wrenn and P. A. Smith, "Results Derived from Simultaneous Measurements Using the Langmuir Plate and Spherical Ion Probe on Explorer XXXI and the Ionosonde on Alouette II," *Proc. IEEE*, **57**, 1969, pp. 1085-1089.

71. L. H. Brace and J. A. Findlay, "Comparison of Cylindrical Electrostatic Probe Measurements on Alouette II and Explorer XXXI Satellites," *Proc. IEEE*, **57**, 1969, pp. 1057-1060.
72. R. F. Benson, P. A. Webb, J. L. Green, L. Garcia, and B. W. Reinisch, "Magnetospheric Electron Densities Inferred from Upper-Hybrid Band Emissions," *Geophys. Res. Lett.*, **31**, 2004, L20803, doi:10.2929/2004GL020847.
73. R. F. Benson, "Elusive Upper Hybrid Waves in the Auroral Topside Ionosphere," in R. L. Lysak (ed.), *Auroral Plasma Dynamics, Geophysical Monograph 80*, Washington, DC, American Geophysical Union, 1993, pp. 267-274.
74. J. E. Jackson, "The Analysis of Topside Ionograms," Goddard Space Flight Center Report X-615-67-452, Greenbelt, Maryland, 1967.
75. J. E. Jackson, E. R. Schmerling, and J. H. Whitteker, "Mini-Review on Topside Sounding," *IEEE Trans. Antennas Propagat.*, **AP-28**, 1980, pp. 284-288.
76. G. E. K. Lockwood, "A Modified Iteration Technique for Use in Computing Electron Density Profiles from Topside Ionograms," *Radio Sci.*, **5**, 1970, pp. 575-577.
77. N. P. Danilkin, P. F. Denisenko, and V. V. Sotsky, "Peculiarities of the Inverse Problems of Vertical Radio Sounding of the Ionosphere," *Adv. Space Res.*, **8**, 1988, pp. (4)91-(4)94.
78. J. W. Wright and M. L. V. Pitteway, "Data Acquisition and Analysis for Research Ionograms" in Computer Aided Processing of Ionograms and Ionosonde Records, Rep. UAG-105, Boulder, World Data Center A for Solar Terrestrial Physics, 1998. p. 1-11.
79. B. W. Reinisch and X. Huang, "Automatic Calculation of Electron Density Profiles from Digital Ionograms. 1. Automatic O and X Trace Identification for Topside Ionograms," *Radio Sci.*, **17**, 1982, pp. 421-434.
80. X. Huang and B. W. Reinisch, "Automatic Calculation of Electron Density Profiles from Digital Ionograms 2. True Height Inversion of Topside Ionograms with the Profile-Fitting Method," *Radio Sci.*, **17**, 1982, pp. 837-844.
81. X. Huang, B. W. Reinisch, D. Bilitza, and R. F. Benson, "Electron Density Profiles of the Topside Ionosphere," *Ann. Geophys.*, **45**, 2002, pp. 125-130.
82. D. Bilitza, X. Huang, B. W. Reinisch, R. F. Benson, H. K. Hills, et al., "Topside Ionogram Scaler with True Height Algorithm (TOPIST): Automated Processing of ISIS Topside Ionograms," *Radio Sci.*, **39**, 2004, RS1S27, doi:10.1029/2002RS002840.
83. D. L. Carpenter, T. F. Bell, U. S. Inan, R. F. Benson, V. S. Sonwalkar, et al., "Z-Mode Sounding within Propagation 'Cavities' and Other Inner Magnetospheric Regions by the RPI Instrument on the IMAGE Satellite," *J. Geophys. Res.*, **108**, A12, 2003, 1421, doi:10.1029/2003JA010025.
84. D. A. Gurnett, S. D. Shawhan, and R. R. Shaw, "Auroral Hiss, Z Mode Radiation, and Auroral Kilometric Radiation in the Polar Magnetosphere: DE 1 Observations," *J. Geophys. Res.*, **88**, 1983, pp. 329-340.
85. X. Huang, B. W. Reinisch, P. Song, P. Nsumei, J. L. Green, et al., "Developing an Empirical Density Model of the Plasmasphere Using IMAGE/RPI Observations," *Adv. Space Res.*, **33**, 2004, pp. 829-832.
86. D. B. Muldrew, "Nonvertical Propagation and Delayed-Echo Generation Observed by the Topside Sounders," *Proc. IEEE*, **57**, 1969, pp. 1097-1107.
87. V. S. Sonwalkar, D. L. Carpenter, T. F. Bell, M. A. Spasojevic, U. S. Inan, et al., "Diagnostics of Magnetospheric Electron Density and Irregularities at Altitudes < 5000 km using Whistler and Z Mode Echoes from Radio Sounding on the IMAGE Satellite," *J. Geophys. Res.*, **109**, 2004, A11212, doi:10.1029/2004JA010471.
88. W. Calvert and J. M. Warnock, "Ionosphere Irregularities Observed by Topside Sounders," *Proc. IEEE*, **57**, 1969, pp. 1019-1025.
89. J. H. Whitteker, L. H. Brace, E. J. Maier, J. R. Burrows, W. H. Dodson, et al., "A Snapshot of the Polar Ionosphere," *Planet. Space Sci.*, **24**, 1976, pp. 25-32.
90. F. Daniels, "ISIS-II Spacecraft," CRC Report No. 1218, Ottawa, Communications Research Centre, 1971.
91. W. R. Hoegy and R. F. Benson, "De/ISIS Conjunction Comparisons of High-Latitude Electron Density Features," *J. Geophys. Res.*, **93**, 1988, pp. 5947-5954.
92. R. F. Benson, "Auroral Kilometric Radiation: Wave Modes, Harmonics and Source Region Electron Density Structures," *J. Geophys. Res.*, **90**, 1985, pp. 2753-2784.
93. J. M. Grebowsky, R. F. Benson, P. A. Webb, V. Truhlik, and D. Bilitza, "Altitude Variation of the Plasmopause Signature in the Main Ionospheric Trough," *J. Atmos. Solar-Terr. Phys.*, **71**, 2009, pp. 1669-1676, doi:10.1016/j.jastp.2009.05.016.
94. K. L. Chan and L. Colin, "Global Electron Density Distributions from Topside Soundings," *Proc. IEEE*, **57**, 1969, pp. 990-1004.
95. D. B. Bilitza, B. W. Reinisch, S. M. Radicella, S. Pulinets, T. Gulyaeva, et al., "Improvements of the International Reference Ionosphere Model for the Topside Electron Density Profile," *Radio Sci.*, **41**, 2006, RS5S15, doi:10.1029/2005RS003370.
96. B. W. Reinisch, P. Nsumei, X. Huang, and D. K. Bilitza, "Modeling the F2 Topside and Plasmasphere for IRI Using IMAGE/RPI, and ISIS Data," *Adv. Space Res.*, **39**, 2007, doi:10.1016/j.asr.2006.05.032.
97. C. Rush, M. Fox, D. Bilitza, K. Davies, L. McNamara, et al., "Ionosphere Mapping: An Update of foF2 Coefficients," *Telecommunication J.*, **56**, 1989, pp. 179-182.
98. S. A. Pulinets, V. P. Kim, V. V. Hegai, V. K. Depuev, and S. M. Radicella, "Unusual Longitude Modification of the Night-Time Midlatitude F2 Region Ionosphere in July 1980 over the Array of Tectonic Faults in the Andes Area: Observations and Interpretation," *Geophys. Res. Lett.*, **25**, 1998, pp. 4133-4136.
99. L. Colin and K. L. Chan, "Model Studies of the Kinked Z Trace in Topside Ionograms," *Proc. IEEE*, **57**, 1969, pp. 1143-1147.
100. J. R. McAfee, "Ray Trajectories in an Anisotropic Plasma near Plasma Resonance," *J. Geophys. Res.*, **73**, 1968, pp. 5577-5583.
101. J. R. McAfee, "Topside Ray Trajectories near the Upper Hybrid Resonance," *J. Geophys. Res.*, **74**, 1969, pp. 6403-6408.
102. D. B. Muldrew, "Electron Resonances Observed with Topside Sounders," *Radio Sci.*, **7**, 1972, pp. 779-789.

103. R. F. Benson, "Plasma Physics Using Space-Borne Radio Sounding," in P. Song, J. Foster, M. Mendillo, and D. Bilitza (eds.), *CP974, Radio Sounding and Plasma Physics*, Lowell, Massachusetts, American Institute of Physics, 2008, pp. 20-33.
104. R. F. Benson and J. Bitoun, "Interpretation of Satellite Gyroharmonic Resonance Observations," *Radio Sci.*, **14**, 1979, pp. 113-123.
105. D. B. Muldrew, "The Poynting Vector Applied to the Complex Refractive Index in a Hot Plasma near the Electron-Cyclotron Frequency, and to the Cyclotron Resonance Observed on Topside Ionograms," *Radio Sci.*, **41**, 2006, RS6006, doi:10.1029/2006RS003496.
106. R. F. Benson, "Ionospheric Plasma Resonances: Time Durations vs. Latitude, Altitude, and fN/fH ," *Planet. Space Sci.*, **20**, 1972, pp. 683-706.
107. E. S. Warren and E. L. Hagg, "Observation of Electrostatic Resonances of the Ionospheric Plasma," *Nature*, **220**, 1968, pp. 466-468.
108. H. Oya, "Sequence of Diffuse Plasma Resonances Observed on Alouette 2 Ionograms," *J. Geophys. Res.*, **75**, 1970, pp. 4279-4285.
109. G. L. Nelms and G. E. K. Lockwood, "Early Results from the Topside Sounder in the Alouette II Satellite," in R. L. Smith-Rose (ed.), *Space Research VII*, Amsterdam, North-Holland Publishing Co., 1967, pp. 604-623.
110. D. B. Muldrew, "Electrostatic Resonances Associated with the Maximum Frequencies of Cyclotron-Harmonic Waves," *J. Geophys. Res.*, **77**, 1972, pp. 1794-1801.
111. R. F. Benson, V. A. Osherovich, J. Fainberg, A. F.-Viñas, and D. R. Ruppert, "An Interpretation of Banded Magnetospheric Radio Emissions," *J. Geophys. Res.*, **106**, 2001, pp. 13179-13190.
112. V. A. Osherovich, "Physical Nature of the Diffuse Plasma Resonances in the Ionosphere," *J. Geophys. Res.*, **92**, 1987, pp. 316-320.
113. V. A. Osherovich, R. F. Benson, and J. Fainberg, "Electromagnetic Bounded States and Challenges of Plasma Spectroscopy," *IEEE Trans. Plasma Sci.*, **33**, 2005, pp. 599-608.
114. V. A. Osherovich, "Cylindrical Oscillations of Force-Free Electromagnetic Fields," *Astrophys. Space Sci.*, **121**, 1986, pp. 255-264.
115. V. A. Osherovich, "Cylindrical Oscillations of Force-Free Electromagnetic Fields," *Astrophys. Space Sci.*, **127**, 1986, pp. 185-187.
116. V. A. Osherovich and E. B. Gliner, "Force-Free Electromagnetic Waves," *Solar Physics*, **117**, 1988, pp. 391-397.
117. R. L. Stenzel and J. M. Urrutia, "Force-Free Electromagnetic Pulses in a Laboratory Plasma," *Phys. Rev. Lett.*, **65**, 1990, pp. 2011-2014.
118. H. Oya, "Verification of Theory on Weak Turbulence Relating to the Sequence of Diffuse Plasma Resonances in Space," *Phys. Fluids*, **14**, 1971, pp. 2487-2499.
119. V. A. Osherovich, "The Physical Nature of the Upper Subsidiary Diffuse Resonances," *J. Geophys. Res.*, **94**, 1989, pp. 5530-5532.
120. V. A. Osherovich and R. F. Benson, "The Lower Subsidiary Diffuse Plasma Resonances and the Classification of Radio Emissions Below the Plasma Frequency," *J. Geophys. Res.*, **96**, 1991, pp. 19331-19341.
121. G. Belmont, "Characteristic Frequencies of a Non-Maxwellian Plasma: A Method for Localizing the Exact Frequencies of Magnetospheric Intense Natural Waves near f_{pe} ," *Planet. Space Sci.*, **29**, 1981, pp. 1251-1266.
122. J. G. Trotignon, P. M. E. Decreau, J. L. Rauch, O. Randriamboarison, V. Krasnoselskikh, et al., "How to Determine the Thermal Electron Density and the Magnetic Field Strength from the Cluster/Whisper Observations around the Earth," *Ann. Geophysicae*, **19**, 2001, pp. 1711-1720.
123. A. F. Viñas, R. L. Mace, and R. F. Benson, "Dispersion Characteristics for Plasma Resonances of Maxwellian and Kappa Distribution Plasmas and their Comparisons to the IMAGE/RPI Observations," *J. Geophys. Res.*, **110**, 2005, A06202, doi:10.1029/2004JA010967.
124. B. Higel, "Small Scale Structure of Magnetospheric Electron Density through on-Line Tracking of Plasma Resonances," *Space Sci. Rev.*, **22**, 1978, pp. 611-631.
125. R. F. Benson, "Stimulated Plasma Instability and Nonlinear Phenomena in the Ionosphere," *Radio Sci.*, **17**, 1982, pp. 1637-1659.
126. E. L. Hagg and D. B. Muldrew, "A Novel Spike Observed on Alouette II Ionograms," in J. O. Thomas and B. J. Landmark (eds.), *Plasma Waves in Space and Laboratory*, Edinburgh, Edinburgh University Press, 1970, pp. 69-75.
127. H. Oya and R. F. Benson, "A New Method for in Situ Electron Temperature Determinations from Plasma Wave Phenomena," *J. Geophys. Res.*, **77**, 1972, pp. 4272-4276.
128. R. F. Benson, "Ion Effects on Ionospheric Electron Resonance Phenomena," *Radio Sci.*, **10**, 1975, pp. 173-185.
129. R. F. Benson and V. A. Osherovich, "High Order Stimulated Ionospheric Diffuse Plasma Resonances – Significance to Magnetospheric Emissions," *J. Geophys. Res.*, **97**, 1992, pp. 19413-19419.
130. W. Calvert, "Oblique Z-Mode Echoes in the Topside Ionosphere," *J. Geophys. Res.*, **71**, 1966, pp. 5579-5583.
131. R. F. Benson, "An Appreciation of Paul A. Siple," *Eos Trans. AGU*, **75**, 1994, pp. 355 and 361 (also published in *Earth in Space* in September).
132. C. D. Florida "The Development of a Series of Ionospheric Satellites," *Proc. IEEE*, **59**, 1969, pp. 867-875.
133. J. Mar and T. Garrett, "Mechanical Design and Dynamics of the Alouette Spacecraft," *Proc. IEEE*, **59**, 1969, pp. 882-896.
134. C. Franklin, "Alouette/ISIS: How it all Began, Presentation to the IEEE International Milestone in Engineering Ceremony, May 13, 1993, Ottawa," <http://iee.ca/diglib/library/milestone/keynote.htm>.
135. C. Franklin, Personal Communication, 2006.
136. J. R. McAfee, "Topside Resonances as Oblique Echoes," *J. Geophys. Res.*, **74**, 1969, pp. 802-808.

137. H. G. James, "Slow Z-Mode Radiation from Sounder-Accelerated Electrons," *J. Atmos. Solar-Terr. Phys.*, **66**, 2004, pp. 1755-1765.
138. H. G. James, "Characteristics of Field-Aligned Density Depletion Irregularities in the Auroral Ionosphere that Duct Z- and X-Mode Waves," *J. Geophys. Res.*, **111**, 2006, A09315, doi:10.2929/2006JA011652.
139. J. L. Green, "The Struggle to Get RPI on the IMAGE Mission," in P. Song, J. Foster, M. Mendillo, and D. Bilitza (eds.), *CP974, Radio Sounding and Plasma Physics*, Lowell, Massachusetts, American Institute of Physics, 2008, pp. 3-8.
140. W. Calvert, R. F. Benson, D. L. Carpenter, S. F. Fung, D. L. Gallagher, et al., "The Feasibility of Radio Sounding in the Magnetosphere," *Radio Sci.*, **30**, 1995, pp. 1577-1595.
141. D. L. Carpenter, "Highlights of RPI Sounding of the Plasmasphere and Polar Regions at Frequencies in the Whistler and Z-Mode Domains," in P. Song, J. Foster, M. Mendillo, and D. Bilitza (eds.), *CP974, Radio Sounding and Plasma Physics*, Lowell, Massachusetts, American Institute of Physics, 2008, pp. 89-96.
142. S. F. Fung, "Radio Plasma Imager and Measurement of Magnetospheric Field-Aligned Electron Density," in P. Song, J. Foster, M. Mendillo, and D. Bilitza (eds.), *CP974, Radio Sounding and Plasma Physics*, Lowell, Massachusetts, American Institute of Physics, 2008, pp. 97-110.
143. I. A. Galkin, G. M. Khmyrov, A. V. Kozlov, and B. W. Reinisch, "Intelligent Resident Archive for RPI Level 2 Data," in P. Song, J. Foster, M. Mendillo, and D. Bilitza (eds.), *CP974, Radio Sounding and Plasma Physics*, Lowell, Massachusetts, American Institute of Physics, 2008, pp. 111-117.
144. J. DeKeyser, D. L. Carpenter, F. Darrouzet, D. L. Gallagher, and J. Tu, "CLUSTER and IMAGE: New Ways to Study the Earth's Plasmasphere," *Space Sci. Rev.*, **145**, 2009, pp. 7-53, doi:10.1007/s11214-008-9464-7.
145. F. Darrouzet, D. L. Gallagher, N. André, D. L. Carpenter, I. Dandouras, et al., "Plasmaspheric Density Structures and Dynamics: Properties Observed by the CLUSTER and IMAGE Missions," *Space Sci. Rev.*, **145**, 2009, pp. 55-106, doi:10.1007/s11214-008-9438-9.
146. A. Masson, O. Santolík, D. L. Carpenter, F. Darrouzet, P. M. E. Décréau, et al., "Advances in Plasmaspheric Wave Research with CLUSTER and IMAGE Observations," *Space Sci. Rev.*, **145**, 2009, pp. 137-191, doi:10.1007/s11214-009-9508-7.
147. B. W. Reinisch, M. B. Moldwin, R. E. Denton, D. L. Gallagher, H. Matsui, et al., "Augmented Empirical Models of Plasmaspheric Density and Electric Field Using IMAGE and CLUSTER data," *Space Sci. Rev.*, **145**, 2009, pp. 231-261, doi:10.1007/s11214-008-9481-6.
148. P. M. E. Decreau, P. Ferreau, V. Krannoselskikh, M. Leveque, P. Martin, et al., "WHISPER, a Resonance Sounder and Wave Analyser: Performances and Perspectives for the Cluster Mission," *Space Sci. Rev.*, **79**, 1997, pp. 157-193.
149. J. G. Trotignon, J. L. Rauch, P. M. E. Decreau, P. Canu, and J. Lemaire, "Active and Passive Plasma Wave Investigations in the Earth's Environment: The Cluster/WHISPER Experiment," *Adv. Space Res.*, **31**, 2003, pp. 1449-1454.
150. W. Calvert and J. R. McAfee, "Topside-Souder Resonances," *Proc. IEEE*, **57**, 1969, pp. 1089-1096.
151. J. R. McAfee, "Electron Plasma Resonances in the Topside Ionosphere," *Fundam. Cosmic Phys.*, **1**, 1974, pp. 71-117.
152. G. E. K. Lockwood, "Excitation of Cyclotron Spikes in the Ionospheric Plasma," *Can. J. Phys.*, **43**, 1965, pp. 291-297.
153. R. F. Benson, "Stimulation of the Harris Instability in the Ionosphere," *Phys. Fluids*, **17**, 1974, pp. 1032-1037.
154. J. Bitoun, L. Fleury, and B. Higel, "Theoretical Study of Gyroresonances with Application to Rocket Experiments," *Radio Sci.*, **10**, 1975, pp. 875-889.
155. R. F. Benson, "An Analysis of Alouette I Plasma Resonance Observations," in J. O. Thomas and B. J. Landmark (eds.), *Plasma Waves in Space and Laboratory*, Edinburgh, Edinburgh University Press, 1970, pp. 25-54.
156. L. Fleury and M. Petit, "Antenna Dependence of Plasma Resonance Patterns," *J. Geophys. Res.*, **79**, 1974, pp. 4817-4820.
157. J. W. King and D. M. Preece, "Observations of Proton Gyro-Effects in the Topside Ionosphere," *J. Atm. and Terr. Phys.*, **29**, 1967, pp. 1387-1390.
158. R. E. Horita, "Proton Cyclotron Frequency Phenomena in the Topside Ionosphere," *Planet. Space Sci.*, **22**, 1974, pp. 793-799.
159. R. E. Horita, "Proton Cyclotron Echoes and Spurs Observed on Alouette II and ISIS II," *Radio Sci.*, **22**, 1987, pp. 671-686.
160. H. Oya, "Generation Mechanism of Proton Cyclotron Echoes Due to Pulsed Radio Frequency Waves in Space Plasma," *J. Geophys. Res.*, **83**, 1978, pp. 1991-2008.
161. G. M. Chen and R. E. Horita, "Proton Cyclotron Echoes at 3fH and 4fH Resonances," *Radio Sci.*, **26**, 1991, pp. 23-29.
162. D. B. Muldrew, "Topside-Souder Proton-Cyclotron Echo Generation from a Plasma Memory Process and Electron Bernstein-Wave Propagation," *Radio Sci.*, **33**, 1998, pp. 1395-1411.
163. D. B. Muldrew, "Correction To 'Topside-Souder Proton-Cyclotron Echo Generation from a Plasma Memory Process and Electron Bernstein-Wave Propagation' by D. B. Muldrew," *Radio Sci.*, **35**, 2000, pp. 1047-1048.
164. R. F. Benson, "Evidence for the Stimulation of Field-Aligned Electron Density Irregularities on a Short Time Scale by Ionospheric Topside Sounders," *J. Atm. and Solar-Terr. Phys.*, **59**, 1997, pp. 2281-2293.
165. N. A. Zaboltn, D. S. Bratsun, S. A. Pulnits, and R. F. Benson, "Response of Topside Radio Sounding Signals to Small-Scale Field-Aligned Ionospheric Irregularities," *J. Atm. and Solar-Terr. Phys.*, **59**, 1997, pp. 2231-2246.
166. V. A. Oshervich, J. Fainberg, R. F. Benson, and R. G. Stone, "Theoretical Analysis of Resonance Conditions in Magnetized Plasmas When the Plasma/Gyro Frequency Ratio is Close to an Integer," *J. Atm. and Solar-Terr. Phys.*, **59**, 1997, pp. 2361-2366.
167. S. P. Kuo, M. C. Lee, and P. Kossey, "Excitation of Short-Scale Field-Aligned Electron Density Irregularities by Ionospheric Topside Sounders," *J. Geophys. Res.*, **104**, 1999, pp. 19889-19894.

168. R. F. Benson, J. Fainberg, R. A. Hess, V. A. Osherovich, and R. G. Stone, "An Explanation for the Absence of Sounder-Stimulated Gyroharmonic Resonances in the Io Plasma Torus by the Ulysses Relaxation Sounder," *Radio Sci.*, **32**, 1997, pp. 1127-1134.
169. P. Canu, "Observation of Long-Duration Gyroharmonic Resonances: A Refutation of the Short-Duration Explanation for Interpreting the Anomalous URAP Sounder Spectra Observed in the Io Torus," *Radio Sci.*, **36**, 2001, pp. 171-181.
170. R. F. Benson, J. Fainberg, R. A. Hess, V. A. Osherovich, and R. G. Stone, "Comment On 'Observation of Long-Duration Gyroharmonic Resonances: A Refutation of the Short-Duration Explanation for Interpreting the Anomalous URAP Sounder Spectra Observed in the Io Torus' by P. Canu," *Radio Sci.*, **36**, 2001, pp. 1649-1652.
171. P. Canu, "Reply," *Radio Sci.*, **36**, 2001, pp. 1645-1647.
172. D. B. Muldrew, "Radio Propagation Along Magnetic Field-Aligned Sheets of Ionization Observed by the Alouette Topside Sounder," *J. Geophys. Res.*, **68**, 1963, pp. 5355-5370.
173. R. A. Helliwell, *Whistlers and Related Ionospheric Phenomena*, Stanford, California, Stanford University Press, 1965.
174. W. Calvert, "Wave Ducting in Different Wave Modes," *J. Geophys. Res.*, **100**, 1995, pp. 17491-17497.
175. D. L. Carpenter, M. A. Spasojevic, T. F. Bell, U. S. Inan, B. W. Reinisch, et al., "Small-Scale Field-Aligned Plasmaspheric Density Structures Inferred from RPI on IMAGE," *J. Geophys. Res.*, **107**, A9, 2002, 1258, doi:10.1029/2001JA009199.
176. S. F. Fung, R. F. Benson, D. L. Carpenter, J. L. Green, V. Jayanti, et al., "Guided Echoes in the Magnetosphere: Observations by Radio Plasma Imager on IMAGE," *Geophys. Res. Lett.*, **30**, 11, 2003, 1589, doi:10.1029/2002GL016531.
177. P. L. Dyson and R. F. Benson, "Topside Sounder Observations of Equatorial Bubbles," *Geophys. Res. Lett.*, **5**, 1978, pp. 795-798.
178. R. F. Benson, "Field-Aligned Electron Density Irregularities Near 500 km – Equator to Polar Cap Topside Sounder Z Mode Observations," *Radio Sci.*, **20**, 1985, pp. 477-485.
179. B. W. Reinisch, X. Huang, P. Song, G. S. Sales, S. F. Fung, et al., "Plasma Density Distribution Along the Magnetospheric Field: RPI Observations from IMAGE," *Geophys. Res. Lett.*, **28**, 2001, pp. 4521-4524.
180. D. B. Muldrew, "Characteristics of the Coupled Z Mode at Arecibo," *Radio Sci.*, **28**, 1993, pp. 379-388.
181. D. B. Muldrew, "Correction To 'Characteristics of the Coupled Z Mode at Arecibo' by D. B. Muldrew," *Radio Sci.*, **29**, 1994, pp. 673-674.
182. B. W. Reinisch, X. Huang, P. Song, J. L. Green, S. F. Fung, et al., "Plasmaspheric Mass Loss and Refilling as a Result of a Magnetic Storm," *J. Geophys. Res.*, **109**, 2004, A01202, doi:10.1029/2003JA009948.

Picosecond-Level Error Detection Using PCA in the Hardware Timing Systems for the EISCAT_3D LAAR



Gustav Johansson
Fredrik Häglund
Johan E. Carlson
Jonny Johansson

Abstract

While developing the timing system for the receiver arrays for the EISCAT_3D system, several approaches for detecting and adjusting for timing errors within the array have been explored. Since the lengths of the radar pulses are shorter than the size of the aperture, time-delay beamforming is necessary, which puts high demands on the timing system. The demand on the timing error among all elements in the array is to have a standard deviation of less than 120 ps. This requires high-quality error-detection systems to guarantee radar operation. This paper investigates the qualities of a secondary error-detection system based on statistical analysis of captured data.

The measurements were assembled with a signal-to-noise ratio (SNR) of -30 dB, implying that the elements in a 2112 element array needed to be grouped into subarrays of 48 elements each. The captured data was then evaluated by principal-component analysis (PCA) and averaged over 20,000 measurements, or about half a second. Timing errors between subarrays of down to ~ 120 ps and a percentage of faulty subarrays of up to 20% were detectable.

Principal-component analysis can be used as a cheap secondary error-detection system because it only needs a small amount of computer time to implement. In addition, it acts as a detection system for hardware errors in the primary timing system that are undetectable without a secondary system.

1. Introduction

EISCAT_3D is a design study of a new Incoherent-Scatter Radar (ISR) that is based on a Large-Aperture-Array Radar (LAAR) system, where *Large Aperture* refers to

the fact that the incoming radar pulses are shorter than the aperture of the radar. This renders it necessary for the radar to use time-delay [1] beamforming, as opposed to phase-delay [1] beamforming. The addition of high demands on the pointing accuracy, $< \pm 0.06^\circ$, and low beamforming loss, < 0.2 dB, have put stringent demands on the timing system of the array.

During the development of the receiver hardware for the EISCAT_3D[2] radar test array, one of the main focus areas has been the timing system. Because of the necessity of very low errors in the timing – an error with a standard deviation of less than 120 ps [3] – a continuous timing-calibration system has been built. While this cable-calibration system currently is under evaluation in the test array, another approach for detecting timing errors has been evaluated.

This paper describes the method, which uses principal-component analysis (PCA) to find any subarrays in a digitally sampled array where the timing of the signal differs significantly from the other subarrays. The incoming radar signals are well below the noise floor (-30 dB for a single antenna element), and the method is shown to work without prior knowledge of the incoming signal. It can thus be used while the radar is operating.

This error-detection method is *not* intended to replace the cable-calibration system, but is rather a supplemental detection system to lower the risk of degradation of the functionality of the EISCAT_3D radar. An important difference between the two systems is the capacity in which they are used. The cable-calibration system is only continuous on a large scale, since it is an active calibration system. It injects a signal into different signal paths in the array, effectively drowning out any other signals. It can thus only be used during radar down times, e.g., between pulses or experiments. The method proposed in this paper

Gustav Johansson, Fredrik Häglund, and Jonny Johansson are with EISLAB – Luleå University of Technology, SE-971 87 Luleå, Sweden; Tel: +46 920 492138; Fax: +46 920 492191; E-mail: gustav_j@ltu.se. Johan E. Carlson is with the Division of Systems and Interaction – Luleå University of Technology, Luleå, Sweden.

is a passive monitoring system that uses statistical methods to find timing errors in signals buried in noise. It can thus be used continuously, during both active radar operation and the radar-calibration mode.

Another important difference is the accuracy of the detection method, itself. The cable-calibration system measures an absolute timing error with a high accuracy. Simulations show that an error with a standard deviation of less than 50 ps should be achievable for the timing, and an amplitude error of less than 8%. The statistical method in this paper does not reveal an absolute error at all, but can only indicate that an element is unsynchronized with the other elements. However, if more than one error is detected, a relative difference in magnitude of the error is discernible. As for amplitude errors, no indication at all is given by the statistical method.

Other methods of sub-noise-signal error detection that were considered included correlation, which, for example, is used in global navigation satellite systems [4]. However, these were not as successful for small errors, and took more than twice the computational time to process.

It is important to note that since the radar pulses are shorter than the aperture of the array, it is essential for the functionality of the principal-component analysis method that enough samples are used in the analysis to ensure that at least one complete radar pulse has been recorded at every element in the array.

The remainder of this paper will go through the methods used, the results, and finally, the conclusions.

2. Method

The signals coming into the EISCAT_3D radar array are very weak. A reasonable assumption is for the signal to have a signal-to-noise ratio (SNR) of about -30 dB for a single antenna element. However, the antennas in

the array are grouped into subarrays of 48 antennas each, thereby increasing the SNR to about -10 dB. This is the level that has been used in simulations of the EISCAT_3D system using the Large-Aperture-Array Radar Simulation Environment (LAARSE) [5].

The incoming signal of the EISCAT_3D radar is located in a 30 MHz-wide band centered at around 220 MHz, and contains a number of different frequencies. While real data could be used to test the statistical method, the test array built in Kiruna, Sweden, is too small to test the method, since it only contains one subarray. Instead, the method has been evaluated using the Large-Aperture-Array Radar Simulation Environment to simulate a larger version of the EISCAT_3D test array. The target size of a receiver array in the EISCAT_3D project is between 2,000 to 16,000 antenna elements. The simulations made in this paper were based on the smaller version of these, simulating an 88×24 element array, yielding 2,112 antenna elements in the array in $M = 44$ subarrays.

2.1 Statistical Method

Principal-component analysis (PCA) is a well-known statistical method for analyzing multivariate data [6]. Through the analysis, the principal components of the data are calculated, which can be thought of as an alternative way to describe the data by as few variables as possible. From these components, principal-component scores (PCS) can be calculated for each data row of the analyzed data set. This is a single number per component that describes how well the principal components describe that row.

Another way to look at principal-component analysis is through a geometrical interpretation. Each successive component in the principal-component analysis will describe the largest variation in the data not already described by a previous component. In the two-dimensional case, an example set of data is plotted in Figure 1. The data forms a cloud centered around the origin, and when performing

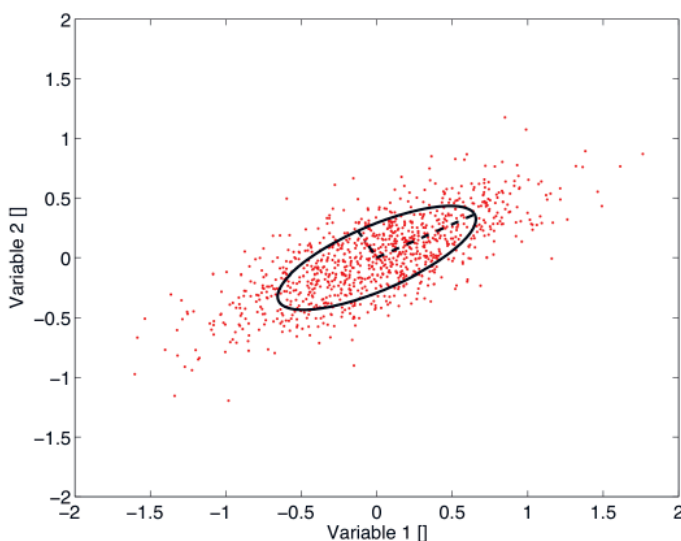


Figure 1. The geometrical interpretation of the principal-component analysis (PCA) in two dimensions. A data set of 1000 randomly generated points that had an elliptic distribution were analyzed with principal-component analysis. The two first components were plotted with dashed and dash-dot lines, respectively. A solid-line representation of the two-dimensional Gaussian distribution contour that they described is also included.

a principal-component analysis on the data set, the two first principal components will point in the directions of the largest variation. The components of the principal-component analysis will in this case describe the contour of a two-dimensional Gaussian distribution plot of the data. It is thus clear that not only the direction of the largest variation is deduced, but also a measure of the relative magnitude of the variation. Increasing the number of components in the principal-component analysis in this simple case would not improve the results any further, since we only had a two-dimensional data set from the start. On the other hand, a data set that would seem to be three-dimensional might very well be described sufficiently well by only two principal components, or by even a single component. When the dimensionality of a problem increases, the geometrical interpretation loses its lucidity, but from an understanding point of view, it gives a clear example in the two- and three-dimensional cases.

2.2 Method of Application

When applied to the data from a number of different subarrays in the EISCAT_3D radar, the principal-component analysis will detect any subarray that has a component of data that differs from the rest of the subarrays. In a perfectly synchronized array, the results will not reveal any differences, since the signal part of the data is the same for all subarrays. However, if a subarray is unsynchronized with the others, it will by itself generate a higher principal-component score, since its data have a part that is different from all of the other subarrays.

The data from the subarrays in the Large-Aperture-Array Radar Simulation Environment simulations of the EISCAT_3D radar were collected in a matrix as follows:

$$\mathbf{X} = \begin{bmatrix} \mathbf{x}_1 \\ \mathbf{x}_2 \\ \vdots \\ \mathbf{x}_M \end{bmatrix}, \quad (1)$$

where $M = 44$ is the total number of subarrays, and $\mathbf{x}_m = [x[0].x[1] \cdots x[N]]$ is the sampled data from the m th subarray, with $N = 257$ samples. In \mathbf{X} , the mean was subtracted from the columns to center the data. The principal components, \mathbf{a}_j for $j = 1, 2, \dots, N$, of \mathbf{X} were calculated. The property of the principal-component analysis, where each successive component describes the largest variation of the data not already described by previous components, was used to describe the data. Since the signals were buried in noise, it was enough to monitor only the first principal component, since this component describes the noise. That is, the variation in the direction of the first principal component, \mathbf{a}_1 , was enough to describe the data set. Since the noise was the largest contributor to the analyzed data, it was thus described by the first component.

The principal-component score, y_m , for $m = 1, 2, \dots, M$ for the data were calculated as

$$\mathbf{y} = \mathbf{X}\mathbf{a}_1, \quad (2)$$

resulting in an $(M \times 1)$ vector with the scores y_m for the M subarrays by using only the first principal component. Looking at the principal-component score of the first component, a score that differs from the average score could be attributed to a difference in the underlying signal with respect to the data set. However, a single evaluation would not reveal this difference with any certainty, thus requiring a larger set of data on which to perform the analysis.

To provide the larger data set, all simulations were made $K = 20,000$ times, and thereafter the analysis was conducted. With a data length of $N = 257$ samples at 80 MHz sampling frequency, each data set corresponded to $\sim 3.2 \mu\text{s}$. Thus, 20,000 sets of data at 12.5% duty cycle of the radar were collected in 514 ms.

2.3 Experimental Setup

In the Large-Aperture-Array Radar Simulation Environment, a signal is generated at the incoming frequencies and was, in the data used in this paper, constructed from four randomly placed signals within the signal band. The Large-Aperture-Array Radar Simulation Environment simulates every step of the receiving array, from input filters to analog-to-digital converters (ADC) and beamforming. The output from the simulations used for further investigation was the beam-formed signal from each antenna subarray, since this was what could be used for analysis in a future system. White Gaussian measurement noise and a distributed timing error over the array with a standard deviation of 160 ps were added to each simulation run to match reality as closely as possible.

Known but random timing errors were introduced into a number of elements to provide an error that could be analyzed. A number of different timing errors were tested to give a wider range of indication of the accuracy of the method.

To increase experimental robustness, the pointing of the array was randomized $\pm 10^\circ$. The signal structure described above was also randomly generated for each simulation, both in frequency and amplitude, so that every signal was unique. This was to simulate a real experiment where the changing ionosphere was measured, and to make sure that the results from the statistical analysis were not influenced by a signal correlation between simulations that would not exist in reality. Every simulation run was thus unique in every way, except for the introduced error, which was kept constant over the simulations. This enabled constant errors in the timing hardware to be tracked and detected.

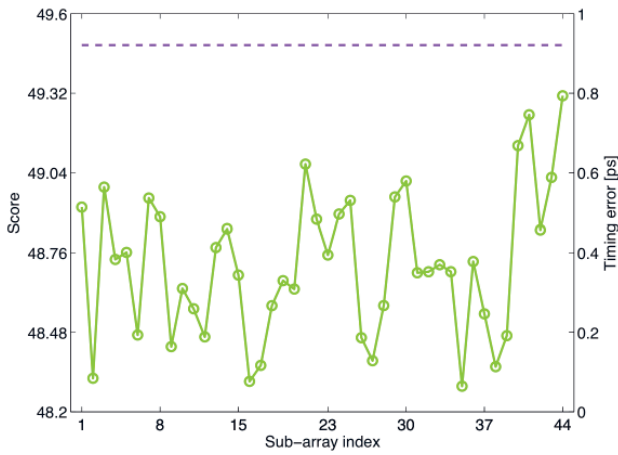


Figure 2. The mean value of the 20,000 data set principal-component score of a 2,112 element antenna divided into 44 subarrays, with no induced timing errors. The threshold is indicated with a dashed line.

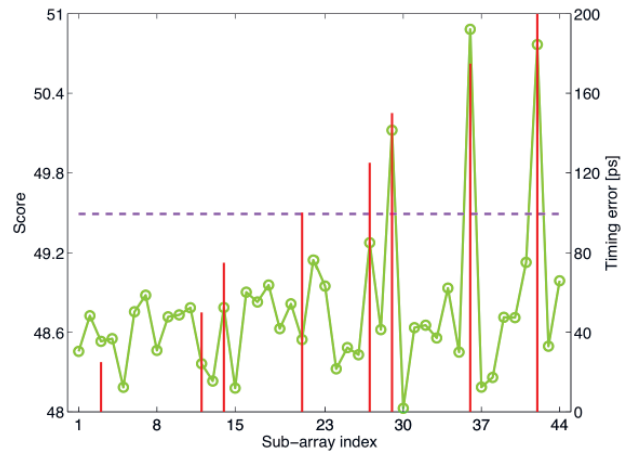


Figure 3. The mean value of the 20,000 data set principal-component score of a 2,112 element antenna divided into 44 subarrays, with induced timing errors from 25 to 200 ps in steps of 25 ps. The threshold is indicated with a dashed line, and the induced errors are shown in solid.

3. Results

To evaluate the performance of principal-component analysis for detecting timing errors, two main tests were performed. The first of these tested how small the errors were that could be detected with the method. The second tested how many faulty subarrays could be present in the array without the detector breaking down.

The first step was to analyze the case without any introduced errors to get a reasonable value for the threshold for detecting faulty subarrays. Figure 2 shows the mean value, \bar{y} , for each subarray of the first principal component score over $K = 20,000$ runs:

$$\bar{y} = \frac{1}{K} \sum_{k=1}^K |y_k|, \quad (3)$$

where the absolute value of the scores, $|y_k|$, was used. Using the absolute value was necessary since any subarray that stood out from the rest was to be detected, regardless of the sign. The result from Figure 2 and Equation 1 was used in conjunction with five different sets of measurements

# of Faulty Subarrays	Threshold
2%	$\mu_{\bar{y}} + 2.80\sigma_{\bar{y}}$
10%	$\mu_{\bar{y}} + 2.93\sigma_{\bar{y}}$
23%	$\mu_{\bar{y}} + 0.10\sigma_{\bar{y}}$
41%	$\mu_{\bar{y}} + 0.00\sigma_{\bar{y}}$
43%	$\mu_{\bar{y}} + 0.00\sigma_{\bar{y}}$

Table 1. The lowest possible threshold level with $P_{FA} = 0\%$ for five different levels of errors.

where the number of faulty elements was varied. The target of the threshold was to provide a simple detector capable of detecting small errors with a very low probability of false alarm (P_{FA}). To achieve this, the threshold was swept from $\gamma = \mu_{\bar{y}} + 6\sigma_{\bar{y}}$ to $\gamma = \mu_{\bar{y}}$ over the different measurements, and the minimum threshold possible with $P_{FA} = 0\%$ was calculated. The resulting thresholds are collected in Table 1. Since the largest of these approached $\gamma = \mu_{\bar{y}} + 3\sigma_{\bar{y}}$ and a margin was desirable, that threshold level was chosen for all consecutive simulations done in this paper.

As can be seen in Table 1, increasing the number of faulty subarrays in the analysis decreased the lowest possible threshold with $P_{FA} = 0\%$. This was because when the number of faulty subarrays increased, the number of correct subarrays decreased, causing the difference between errors and the correct part of the array to grow. A more-

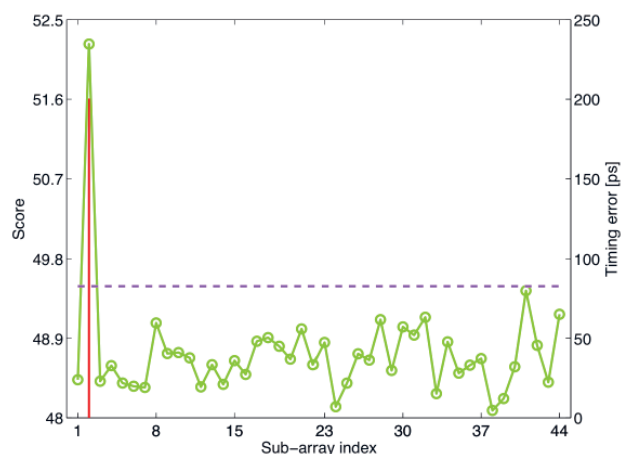


Figure 4. The mean value of the 20,000 data set principal-component score of a 2,112 element antenna divided into 44 subarrays, with 2% randomly induced timing errors. The threshold is indicated with a dashed line and the induced error is shown in solid. The single induced error was detected correctly for this setup.

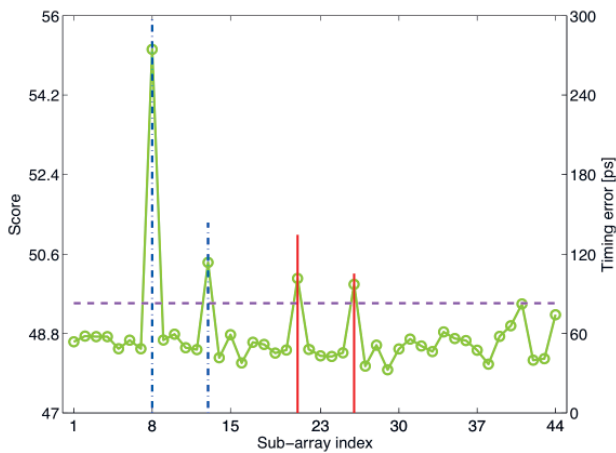


Figure 5. The mean value of the 20,000 data set principal-component score of a 2,112 element antenna divided into 44 subarrays, with 10% randomly induced timing errors. The threshold is indicated with a dashed line, and induced errors are shown in solid and dash-dot for positive and negative values, respectively. All four induced errors were detected without false alarms.

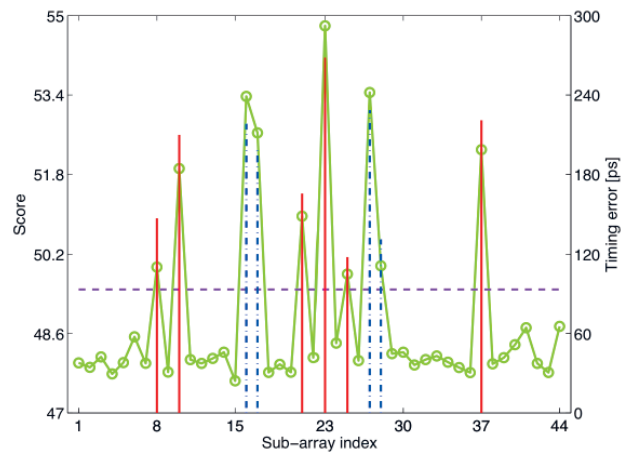


Figure 6. The mean value of the 20,000 data set principal-component score of a 2,112 element antenna divided into 44 subarrays, with 23% randomly induced timing errors. The threshold is indicated with a dashed line, and induced errors are shown in solid and dash-dot for positive and negative values, respectively. All ten errors were detected, again without any false alarms.

sophisticated threshold setting, deduced from each case, could therefore be preferred. However, since the goal of the method is to detect errors in the array at an early stage, it is likely that only a single or a few faulty subarrays are to be detected at one time. Thus, it was reasonable to use a fixed threshold based on the zero-error case.

3.1 Minimum Detectable Error

By inducing time errors with increasing size in different antennas in one simulation setup, an indication of the minimum detectable error with the method investigated could be found. Figure 3 shows the results from a setup where errors between 25 ps and 200 ps were induced at a step size of 25 ps. In this setup, 18% of the subarrays contained errors. The figure shows that errors down to 150 ps were clearly detectable with the method. With a more-sophisticated method of setting the threshold, even the 125 ps error would be detectable.

In a situation with only a single faulty subarray, the detector would probably be able to detect errors down to 100 ps (see Figure 4).

3.2 Multiple Number of Faulty Subarrays

To investigate how large a part of the array can be erroneous and have the detection capabilities maintained, a number of different setups were used. Each setup increased the number of induced errors in the array, and was then evaluated for missed and false detection. The position, size, and sign of the error was randomized for each setup. The results for a single faulty subarray are shown in Figure 4. The

induced error was about 200 ps, and was clearly detectable. Increasing the number of faulty subarrays to about 10%, Figure 5 still showed a 100% detection rate with no false alarms, even though one of the erroneous subarrays had a timing error of ~ 105 ps.

Even at 23% faulty subarrays the principal-component-score method did not fail, as can be seen in Figure 6. All errors were clearly detected, without false alarms. With this amount of faulty subarrays, the question arose as to whether there was a point in further pursuing this investigation. After all, a continuous monitoring system such as this is meant to be should alert the operator at the

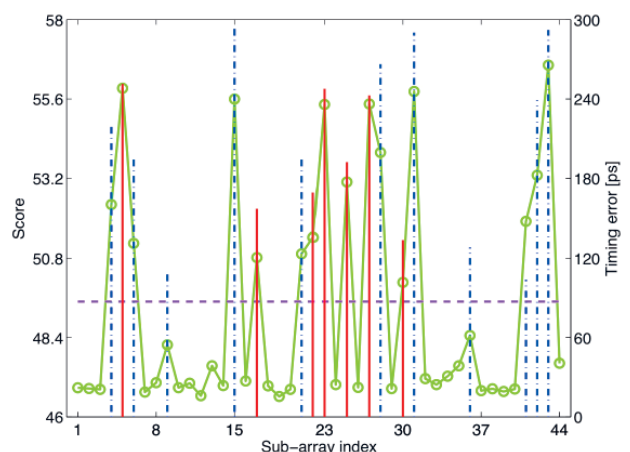


Figure 7. The mean value of the 20,000 data set principal-component score of a 2,112 element antenna divided into 44 subarrays, with 41% randomly induced timing errors. The threshold is indicated with a dashed line, and induced errors are shown in solid and dash-dot for positive and negative values, respectively. Two out of 18 faulty subarrays were not detected, but still without any false alarms.

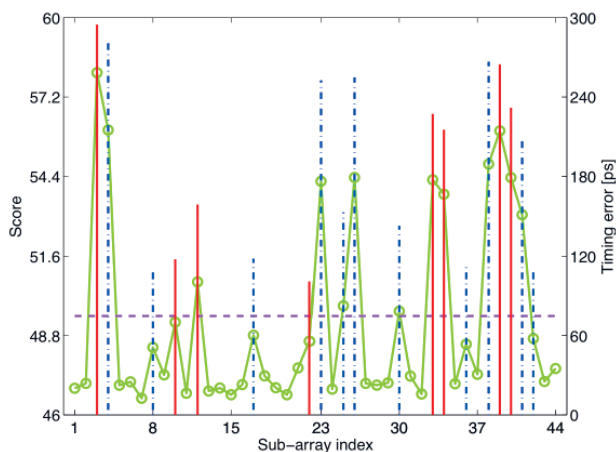


Figure 8. The mean value of the 20,000 data set principal-component score of a 2,112 element antenna divided into 44 subarrays, with 43% randomly induced timing errors. The threshold is indicated with a dashed line, and induced errors are shown in solid and dash-dot for positive and negative values, respectively. Six out of 19 faulty subarrays were not detected, without false alarms.

first faulty subarray, and thus trigger a repair of the faulty subarray, rather than continued operation. The probability that as much as 23% of the subarrays would have erroneous timing-hardware errors simultaneously is negligible. Regardless, for the completeness of the investigation, even more faulty subarrays were added.

At 41% faulty subarrays, the method started to miss-detect. As can be seen in Figure 7, two out of 18 faulty subarrays were not detected. However, the missed errors were all below 130 ps in amplitude, so the question was whether they were not detected because of their magnitude or because of the high number of faulty subarrays. The authors are convinced of the former, since when increasing the number of faulty subarrays to 43% (see Figure 8), the six out of 19 faulty subarrays that were not detected were again all below 130 ps. It thus seems likely that what sets the detectability of the faulty subarray is a tradeoff between the number of faulty subarrays and the magnitude of the errors. However, the simulations showed the algorithm to be more sensitive to the magnitude of the error.

4. Conclusions

The use of principal-component analysis to detect timing errors in a subarray of the EISCAT_3D radar is viable under certain circumstances. The magnitude of the errors has to be larger than ~ 120 ps, which is concurrent with the standard deviation of the acceptable timing error throughout

the array, and the ratio of faulty subarrays has to be below 20% of the subarrays in the radar. In these situations, the principal-component analysis method is capable of detecting 100% of the faults with a 0% false-alarm rate.

As a secondary timing-error detection system, the method described in this paper is easy and cheap to implement, as it only needs a small amount of computation time to work. It can be used to detect hardware errors foremost in the primary timing calibration system itself, as this might cause otherwise undetectable errors in the array.

5. Acknowledgments

The work presented in this paper was funded by the European Community under the “Structuring the European Research Area” Specific Programme Research Infrastructure action.

The EISCAT Scientific Association is supported by the Suomen Akatemia of Finland, the Chinese Institute of Radiowave propagation, the Deutsche Forschungsgemeinschaft of Germany, the National Institute for Polar Research of Japan, Norges Forskningsråd of Norway, Vetenskapsrådet of Sweden, and the Particle Physics and Astronomy Research Council of the United Kingdom.

6. References

1. A. K. Bhattacharyya, *Phased Array Antennas, Floquet Analysis, Synthesis, BFNs, and Active Array Systems*, New York, Wiley, 2006.
2. G. Wannberg, “EISCAT_3D Design Specification Document,” EISCAT Scientific Association, Tech. Rep., 2005, available at http://e7.eiscat.se/groups/EISCAT_3D%20info/P_S_D_7.pdf.
3. G. Stenberg, J. Borg, J. Johansson, and G. Wannberg, “Simulation of Post-ADC Digital Beam-Forming for Large Area Radar Receiver Arrays,” International RF and Microwave Conference, 2006.
4. P. Misra and P. Enge, *Global Positioning System, Signals, Measurements, and Performance, Second Edition*, Lincoln, MA, Ganga-Jamuna Press, 2006.
5. G. Johansson, “Large Aperture Array Radar Simulation Environment,” Luleå University of Technology, Technical Report, February 2009.
6. D. E. Johnson, *Applied Multivariate Methods for Data Analysts*, Duxbury Press, 1998.

Radio-Frequency Radiation Safety and Health



James C. Lin

Mobile-Phone Popularity, Addiction, and Funding for Biological Effects Research

The popularity of mobile phones remains very high. Worldwide, there are more people who own and use mobile phones than any other electronic gadgets, regardless whether it is in a rich or poor, developed or developing country. Mobile phones provide instant connectivity: whenever one wants to talk or conduct business transactions, regardless of where.

Mobile phones are convenient, increasingly more intuitive to operate, and come in hip, fanciful little packages with a growing range of extra features that deliver music, video, messaging, and Internet capabilities. No wonder both the young and old find them difficult to resist. They are playing major roles in everyday modern life. They have become necessities for work, family, safety, and a part of social networking. Ironically, health and safety issues often rise up to the top of the list in user surveys.

Children have them, and some grownups are hooked by them. Adolescents and young adults are obsessed with, and possibly addicted to, the mobile phone. Surveys have shown that adolescents and young adults spend more than an hour on the phone every day, on average. Many consider themselves to be heavy or very heavy users.

The question of whether the brains of children are more susceptible to the radio-frequency (RF) fields emitted by mobile phones than are those of adults remains open and controversial. This has led to concern about whether children might be at higher risk of mobile-phone use. Should a cautious approach of risk management be taken, especially in relation to children? Some fear any disturbance to brain activity in children could lead to impaired learning ability or behavioral problems. Moreover, any lasting effects could have important consequences, especially in the young, who still have years of development ahead of them. These questions cannot be easily answered, based on existing scientific knowledge.

Cellular mobile telephones are powerful wireless-communication devices. Their connectivity is enabled by the

antennas inside every mobile-phone handset, which emits electromagnetic fields in the microwave range of the radio frequency spectrum. In common usage, the handset is held next to the head, with about 50% of emitted electromagnetic energy absorbed by the head. For the first time in human history, a source of radio-frequency electromagnetic energy is thus located right next to the head of billions of mobile-phone users.

Scientific studies in the United States were initiated, mostly by mobile-phone manufactures and operators, in response to hearings in the US Congress when the suggestion of a connection between mobile phones and brain cancers was raised in 1993. A fair summary of the results would be that they did not conclusively demonstrate evidence that proves or disproves a health risk from mobile-phone electromagnetic fields. It is factual that more studies showed no health effect [1]. However, except for the animal studies, a majority of the studies were short-term investigations. That included epidemiological studies of head and neck cancers in mobile-phone users.

Epidemiological studies published to date on the use of a mobile phone for less than ten years showed no overall association between mobile-phone use and increased risk of malignant brain tumors. This was so with duration of use, years since first use, cumulative number of calls, and cumulative hours of use. However, brain tumors are known to have latencies of ten to fifteen years.

Long-term studies of biological and/or health effects on animals and humans exposed to mobile phones and other near-body wireless-communication electromagnetic fields still need to be done.

However, since the early 1990s, except for less than a handful of projects, support from US research funding or public-health-related governmental agencies has been nonexistent. Of late, even industry money for biological or health-effects research has dried up for some time in the US. Perhaps the declining economic environment may

James C. Lin is with the University of Illinois-Chicago, 851 South Morgan Street, M/C 154, Chicago, IL 60607-7053 USA; Tel: +1 (312) 413-1052 (direct); +1 (312) 996-3423 (main office); Fax: +1 (312) 996-6465; E-mail: lin@ece.uic.edu.

[A version of this item appeared in *IEEE Antennas and Propagation Magazine*, **52**, 2, April 2010, pp. 164-166; copyright ©2010 IEEE, used with permission.]

have played a role; but outsourcing of this research may be a contributing factor or a larger factor as well, especially outsourcing to Europe. It also may speak well of the US mobile-phone industry's eagerness in sponsoring biological-effects research outside the US borders, in other countries, under the banner of globalization.

Interestingly, concerns about biological effects and health implications have not quelled, if any, after years of outsourcing of mobile-phone-effects research to Europe. Public concerns for health and safety associated with mobile-phone electromagnetic fields have been on the rise in France and many other countries within the European Union.

Within the past year or so, both houses of the US Congress have expressed ostensible interest in the issue of cellular mobile telephones and induced tumors in users' heads. Dennis Kucinich, a US Congressman from Ohio and Chair of the Domestic Policy Oversight Subcommittee, conducted a hearing on mobile phones in September 2008. More recently, in September 2009, Tom Harkin, a US Senator from Iowa, chaired a hearing of the Subcommittee on Labor, Health, and Human Service and Education and Related Agencies on "Health Effects of Cell Phones." Apparently, the hearing was convened through encouragement from Senator Arlen Specter of Pennsylvania. Nevertheless, by all accounts, the meetings were standing-room only.

The observation of a research focus shifting away from the US has been made especially poignant by the list of witnesses at these hearings. Both hearings received fairly widespread coverage in the media. It was reported after the most-recent hearing that the Senators present found "this really very interesting and very challenging," and assured the participants that they are "going to do some follow-up on this." Nevertheless, one would be well advised not to read too much into these pronouncements made immediately following the Congressional hearings, in terms of funding for research or interest from the US research-funding or public-health-related governmental agencies.

Simply put, the view has been "people are not dropping off like flies as a consequence of mobile-phone use!" In the meantime, adolescents and young adults have become heavy and, indeed, very heavy mobile-phone users.

Several studies have found that some adolescents exhibit an unhealthy dependence on mobile phones, conveying more depressive symptoms, higher interpersonal anxiety, and lower self esteem [2-4]. For example, among obsessed young mobile-phone users, tendencies to identify themselves with their mobile phones and to have difficulties in controlling their usage have been reported. The degree and pattern of attachment to mobile phones show classic symptoms of behavioral addiction. Some of the symptoms of obsessive mobile phone use among 1,665 frequent users tested included the following: 1,122 adolescents needed a marked increase in the frequency and duration to achieve satisfaction; 1,273 subjects showed withdrawal symptoms;

1,136 used mobile phones for a period of time longer or more frequently than intended; 898 experienced persistent desire and/or unsuccessful attempts to cut down use; and 969 spent an excessive amount of time on mobile phones [2]. About half of the adolescents in this study reported having symptoms of obsessive mobile phone use, and had reported functional impairment caused by it. Indeed, the study suggested that obsessive mobile phone use can compromise relationships with friends or classmates.

Similar obsessive, problematic, or excessive mobile-phone use and functional impairment in adolescents have been observed worldwide [2-6]. Symptoms of tolerance, withdrawal, craving, and loss of control over mobile-phone use were deemed to be akin to behavioral addiction or substance-use dependence. Indeed, a positive correlation was observed between obsessive mobile-phone use and Internet addiction [3]. (Excessive use of the Internet can lead to a mental disorder of the addictive type [7, 8]).

A study investigating addictive patterns of mobile-phone use among youth concluded that adolescents and young adults' obsessive use of mobile phones may be considered abusive, but not addictive, since their use does not lead to rapid changes in emotion [7]. It is interesting to note that the same research group found that males displayed more addictive use of the Internet, while females seems to use the mobile phone more as a means for emotional communication [8].

References

1. J. C. Lin (ed.), *Advances in Electromagnetic Fields in Living Systems, Volume 5*, New York, Springer, 2009.
2. C. F. Yen T. C. Tang, J. Y. Yen, H. C. Lin, C. F. Huang, S. C. Liu, and C. H. Ko, "Symptoms of Problematic Cellular Phone Use, Functional Impairment and its Association with Depression Among Adolescents in Southern Taiwan," *J. Adolescent*, **32**, 2009, pp. 863-873.
3. J. H. Ha, B. Chin, D. H. Park, S. H. Ryu, and J. Yu, "Characteristics of Excessive Cellular Phone Use in Korean Adolescents," *Cyberpsychol. Behav.*, **11**, 2008, pp. 783-784.
4. S. P. Walsh, K. M. White, and R. M. Young, "Over-Connected? A Qualitative Exploration of the Relationship Between Australian Youth and their Mobile Phones," *J. Adolescent*, **31**, 2008, pp. 77-92.
5. N. Kawasaki, S. Tanei, F. Ogata, S. Burapadaja, C. Loetkham, and T. Nakamura, "Survey on Cellular Phone Usage on Students in Thailand," *Journal of Physiological Anthropology*, **25**, 2006, pp. 377-382.
6. A. Bianchi and J. G. Phillips, "Psychological Predictors of Problem Mobile Phone Use," *Cyberpsychology & Behavior*, **8**, 2005, pp. 39-51.
7. X. Sanchez-Carbonell, M. Beranuy, M. Castellana, A. Chamarro, and U. Oberst "Internet and Cell Phone Addiction: Passing Fad or Disorder?," *Adicciones*, **20**, 2008, pp. 149-159.
8. M. Beranuy Fargues, A. Chamarro Lusar, C. Graner Jordania and X. Carbonell Sánchez "Validation of Two Brief Scales for Internet Addiction and Mobile Phone Problem Use," *Psicothema* **21**, 2009, pp. 480-485.



CONFERENCE ANNOUNCEMENT

ISAP 2011

Lotte Hotel Jeju, Korea, October 25-28, 2011

The 2011 International Symposium on Antennas and Propagation (ISAP2011) will be held at the Lotte Hotel Jeju, Korea, during October 25~28, 2011. This symposium is sponsored and organized by the Korea Electromagnetic Engineering Society (KEES) and cosponsored by the Communications Society of the Institute of Electronics, Information and Communication Engineers (IEICE). This symposium is held under the technical co-sponsorship of the Antennas and Propagation Society of the Institute of Electrical and Electronics Engineers (IEEE/AP-S) and the International Union of Radio Science (URSI).

Objective

ISAP2011 is intended to provide an international forum for exchanging information on the progress of research and development in antennas, propagation, electromagnetic wave theory, and related fields, as shown in the Scope. An important objective of this meeting is to promote mutual interaction among participants.

Topics

This symposium will cover a wide range of topics on antennas, propagation, electromagnetic wave theory, and wireless application systems, as suggested below. Papers concerned with other related topics will also be considered.

A. Antennas and Related Topics

- A1 Microstrip and Printed Antennas
- A2. Active and Integrated Antennas
- A3. Array Antennas, Phased Arrays and Feeding Circuits
- A4. Small Antennas
- A5. Adaptive and Smart Antennas
- A6. Multiband/wideband Antennas
- A7. Slot Antennas
- A8. Millimeter Wave and Sub-Millimeter Wave Antennas
- A9. Reflector/Lens Antennas and Feeds
- A10. Optical Technology in Antennas
- A11. Mobile and Base Station Antennas
- A12. Antenna Measurements
- A13. Others

B. Propagation and Related Topics

- B1. Mobile and Indoor Propagation
- B2. Mobile Channel Characterization and Modeling
- B3. Millimeter and Optical Wave Propagation
- B4. Earth-Space and Terrestrial Propagation
- B5. Radio Astronomy
- B6. Remote Sensing
- B7. SAR Polarimetry and Interferometry
- B8. Ionospheric Propagation
- B9. Others

C. Electromagnetic Wave Theory

- C1. Complex Media and Artificial Media
- C2. Computational Electromagnetics
- C3. Theoretical Electromagnetics and Analytical Methods
- C4. High-Frequency Techniques
- C5. Inverse Problems
- C6. Random Media and Rough Surfaces
- C7. Scattering and Diffraction
- C8. Waveguiding Structures
- C9. Periodic and Band-Gap Structures
- C10. Time Domain Techniques
- C11. Others

D. Systems and Other Related Topics

- D1. High Power Microwave Applications
- D2. Advanced Materials for EM Applications
- D3. UWB and Impulse Radio
- D4. Ubiquitous Network Systems
- D5. Satellite Communication Systems
- D6. Radio Technologies for Intelligent Transport Systems
- D7. Subsurface Sensing (D8) EMC/EMI Simulations and Measurements (D9) Others

E. Emerging / Special Topics

- E1. Wireless Energy Transmission
- E2. Terahertz Photoconductive Antenna
- E3. Nano Antenna
- E4. MIMO Antenna
- E5. Meta Material and Applications
- E6. Biological Effects and Medical Applications
- E7. Basic Measurement Technology in RF and Microwave

Important Dates

Paper Submission Deadline: May 15, 2011
Acceptance Notification: July 15, 2011
Camera-Ready Manuscript: August 15, 2011
Advance Registration: August 15, 2011

Contact

ISAP 2011 Secretariat
5F. Daehan Bldg., #1018 Dunsan-Dong, Seo-Gu,
Daejeon 302-120, Korea
Tel : +82-42-472-7458
Fax : +82-42-472-7459
E-mail : isap2011@isap2011.org
Web : www.isap2011.org

URSI CONFERENCE CALENDAR

June 2010

CROWNCOM - 5th Int. Conference on Cognitive Radio Oriented Wireless Networks and Communications

Cannes, France, 16-18 June 2010

Contact : Jacques Palicot, SUPELEC, Avenue de la Bulaie, 53576 Cesson-Sévigné, France, Fax +33 299-844599, E-mail: jacques.palicot at supelec.fr

OCOSS 2010 - Ocean and Coastal Observation: sensors and observing systems, numerical models and information systems

Brest, France, 21-23 June 2010

Contact: jisnard-isti at club-internet.fr

MSMW 2010

Kharkov, Ukraine, 21-26 June 2010

Contact : Alexei Kostenko, IRE NASU, ul. Proskura 12, Kharkov 61085, Ukraine, Fax: +380(57)3152105, E-mail:kostenko at ire.kharkov.ua

July 2010

SCOSTEP - STP12

Berlin, Germany, 12-16 July 2010

Contact: Prof. Dr. Franz-Josef Lübken, Leibniz Institute of Atmospheric Physics, Schloss-Strasse 6, 18225 Kühlungsborn, Germany, Fax: +49-38293-6850, E-Mail: luebken@iap-kborn.de, <http://www.iap-kborn.de/SCOSTEP2010/>

COSPAR 2010 - 38th Scientific Assembly of the Committee on Space Research (COSPAR) and Associated Events

Bremen, Germany, 18 - 25 July 2010

cf. Announcement in the Radio Science Bulletin of December 2008, p. 73.

Contact: COSPAR Secretariat, c/o CNES, 2 place Maurice Quentin, 75039 Paris Cedex 01, France, Fax: +33 1 44 76 74 37, E-mail: cospar@cosparhq.cnes.fr, Web: <http://www.cospar2010.org/> or <http://www.cospar-assembly.org>

East, Central and Southern African Regional GNSS and Space Weather Workshop

Nairobi, Kenya, 19-23 July 2010

Contact: Prof. P. Baki, University of Nairobi, Kenya, pbaki@uonbi.ac.ke, paulbaki@gmail.com, castrajoseph@yahoo.com

August 2010

EMTS 2010 - International Symposium on Electromagnetic Theory (Commission B Open Symposium)

Berlin, Germany, 16-19 August 2010

Contact: EMTS 2010, Prof. Karl J. Langenberg, Universität Kassel, D-34109 Kassel, Germany, E-mail: info@emts2010.de, Web: <http://www.emts2010.de>

Nordic Shortwave Conference HF10 and Longwave Symposium LW10

Farö, North of the Island of Gotland in the Baltic, 17-19 August 2010

Contact : Saab Aerotech, Nobymalmsvägen, SE- 58182 Linköping, Sweden, Phone : +46 13 23 13 21, Fax : +46 13 29 92 35, E-mail : margareta.samuelsson@saabgroup.com, Web : <http://www.nordichf.org>

3rd International Communications in Underground and Confined Areas

Val d'Or, Québec, Canada, 23-25 August 2010

Contact: Paule Authier, Secrétaire, LRTCS-UQAT, Laboratoire de recherche Télébec en communications souterraines de l'UQAT, 450, 3e Avenue, local 103, Val-d'Or, Québec J9P 1S2, Fax: (1)(819) 874-7166, E-mail: lrcs@uqat.ca, Web: <http://www.icwcuca.ca/welcome.asp>

ISRSSP'10 - 2nd International Symposium on Radio Systems and Space Plasma

Sofia, Bulgaria, 25-27 August 2010

Contact : E-mail: Blagovest Shishkov - bshishkov at math.bas.bg, Web: <http://www.isrssp.org>
cf. Announcement in the Radio Science Bulletin of December 2009, p.33-34 .

September 2010

ISTC2010 - International Symposium on Turbo Codes *Brest, France, 6-10 September 2010*

cf. Announcement in the Radio Science Bulletin of December 2009, p. 34-36.

Contact: Télécom Bretagne, International Symposium on Turbo Codes, Département: Électronique, Technopôle Brest Iroise, CS83818, 29238 BREST Cedex, FRANCE, Tel: +33 2 98 00 10 28, Fax : +33 2 98 00 11 84, Email : istic at mlistes.telecom-bretagne.eu, Web: <http://conferences.telecom-bretagne.eu/turbocodes/>

CAOL 2010 – International conference on Advanced Optoelectronics and Lasers

Sevastopol, Ukraine, 10-14 September 2010

Contact: <http://caol.kture.kharkov.ua/>

VERSIM Workshop

Prague, Czech Republic, 13-17 September 2010

Contact: E-mail: versim@ufa.cas.cz, 10 Web: <http://physics.mff.cuni.cz/kfpp/versim10/>

Metamaterials 2010 - The Fourth International Congress on Advanced Electromagnetic Materials in Microwaves and Optics

Karlsruhe, Germany, 13-16 September 2010

Contact : Web: <http://congress2010.metamorphose-vi.org/>

ISSSE 2010 - International Symposium on Signals Systems and Electronics

Nanjing, China, 16-19 September 2010

Contact: Guangqi Yang, State Key Lab of Millimeter Waves, School of Information Science and Engineering, Southeast University, Nanjing, 210096, China, Tel: +86 (25) 8379 4364, Fax: +86 (25) 8379 2096, E-mail: issse2010@emfield.org, Web: <http://www.emfield.org/issse2010>

ICEAA 2010 - International Conference on Electromagnetics in Advanced Applications

Sydney, Australia, 20-24 September 2010

cf. Announcement in the Radio Science Bulletin of September 2009, p. 62-63.

E-mail: Roberto.Graglia@polito.it, Web: <http://www.iceaa-offshore.org/>

AP-RASC - 2010 Asia-Pacific Radio Science Conference *Toyama, Japan, 22-26 September 2010*

cf. Announcement in the Radio Science Bulletin of December 2009, p. 6-8.

Contact: Prof. K. Kobayashi, Vice President for International Affairs, Chuo University, 1-13-27 Kasuga, Bunkyo-ku, Tokyo 112-8551, JAPAN, Fax: +81-3-3817-1847, E-mail: kazuya@tamacc.chuo-u.ac.jp

October 2010

Commission F Microwave Signatures Symposium

Florence, Italy, 4-8 October 2010

Contact: Prof. P. Pampaloni, IFAC/CNR, Florence, Italy, Fax +390 555 226434, E-mail: p.pampaloni@ifac.cnr.it

December 2010

APCM 2010 - 2010 Asia-Pacific Microwave Conference

Yokohama, Japan, 7-10 December 2010

Contact: Prof. Kiyomichi Araki, Chair, Steering Committee, c/o Real Communications Corp., 3F Shinmatsudo, Matsudo 270-0034, Japan, Tel. +81 47-309-3616, Fax +81 47-309-3617, E-mai: nweapmc@io.ocn.ne.jp, Web: www.apmc2010.org

April 2011

CEM 2011 - Eight International Conference on Computation in Electromagnetics

Wroclaw, Poland, 11-14 April 2011

Contact: Prof. Jan K. Sykulski, Chairman of CEM 2011, Electrical Power Engineering Research Group, School of Electronics and Computer Science, University of Southampton, Southampton, SO17 1BJ United Kingdom, Fax +44 23-8059 3709, E-mail: jks@soton.ac.uk, Web: <http://www.cem2011.com>

JURSE 2011 - Joint Urban Remote Sensing Event 2011 (formerly URBAN)

Munich, Germany, 11-13 April 2011

Contact: Photogrammetry & Remote Sensing, Technische Universitaet Muenchen, Arcisstr. 21, D-80333 München, Germany, Fax: +49 89 2809573, E-mail: pf@bv.tum.de, Web: <http://www.pf.bv.tum.de/jurse2011/>

October 2011

ISAP2011 - 2011 International Symposium on Antennas and Propagation

Jeju, Japan, 25-28 October 2011

cf. Announcement in the Radio Science Bulletin of June 2010, p. 53-54.

Contact: 5F Daehan Bldg., #1018 Dunsan-Dong, Seo-Gu, Daejeon 302-120, Korea, Tel : +82-42-472-7463, Fax : +82-42-472-7459, isap@isap2011.org, <http://www.isap2011.org>

An up-to-date version of this Conference Calendar, with links to various conference web sites can be found at www.ursi.org/Calendar of supported meetings

URSI cannot be held responsible for any errors contained in this list of meetings.



BOOKS PUBLISHED FOR URSI RADIOSCIENTISTS

Electromagnetic and Optical Pulse Propagation 2: Temporal Pulse Dynamics in Dispersive, Attenuative Media

(Springer Series in Optical Sciences, Vol. 144)

by Kurt E. Oughstun, Berlin, Springer, 2009, Hardcover ISBN: 978-1-4419-0148-4; 831 pp.; 350 Illus.; USD 199.00

This book is the second volume of a two-volume set on *Electromagnetic and Optical Pulse Propagation*, authored by Prof. Oughstun. It presents a systematic treatment of the radiation and propagation of transient electromagnetic and optical wave fields. Such fields are used in ultra-wideband radar and communication systems, as well as in ultra-short pulsed optics. The radiation and propagation is through causal, locally linear media that exhibit both temporal dispersion and absorption. Media such as those that are dielectric, conducting, and semiconducting are considered. Applications are for bioelectromagnetics, remote sensing, ground- and foliage-penetrating radar, and undersea communications.

The first chapter of this book, Chapter 9, is entitled “Pulsed Electromagnetic and Optical Beam Wave Fields in Temporally Dispersive Media.” It starts with the governing equation of macroscopic electromagnetic fields in homogeneous, isotropic, locally linear (HILL), temporally dispersive media, and without any external sources. As in Volume 1, throughout the book the analysis can be interpreted in both in cgs and in MKS units by omitting a possible pre-factor written in double brackets. This is an interesting feature, which is on one side helpful, and on another side makes the equations longer.

The following Chapter 10 treats asymptotic methods of analysis using advanced saddle-point techniques. For instance, it discusses Olver’s saddle-point method, which is an important alternative to the method of steepest descent.

The concept of group-velocity approximation is discussed in Chapter 11. One focus of the chapter is the extension of the classical concept to lossy dispersive materials. This is the case if the spectrum of an ultra-wideband pulse spans at least one critical feature in the dispersion relation.

Chapter 12 provides the analysis of the phase function and its saddle points for (causal) temporally dispersive media that are homogeneous, isotropic, and locally linear. For

instance, the phase function of a single-resonance Lorentz-model dielectric exhibits four branch points and four saddle points. Beside the aforementioned single-resonance model, this chapter discusses the phase function and its saddle points for multiple-resonance Lorentz, Rocard-Powles-Debye, Drude, and semiconductor models.

The very interesting feature of the evolution of the precursor fields is addressed in the following Chapter 13. The analysis is based on Chapters 10 and 12. Accurate asymptotic approximations of the precursor fields are given for Lorentz- and Debye-type dielectrics, as well as for Drude model conductors and semiconductors. As a benefit of the analysis, each feature appearing in the propagated wave field may be traced back to the behavior of a particular saddle point (or points), together with their interaction with any pole singularity of the initial pulse’s envelope spectrum.

Chapter 14 analyzes the contribution of the field component – which is associated with any long-term signal that is being propagated through the dispersive material – to the asymptotic behavior of the propagated wave field. For the analysis, the direct application of Olver’s method and the Cauchy residue theorem applied in the nonuniform asymptotic analysis, and the utilization of the uniform asymptotic expansion technique by Bleistein, Felsen, and Marcuvitz, and the extension by Cartwright, are applied.

The continuous evolution of the total field is part of Chapter 15. Here, the results of the preceding two chapters are combined to derive the uniform asymptotic description of the total pulsed wave-field evolution in a causally dispersive material. At the end of this chapter, the *myth of superluminal pulse propagation* is addressed.

Physical interpretations of dispersive pulse dynamics in causal, dispersive absorptive materials are given in Chapter 16. The chapter begins with a detailed derivation of the energy velocity description of dispersive pulse dynamics, followed by a reformulation of the classical group velocity concept through a direct, unaltered application of

the asymptotic method of stationary phase. A signal analysis of dispersive pulse propagation due to Stratton, recently updated by Banks, is discussed at the end of this chapter.

An overview of applications is presented in the last chapter, Chapter 17. It addresses the application of precursor waveforms, electromagnetic energy dissipation in causally dispersive media, reflection and transmission phenomena (e.g., the Goos-Hänchen shift), and optical pulse penetration through dispersive bodies (e.g., ground- and foliage-penetrating radar and undersea communications). Finally, the health and safety issues associated with electromagnetic ultra-short pulsed radiation are addressed.

The appendix of this book covers details of the asymptotic expansion of single integrals. It also presents a proof of the theorem by Shermans, Stammes, and Lalor on the asymptotic approximations to angular-spectrum representations, and the Radon transform.

Each chapter includes a set of challenging problems and a list of references. Some chapters provide at the end a summary of the discussed analysis, as well.

In summary, the second volume of the two-volume set on *Electromagnetic and Optical Pulse Propagation* is a very impressive book. It is highly recommended for graduate students, researchers, physicists, and engineers who are working in the field of electromagnetic wave propagation, antennas, microwaves, photonics, and optoelectronics.

Review by:

René Marklein
University of Kassel
Dept. of Electrical Engineering and Computer Science
D-34109 Kassel, Germany
Tel: +49 561 804 6426; Fax: +49 561 804 6489
E-mail: marklein@uni-kassel.de or marklein@ieee.org

Electromagnetic Fields, Second Edition

by Jean Van Bladel, New York, IEEE Press, Wiley-Interscience, 2007, pp. XIV+1155, ISBN 978-0-471-26388-3

The first edition of Prof. Van Bladel's *Electromagnetic Fields* was published by Mc-Graw Hill in 1964. It was quickly sold out, to be reprinted only much later, in 1985, by Hemisphere. This reviewer is one of the lucky persons in possession of an original copy of the first edition, which over many years he found invaluable as a reference.

In 2007, the IEEE Press published a second and much expanded edition of *Electromagnetic Fields*. This took the author a decade to prepare, but turned out to be worth waiting for. This second edition is about three times the size of the original version, with a much-expanded and updated bibliography and set of appendixes. It consists of seventeen chapters, each with its own bibliography and with a set of problems that make this book well suited not only as a reference source, but also as a textbook for advanced courses in electromagnetism.

The first two chapters are devoted to mathematical preliminaries on linear analysis and variational techniques. Even though the style is concise, the reader is exposed to a good overview of topics such as linear transformations, dyadics, eigenfunction expansions, functionals, discretization, finite elements, and stability and solution of matrix equations. The next four chapters cover electrostatic fields in the presence of conductors and dielectrics, special geometries for electrostatic field problems, and magnetostatic fields. The presentation involves analytical as well as numerical (integral equations, finite elements) techniques.

Chapter 7 deals with radiation in free space, and briefly covers a hodge-podge of topics, such as the wave equation,

potentials, polarization, radiation patterns, multipole expansions, spherical harmonics, equivalent sources, and wire antennas. Chapter 8 discusses radiation in material media; constitutive relations are examined, even though in a less-systematic way than this reviewer would have liked. Other topics briefly covered include ray and beam propagation, dyadics, reciprocity, the equivalent circuit and effective area of antennas.

Propagation through multilayered planar structures, periodic structures, and apertures are studied in Chapter 9, where the Sommerfeld dipole problem and edge diffraction are also examined. Resonators, both closed and open, are covered in Chapter 10.

The next three chapters are concerned with general problems in scattering theory. Basic concepts and examples are expounded in Chapter 11, beginning with the scattering matrix and the definitions of cross sections. This is followed by the particular case of scattering by a sphere, resonant scattering, the singularity expansion method, impedance boundary conditions, thin layers, and characteristic modes. Chapter 12 is a good introduction to the main numerical concepts and methods employed in scattering theory: integral equations, T-matrix, absorbing boundary conditions, finite elements, and finite differences. In Chapter 13, an overview is provided of approximate analytical techniques at high and low frequencies.

Chapter 14 illustrates approaches and results for some two-dimensional scattering problems, notably circular cylinders, elliptic cylinders, and wedges. The theory of

propagation in metallic and dielectric waveguides is covered in Chapter 15. Scattering by rotationally symmetric bodies, with particular attention to conical structures, is the subject of Chapter 16. Finally, the electrodynamics of moving bodies in the framework of the special theory of relativity is expertly dealt with in Chapter 17.

The rich appendixes at the end of the book cover several important topics: vector analysis in two and three dimensions, coordinate systems, dyadic analysis, special functions, eigenfunctions and eigenvectors, complex integration, linear transforms, and distributions. The volume concludes with a good bibliography, and author and subject indexes.

From the previous paragraphs, the reader may already have concluded that this book attempts to cover an enormous amount of material in a single volume. As a consequence, it is unavoidable that some topics are only briefly touched upon, akin to what would happen in an encyclopedia entry.

The bibliographical references are exemplary rather than comprehensive, but give the interested reader a good starting point to finding additional relevant material. It appears that the book is remarkably free of misprints and errors. This reviewer would have preferred to see the vector notation of Gibbs, based on the “del” or “nabla” operator, adopted, instead of the old European notation of grad, div, and curl. However, this is a small peccadillo in an otherwise masterful work that will constitute an invaluable reference book for decades to come.

Reviewed by:

Piergiorgio L. E. Uslenghi
University of Illinois at Chicago
E-mail: uslenghi@uic.edu

[This review also appeared in *IEEE Antennas and Propagation Magazine*, **52**, 2, April 2010, p. 117; copyright ©2010 IEEE, used with permission.]

Essentials of Cognitive Radio

by Linda E. Doyle, Cambridge, Cambridge University Press, ISBN-13: 9780521897709, 250 pp

This overall book is written around the cognitive cycle: *observe-decide-act*. It seems a very reasonable choice for a concise and practical guide on cognitive radio. The overall description is very intuitive (with interesting analogies, for example, the umbrella in Chapter 2). It requires no particular knowledge (or mathematical skills) to understand the notions developed in the book. This makes the book very easy to understand, and, thus, accessible to a large public.

In Chapter 1, the author introduces the cognitive radio world. She highlights the fact that the evolution is to put more and more intelligence everywhere. This is also the case for wireless networks. From this point of view, cognitive radio is coherent with this evolution. The second part of the chapter deals with spectrum management. Problems of fixed allocation and under usage in these allocated bands of the spectrum are described. Different possibilities for using the spectrum (overlay, underlay techniques) are also presented. I only regret that the chapter is too much spectrum-management oriented, and that there is no discussion from the context-aware point of view, and the point of view of upper layers.

Starting from the umbrella analogy, the second chapter illustrates the difficult task of making a decision (even if it is so simple as, “Should I take my umbrella?”). The decision depends on observation, on rules, on experience, etc. This analogy permits introducing the cognitive cycle: *observe-decide-act*. At the end of the chapter, the author maps all the chapters of the book onto a scheme: in this way, overall coherency of the book is clearly demonstrated.

The subsequent three chapters describe the three functions of the cycle.

Chapter 3 deals with the taking-action function. It is clear that prior to acting, it is necessary to identify which actions are possible. The first part of the chapter, from different points of view (transmitter, channel, receiver, spectrum) identifies the possible actions and their consequences, mainly from an interference point of view. It is in this chapter that some technological aspects, such as modulation, access, and waveforms, are presented. Again, taking action from an upper-layer perspective is not sufficiently discussed.

To sense – to observe the outside world – is, of course, essential for taking actions. The purpose of Chapter 4 is exactly to describe sensors. This chapter mainly focuses on spectrum sensing. Therefore, the author reminds the reader of the classical ways to identify holes and white spaces in the spectrum, both from the cooperative and non-cooperative points of view.

The following chapter, Chapter 5, describes the decision-making process. The author stresses the fact that the decision-making process leads mainly to an optimization problem. However, since the equipment can face various environments, the optimization process might be difficult to handle, especially when the decision-making engine deals with multi-criteria problems.

Making the space of solutions hard to explore, and justifying the use of various techniques of optimization (such as deterministic algorithms, heuristics, or meta-heuristic algorithms) to mitigate these difficulties is discussed. Moreover, the decision-making problem can become even more complex when several pieces of equipment have to “share” the same environment, and have to share the

same resources. Within this context, the author explains that many approaches exist to tackle these problems, such as graph theory or game theory, leading in some cases to interesting results (Nash equilibrium, for instance, in the case of game theory).

To make appropriate decisions, the equipment has to “understand” the observed information about the environment. The knowledge-representation issue appears as a key problem, and the reasoning techniques appear as a cognitive-radio enabler. The author constraints her presentations of the possible reasoning techniques to the “rule-based” approach, as well as the “case-based” approach. Once again, these described approaches are the mostly used and very intuitive, leading to an easy introduction to the reasoning issue to a large public.

The author completes the reasoning techniques introduced by a discussion of the benefits of a learning process. If in some cases the learning task seems an added process that can improve the overall performance of a complex decision-making engine, in some other cases learning becomes crucial, especially when unexpected scenarios occur. In general, the author suggests the learning techniques to deal with the decision-making problem itself, or to learn selecting the most-appropriate optimization technique among the available techniques, depending on the context. Unfortunately, when it comes to learning techniques, this chapter only focuses on pattern-recognition techniques, where machine-learning or artificial-intelligence approaches are suggested as general approaches.

Chapter 6 deals with security problems. This is in fact very important, because with software-radio and cognitive-radio techniques, new windows are opened and classical security challenges of wireless communications are increased. This chapter is short, because there has not been a lot of work done on this subject, but, in my opinion, it is a very important chapter of the book.

The cognitive-radio platforms are described in Chapter 7. The reader is reminded of the running platform with the classical constraint on flexibility and performance. DSP, ASIC, and FPGA are presented. The author takes into account the consumption constraints, which are very important these days from a green-communications point of view. The analog part, with its own difficulties (mainly, nonlinearity), is also described in this chapter. In this chapter, the link with software-radio technology is missing, from my point of view.

The last chapter (Chapter 8) of this book deals with regulation and standardization. The main focus of this chapter is to give a simple and short overview of the most important concepts of regulation, and also of the main international groups involved in cognitive-radio standardization.

In conclusion, the author said that cognitive radio crosses many scientific fields. I fully agree with that. Even though I know that in a short book it is impossible to deal with all the aspects of the problem, one important aspect is missing. This is the management of such complex systems. I mean management of both the (re)configuration platform and the cognitive cycle. The description of these techniques is very light, which can suit a beginner, but can seem “frustrating” for a more-advanced public.

As a practical guide on cognitive radio, this book completely fulfills its objective and is very useful for quickly entering into the domain.

Reviewed by

Jacques Palicot
SUPELEC/IETR
Rennes, France

E-mail: Jacques.palicot@supelec.fr

Information for authors



Content

The *Radio Science Bulletin* is published four times per year by the Radio Science Press on behalf of URSI, the International Union of Radio Science. The content of the *Bulletin* falls into three categories: peer-reviewed scientific papers, correspondence items (short technical notes, letters to the editor, reports on meetings, and reviews), and general and administrative information issued by the URSI Secretariat. Scientific papers may be invited (such as papers in the *Reviews of Radio Science* series, from the Commissions of URSI) or contributed. Papers may include original contributions, but should preferably also be of a sufficiently tutorial or review nature to be of interest to a wide range of radio scientists. The *Radio Science Bulletin* is indexed and abstracted by INSPEC.

Scientific papers are subjected to peer review. The content should be original and should not duplicate information or material that has been previously published (if use is made of previously published material, this must be identified to the Editor at the time of submission). Submission of a manuscript constitutes an implicit statement by the author(s) that it has not been submitted, accepted for publication, published, or copyrighted elsewhere, unless stated differently by the author(s) at time of submission. Accepted material will not be returned unless requested by the author(s) at time of submission.

Submissions

Material submitted for publication in the scientific section of the *Bulletin* should be addressed to the Editor, whereas administrative material is handled directly with the Secretariat. Submission in electronic format according to the instructions below is preferred. There are typically no page charges for contributions following the guidelines. No free reprints are provided.

Style and Format

There are no set limits on the length of papers, but they typically range from three to 15 published pages including figures. The official languages of URSI are French and English: contributions in either language are acceptable. No specific style for the manuscript is required as the final layout of the material is done by the URSI Secretariat. Manuscripts should generally be prepared in one column for printing on one side of the paper, with as little use of automatic formatting features of word processors as possible. A complete style guide for the *Reviews of Radio Science* can be downloaded from <http://www.ips.gov.au/IPSHosted/NCRS/reviews/>. The style instructions in this can be followed for all other *Bulletin* contributions, as well. The name, affiliation, address, telephone and fax numbers, and e-mail address for all authors must be included with

All papers accepted for publication are subject to editing to provide uniformity of style and clarity of language. The publication schedule does not usually permit providing galleys to the author.

Figure captions should be on a separate page in proper style; see the above guide or any issue for examples. All lettering on figures must be of sufficient size to be at least 9 pt in size after reduction to column width. Each illustration should be identified on the back or at the bottom of the sheet with the figure number and name of author(s). If possible, the figures should also be provided in electronic format. TIF is preferred, although other formats are possible as well: please contact the Editor. Electronic versions of figures *must* be of sufficient resolution to permit good quality in print. As a rough guideline, when sized to column width, line art should have a minimum resolution of 300 dpi; color photographs should have a minimum resolution of 150 dpi with a color depth of 24 bits. 72 dpi images intended for the Web are generally *not* acceptable. Contact the Editor for further information.

Electronic Submission

A version of Microsoft *Word* is the preferred format for submissions. Submissions in versions of T_EX can be accepted in some circumstances: please contact the Editor before submitting. *A paper copy of all electronic submissions must be mailed to the Editor, including originals of all figures.* Please do *not* include figures in the same file as the text of a contribution. Electronic files can be sent to the Editor in three ways: (1) By sending a floppy diskette or CD-R; (2) By attachment to an e-mail message to the Editor (the maximum size for attachments *after* MIME encoding is about 7 MB); (3) By e-mailing the Editor instructions for downloading the material from an ftp site.

Review Process

The review process usually requires about three months. Authors may be asked to modify the manuscript if it is not accepted in its original form. The elapsed time between receipt of a manuscript and publication is usually less than twelve months.

Copyright

Submission of a contribution to the *Radio Science Bulletin* will be interpreted as assignment and release of copyright and any and all other rights to the Radio Science Press, acting as agent and trustee for URSI. Submission for publication implicitly indicates the author(s) agreement with such assignment, and certification that publication will not violate any other copyrights or other rights associated with the submitted material.

APPLICATION FOR AN URSI RADIOSCIENTIST

I have not attended the last URSI General Assembly, and I wish to remain/become an URSI Radioscientist in the 2009-2011 triennium. Subscription to *The Radio Science Bulletin* is included in the fee.

(please type or print in BLOCK LETTERS)

Name : Prof./Dr./Mr./Mrs./Ms. _____
Family Name First Name Middle Initials

Present job title: _____

Years of professional experience: _____

Professional affiliation: _____

I request that all information be sent to my home business address, i.e.:

Company name: _____

Department: _____

Street address: _____

City and postal/zip code: _____

Province/State: _____ Country: _____

Phone: _____ ext. _____ Fax: _____

E-mail: _____

Areas of interest (Please tick)

- | | |
|--|---|
| <input type="checkbox"/> A Electromagnetic Metrology | <input type="checkbox"/> F Wave Propagation & Remote Sensing |
| <input type="checkbox"/> B Fields and Waves | <input type="checkbox"/> G Ionospheric Radio and Propagation |
| <input type="checkbox"/> C Radio-Communication Systems & Signal Processing | <input type="checkbox"/> H Waves in Plasmas |
| <input type="checkbox"/> D Electronics and Photonics | <input type="checkbox"/> J Radio Astronomy |
| <input type="checkbox"/> E Electromagnetic Environment & Interference | <input type="checkbox"/> K Electromagnetics in Biology & Medicine |

I prefer (Please tick)

- | | |
|---|----------|
| <input type="checkbox"/> An electronic version of the RSB downloadable from the URSI web site
(The URSI Board of Officers will consider waiving the fee if a case is made to them in writing.) | 40 Euro |
| <input type="checkbox"/> A hard copy of the RSB sent to the above address | 100 Euro |

Method of payment : VISA / MASTERCARD (we do not accept cheques)

Credit card No Exp. date _____

CVC Code: _____ Date : _____ Signed _____

Please return this signed form to :

The URSI Secretariat
c/o Ghent University / INTEC
Sint-Pietersnieuwstraat 41
B-9000 GHENT, BELGIUM
fax (32) 9-264.42.88